Oxidation photochemistry in the remote marine boundary layer

Dissertation
zur Erlangung des Grades
Doktor der Naturwissenschaftern
Im Promotionsfach Chemie

Am Fachbereich Chemie
Johannes Gutenberg-Universitaet in Mainz

vorgelegt von
Zeinab Hosaynali Beygi
geboren in Teheran, Iran

Mainz, 2010

Abstract

A major consequence of atmospheric pollution is the enhanced concentration of Ozone (O_3) in the troposphere over the last 150 years, in particular since 1950. O_3 is a photochemical oxidant and a greenhouse gas. As the main precursor of the hydroxyl radical (OH) it strongly affects the oxidation power of the atmosphere. Detailed knowledge of the photochemistry of ozone and its main precursors, nitrogen oxides (NOx), in the troposphere is essential for understanding the oxidation capacity of the atmosphere and the related influence on climate. This requires a full understanding of the formation and destruction mechanisms of O_3 and its precursors.

The remote marine boundary layer (MBL) is considered an important region in terms of chemical O_3 loss; however, surface atmospheric observations are sparse and the photochemical processes are not well understood. It is obvious that without an actual dataset of NOx in the ppt_v range it is difficult to estimate photochemical O_3 production/destruction and to quantify the influence of anthropogenic emissions on tropospheric O_3. Therefore, actual measurements of NOx in the clean 'background' region are crucial and of great importance. To investigate the photochemistry of O_3 and its precursors in the clean background conditions of the southern Atlantic Ocean, accurate and precise measurements of NO, NO_2, O_3, JNO_2, $J(O^1D)$, HO_2, OH, ROx and a range of meteorological parameters were carried out. The concentrations of NO and NO_2 measured onboard the French research vessel Marion-Dufresne, crossing the southern Atlantic (28°S-57°S, 46°W-34°E) in March 2007, are among the lowest amounts yet observed. Around 70 % of the Earth's surface is covered by oceans, making processes in the MBL potentially significant for the whole atmosphere. The established data set provides valuable new insight into oxidation processes taking place in the remote MBL.

The data are evaluated for consistency with photochemical steady state (PSS) conditions and the calculations indicate deviations from PSS ($\Phi > 1$). The deviations observed under low NOx conditions (5 to 25 ppt_v) demonstrate a remarkable and unexpected trend in the Leighton ratio (used to characterize PSS), dependent on the NOx mixing ratio and JNO_2 intensity. The most important finding of this investigation is that the Leighton ratio can be valid at very low NOx concentrations in the remote MBL. Significant deviations from unity are seen when an increase is observed in JNO_2 intensity ($\Phi > 1$). Therefore the deviation from unity is not observed at minimum NOx concentrations and JNO_2 values as suggested in previous theoretical studies. This result may be an indication of additional unknown photochemistry taking place at high JNO_2 values in the low NOx regime of the remote MBL.

The investigations within this doctoral thesis clearly demonstrate that under remote marine boundary layer conditions, net photochemical destruction of ozone occurs and that photolysis is the primary cause of ozone destruction during daylight hours. The critical average NO level in the remote MBL is estimated to be between 5 and 9 ppt_v, based on measured parameters. These values are considerably lower than the values suggested by previous studies. These results may imply that the ozone production/destruction potential of the remote Southern Atlantic Ocean is more sensitive to the availability of NO in comparison to other environments.

Further, a direct comparison of the measured species with model output of an atmospheric chemistry general circulation model (EMAC) is performed along the

exact cruise track. To further investigate the consistency of the measurements and our current understanding of atmospheric radical chemistry, a steady-state box model was developed and constrained using data obtained during the cruise. The comparison between measured and model-calculated ROx concentrations in the low NOx regime shows that conventional theory fails to reproduce the observations. The possible causes and implications are discussed in this thesis.

Zusammenfassung

Die bedeutendste Folge der Luftverschmutzung ist eine erhöhte Konzentration an Ozon (O_3) in der Troposphäre innerhalb der letzten 150 Jahre. Ozon ist ein photochemisches Oxidationsmittel und ein Treibhausgas, das als wichtigste Vorstufe des Hydroxyradikals OH die Oxidationskraft der Atmosphäre stark beeinflusst. Um die Oxidationskraft der Atmosphäre und ihren Einfluss auf das Klima verstehen zu können, ist es von großer Bedeutung ein detailliertes Wissen über die Photochemie des Ozons und seiner Vorläufer, den Stickoxiden (NOx), in der Troposphäre zu besitzen. Dies erfordert das Verstehen der Bildungs- und Abbaumechanismen von Ozon und seiner Vorläufer.

Als eine für den chemischen Ozonabbau wichtige Region kann die vom Menschen weitgehend unberührte marine Grenzschicht (Marine boundary layer (MBL)) angesehen werden. Bisher wurden für diese Region jedoch kaum Spurengasmessungen durchgeführt, und so sind die dort ablaufenden photochemischen Prozesse wenig untersucht. Da etwa 70 % der Erdoberfläche mit Ozeanen bedeckt sind, können die in der marinen Granzschicht ablaufenden Prozesse als signifikant für die gesamte Atmosphäre angesehen werden. Dies macht eine genaue Untersuchung dieser Region interessant.

Um die photochemische Produktion und den Abbau von Ozon abschätzen zu können und den Einfluss antrophogener Emissionen auf troposphärisches Ozon zu quantifizieren, sind aktuelle Messergebnisse von NOx im ppt_v-Bereich für diese Region erforderlich. Die notwendigen Messungen von NO, NO_2, O_3, JNO_2, $J(O^1D)$, HO_2, OH, ROx sowie einiger meteorologischer Parameter wurden während der Fahrt des französischen Forschungsschiffes Marion-Dufresne auf dem südlichen Atlantik (28°S-57°S, 46°W-34°E) im März 2007 durchgeführt. Dabei sind für NO und NO_2 die bisher niedrigsten gemessenen Werte zu verzeichnen.

Die während der Messcampagne gewonnen Daten wurden hinsichtlich Ihrer Übereinstimmung mit den Bedingungen des photochemischen stationären Gleichgewichts (photochemical steady state (PSS)) überprüft. Dabei konnte eine Abweichung vom PSS (>1) festgestellt werden, welche unter Bedingungen niedriger NOx-Konzentrationen (5 bis $25ppt_v$) einen unerwarteten Trend im Leighton-Verhältnis bewirkt, der abhängig vom NOx Mischungsverhältnis und der JNO_2 Intensität ist. Signifikante Abweichungen vom Verhältnis liegen bei einer Zunahme der JNO_2 Intensität (>1) vor. Diese Ergebnisse zeigen, dass die Abweichung vom PSS nicht beim Minimum der NOx-Konzentrationen und der JNO_2 Werte liegt, so wie es in bisherigen theoretischen Studien dargelegt wurde und können als Hinweis auf weitere photochemische Prozesse bei höheren JNO_2-Werten in einem System mit niedrigem NOx verstanden werden.
Das wichtigste Ergebnis dieser Untersuchung, ist die Verifizierung des Leighton-Verhältnisses, das zur Charakterisierung des PSS dient, bei sehr geringen NOx-Konzentrationen in der MBL.

Die bei dieser Doktorarbeit gewonnenen Erkenntnisse beweisen, dass unter den Bedingungen der marinen Granzschicht rein photochemischer Abbau von Ozon stattfindet und als Hauptursache hierfür während des Tages die Photolyse gilt. Mit

Hilfe der gemessenen Parameter wurde der kritische NO-Level auf Werte zwischen 5 und 9 ppt_v abgeschätzt, wobei diese Werte im Vergleich zu bisherigen Studien vergleichsweise niedrig sind. Möglicherweise bedeutet dies, dass das Ozon Produktion/ Abbau-Potential des südlichen Atlantiks deutlich stärker auf die Verfügbarkeit von NO reagiert, als es in anderen Regionen der Fall ist.

Im Rahmen der Doktorarbeit wurde desweiteren ein direkter Vergleich der gemessenen Spezies mit dem Modelergebnis eines 3-dimensionalen Zirkulationsmodel zur Simulation atmosphären chemischer Prozesse (EMAC) entlang der exakten Schiffsstrecke durchgeführt.

Um die Übereinstimmung der Messergebnisse mit dem bisherigen Verständnis der atmosphärischen Radikalchemie zu überprüfen, wurde ein Gleichgewichtspunktmodel entwickelt, das die während der Überfahrt erhaltenen Daten für Berechungen verwendet. Ein Vergleich zwischen der gemessenen und der modellierten ROx Konzentrationen in einer Umgebung mit niedrigem NOx zeigt, dass die herkömmliche Theorie zur Reproduktion der Beobachtungen unzureichend ist. Die möglichen Gründe hierfür und die Folgen werden in dieser Doktorarbeit diskutiert.

Contents

Chapter 1: Current state of knowledge on tropospheric O_3 and NOx

The atmosphere acts as a protective layer of gas and is crucial for the existence of life as we know it on planet Earth. It controls the Earth's climate through the radiative properties of its components. Whilst the two most abundant gases are nitrogen (N_2) and oxygen (O_2), which comprise approximately 99% of the total atmospheric volume, they exert almost no effect on the chemical and radiative properties of the atmosphere. Instead the so-called trace gases, species which are present at mixing ratios from parts per million (ppm_v) to parts per trillion (ppt_v), drive the chemical and physical processes in the atmosphere. These species include greenhouse gases (GHG): namely water vapour, carbon dioxide (CO_2), methane (CH_4), ozone (O_3) and nitrous oxide (N_2O) (IPCC, 2007). The role trace gases play is disproportionate to their abundance in the atmosphere. Photochemical smog, stratospheric O_3 depletion and climate change are a few of the phenomena brought about by the anthropogenic increase in the concentrations of some trace gas species. There is clear evidence that trace gas species are responsible for altering the basic chemistry of the atmosphere.

Living in the "Anthropocene" has made understanding the impacts of human activity on the environment a critical area of scientific research. The atmosphere is one of the many recipients of anthropogenic pollution resulting from modern human activity and industrialization. Every day, a variety of chemicals is released into the air in large quantities, resulting in changes to the chemistry of the atmosphere on a local, regional and global scale and therefore leads to significant climate perturbations. An accurate and indepth understanding of the atmosphere is a prequistie for sound predictions of future climate change, which are crucial in order to achieve efficient mitigation policies.

1.1 The importance of tropospheric O_3 and NOx

A major consequence of atmospheric pollution is the enhanced concentration of O_3 in the troposphere over the last 150 years. O_3 is a "paradoxical" trace gas with different roles depending on where it is located. It is essential in the stratosphere where it protects human life from damaging ultra-violet radiation (UV-B) from the sun. About 90% of the O_3 in the atmosphere is located in the stratosphere and is commonly referred to as the "ozone layer". On the other hand, O_3 is considered a photochemical pollutant and a greenhouse gas in the troposphere, with a significant impact on both air quality and global warming (Fishman et al., 1979). O_3 in the troposphere is also a toxic gas which can have potentially negative effects on human health, ecosystems and the environment in general (WHO, 2003). Therefore, in order to better understand the radiative budget of the atmosphere and the related influence on the climate, we need further knowledge of the spatial and temporal distribution of O_3 in the atmosphere. This requires a full understanding of the formation and destruction mechanisms of O_3 and its precursors.

O_3 plays a key role in the chemistry of the troposphere. It is an important precursor to the hydroxyl radical (OH), which is the primary cleansing agent of the lower atmosphere (IPCC, 2007). OH reacts with almost all the anthropogenic and natural trace gases in the atmosphere and therefore affects their concentration and lifetime.

Together, O_3 and OH determine the oxidizing capacity of the troposphere (Thompson, 1992). During the past few decades, an increase in tropospheric O_3 concentrations has been reported (Liu et al., 1987, Logan, 1985, Tiao et al., 1986). The rate of increase in O_3 is believed to be about 1% per year (Crutzen, 1988, Janach, 1989). Studies using 3-dimensional global models have estimated that O_3 concentrations may have more than doubled over large parts of the Northern Hemisphere since pre-industrial times (Lelieveld and Dentener, 2000). This increase has been attributed to anthropogenic emission of NOx (NOx = NO + NO_2), CO and volatile organic carbons (VOCs) and subsequent photochemistry (Davis et al., 1996, Kondo et al., 1996). Nitrogen oxides are the most important species as O_3 precursors in the troposphere (Crutzen, 1979). Photochemical O_3 production or loss is determined by the abundance of NOx (Liu et al., 1987). In NOx- rich environments, NO_2 photolysis leads to a net production of O_3, while the photolysis of O_3 will result in net O_3 destruction in low NOx regimes. The topic of photochemical production/destruction of O_3 in the remote troposphere has been investigated in the past (Chameides and Walker, 1973, Crutzen, 1973). Fishman et al. have calculated the O_3 production and destruction rates in the Northern Hemisphere as a function of the estimated NOx concentration (Fishman et al., 1979). As a result of this calculation, the 'critical' NOx concentration was estimated at 20-30 ppt_v where the O_3 production rate balances with the destruction rate. It is obvious that without an actual dataset of NOx in the ppt_v range it is difficult to estimate photochemical O_3 production and quantify the influence of anthropogenic emissions on tropospheric O_3. Therefore measurements of NOx in the clean 'background' region are crucial.

Only recently have instrumental techniques become available with sufficient sensitivity and range of detectability to measure NOx in non-urban regions (ppt_v range). This limits the size of the database needed to define non-urban NOx concentrations. It is important to measure NO and NO_2 simultaneously in the clean marine atmosphere in order to discuss the O_3 photochemistry accurately.

1.2 The major sources and sinks of NOx

Nitrogen oxides have short atmospheric lifetimes of hours to days. Therefore, there is a high degree of variability in tropospheric NOx concentrations. The lifetime of NOx is relatively short close to the Earth's surface (hours), however, it increases at higher altitudes (days). The lifetime also depends on the season i.e. it is longer in winter than in summer due to the lower OH concentrations in the winter.

The sources of NOx in the troposphere are both natural (soil, lightning and wildfires) and anthropogenic (fossil fuel, biomass burning). The largest source of NOx is fossil fuel combustion, which together with the emissions from biomass burning and anthropogenic activities dominates the NOx budget. NOx is emitted predominantly as NO, the fraction of NO_2 emitted can vary between 1% and 30%. As a result of the short lifetime of NOx, there is very little influence of vertical or horizontal transport. Therefore, since the majority of fossil fuel combustion is in urban or the vicinity of urban areas, regions close to the urban centres are impacted the most. This strong weighting of the NOx distribution towards the major source regions is more pronounced in the north-eastern USA, Europe and eastern Asia. This can clearly be seen in figure 1.1, which shows a 5-year mean surface mixing ratio of

NOx computed by the ECHAM/MESSy Atmospheric Chemistry model (EMAC) (Joeckel et al., 2006).

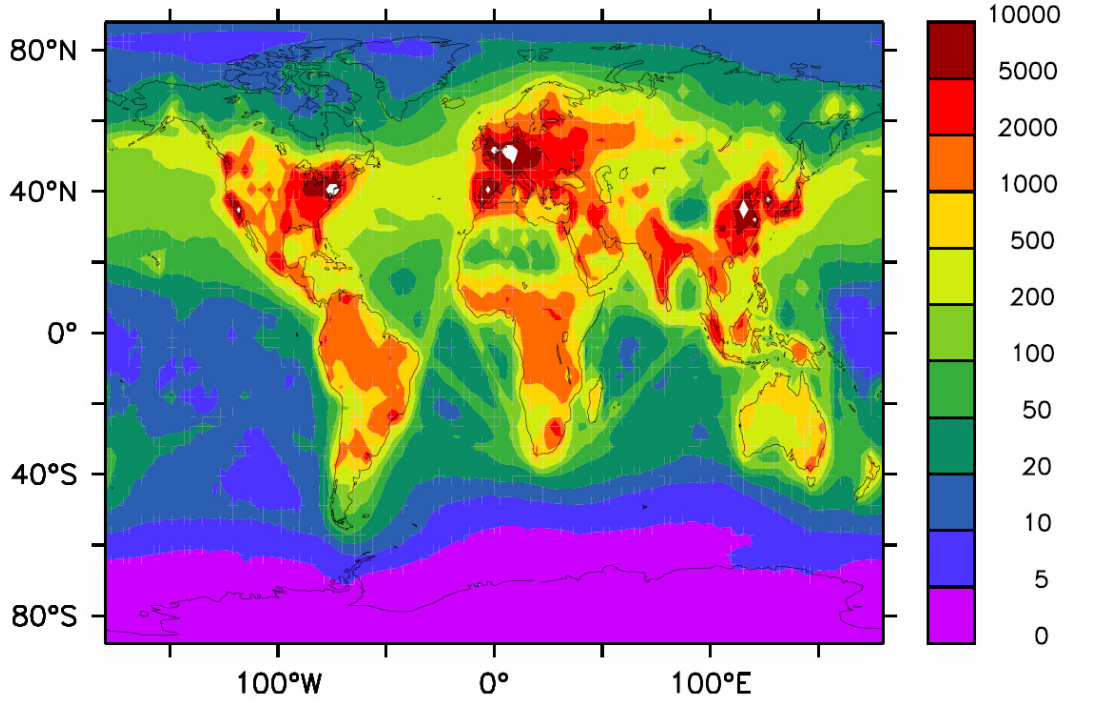

Figure 1.1 Five year mean surface mixing ratios of NOx, unit is in ppt_v.

Secondary maxima are seen in regions of strong biomass burning and bio-fuel use, which is mostly in South America, central Africa and southern Asia. Also, the influence of ocean-going ship emissions is clearly seen in the distributions over the Atlantic and Indian oceans between major ports.

The main sources of NOx in the troposphere are listed in table 1.1 (IPCC, 2007). Lightning, emissions from aircraft and transport from the stratosphere are minor contributors to total NOx sources. However these 'minor' contributions can greatly impact O_3 production in the remote troposphere where NOx concentrations are low and often close to the critical NO mixing ratio.

Table 1.1 Estimate of global tropospheric NOx emissions in TgN yr^{-1}

Sources	Emissions,TgN yr^{-1}
Fossil fuel combustion	33.0
Aircraft	0.7
Biomass burning	7.1
Soils	5.6
Lightning	5.0
Stratosphere	<0.5
Total	51.9

Two known species which can act as reservoir compounds for NOx are nitric acid (HNO_3) (Huebert and Lazrus, 1978) and organic nitrates like peroxyacetyl nitrate

(PAN) (Demerjian et al., 1974). PAN has a longer lifetime compared to NOx and can be transported and subsequently undergo thermal decomposition to release NOx. Both PAN and HNO_3 can undergo photolysis to release NO_2. The main sink of NOx in the troposphere is the formation of HNO_3 (and thereby acid rain) from NO_2 and OH. Gaseous HNO_3 has a high deposition velocity and is readily adsorbed onto surfaces such as aerosols and water (Finalyson-Pitts and Pitts, 1999). The oxidation products of NOx are removed by wet and dry deposition from the atmosphere.

A summary of the NOx measurements made in four regions of the globe is presented in table 1.2 (Seinfeld and Pandis, 2006). As can be seen in the table, NOx concentrations decrease sharply as one moves from urban to rural and then remote sites. This is due to the fact that the short lifetime of NOx in the lower troposphere limits its direct transport to remote regions of the globe.

Table 1.2 Typical boundary-layer NOx mixing ratios

Region	NOx, ppb_v
Urban-suburban	10-1000
Rural	0.2-10
Remote tropical forest	0.02-0.08
Remote marine	0.02-0.04

Previous ground-based measurements of NOx at rural and mountain-top sites show that NOx concentrations are in the range of several hundred ppt_v e.g. (Bollinger et al., 1984). As for the remote marine atmosphere, NO concentrations are observed below 10 ppt_v (Liu et al., 1983, McFarland et al., 1979). From these values NO_2 concentration in the marine boundary layer (MBL) were expected to be below 100ppt_v. Several model calculations have suggested that NOx concentrations are below 100 ppt_v in the MBL.

1.3 Ozone distribution

The tropospheric sources and sinks of O_3 is a topic of interest which has been studied extensively since the early 1970s (Fabian, 1974, Fabian and Pruchniewicz, 1977, Liu et al., 1980, Logan, 1981). There has been a long standing debate over the relative importance of O_3 transport from the stratosphere versus in situ photochemical O_3 production. In the past, O_3 in the troposphere was thought to be solely a result of transport from the O_3 rich lower stratosphere (Singh et al., 1978). Observations of the negative effects of photochemical smog on people and the environment in polluted urban areas, due to enhanced O_3 levels in the 1950s (Haagensmit, 1952), led to the theory that O_3 was being photochemically produced in the urban troposphere (Haagensmit and Fox, 1956, Leighton, 1961). Several atmospheric chemistry global modelling studies (Lelieveld and Dentener, 2000, Wang and Jacob, 1998) have concluded that even though stratospheric intrusion contributes to the tropospheric O_3 budget in the free troposphere, the photochemical production of O_3 dominates in the lower troposphere and the planetary boundary layer. O_3 is formed predominantly in continental regions where there are sources of NOx and is believed to be mainly lost

in the marine boundary layer where sources are small (Lelieveld et al., 2004). In summary, water vapour, short-wave radiation and NOx concentrations determine whether an environment or air mass is O_3 producing or destroying. The local budget of O_3 can be described by the following equation:

$d[O_3]/dt = \pm$ horizontal advection $\pm$ vertical advection $\pm$ photochemistry – deposition

Horizontal advection: Significant concentrations of O_3 are produced over urban and industrialized regions during warm seasons. Advection from these sources is dependent on the photochemical lifetime of O_3 which is approximately 10 days (Liu et al., 1980).

Vertical advection: Stratospheric intrusion of O_3 is often connected to tropopause folding events at extra-tropical latitudes (Danielsen, 1968) and is believed to show a seasonal maximum in spring (Danielsen and Mohnen, 1977).

Photochemistry: Photochemical production of O_3 in the troposphere is thought to be much larger than transport from the stratosphere (Crutzen, 1973, Logan, 1985). The production of O_3 in the troposphere is a result of the presence of NOx, hydrocarbons, and sunlight (Crutzen, 1988, Liu et al., 1980, Liu et al., 1987). Loss of tropospheric O_3 takes place through chemical reactions and dry deposition.

1.4 The NOx - O_3 photostationary state relation

To begin consider a simple photochemical system i.e. a hypothetical air mass containing only NO, NO_2 and O_3. The process begins with the photolysis of NO_2 in sunlight, at wavelengths less than 424 nm, resulting in the formation of O_3:

$$NO_2 + h\nu \rightarrow NO + O(^3P) \qquad (\lambda<424 \text{ nm}) \qquad \text{(R1.1)}$$

$$O(^3P) + O_2 + M \rightarrow O_3 + M \qquad \text{(R1.2)}$$

Here M represents a third molecule that stabilizes the formation of O_3 by absorbing excess energy. The above mechanism is believed to be the only source of O_3 production in the troposphere (Seinfeld and Pandis, 2006). O_3 produced in reaction R1.2 can react with NO to regenerate NO_2:

$$O_3 + NO \rightarrow NO_2 + O_2 \qquad \text{(R1.3)}$$

With enough actinic flux the above reactions (R1.1 to R1.3) will reach a point where NO_2 is destroyed and produced rapidly and as a result a steady state cycle is maintained. Although O_3 is produced from the photolysis of nitrogen dioxide (R1.1), the subsequent titration of O_3 by nitric oxide (R1.3) limits O_3 formation and therefore results in a balance between O_3 production and titration. Therefore, if cycling between NO and NO_2 only occurs through the photolysis of NO_2 and the reaction of NO with O_3, a null cycle is established during the day and therefore there is no net O_3 production.

Peroxy radicals (ROx = HO_2 + RO_2) provide an alternate pathway to R1.3, where R denotes the chemical formula for any member of the alkyl group. This subsequently leads to the conversion of NO to NO_2 without O_3 destruction in R1.4 and R1.5, leading to the accumulation of O_3:

$$HO_2+NO \rightarrow NO_2+OH \quad \text{(R1.4)}$$

$$RO_2+NO \rightarrow NO_2+ RO \quad \text{(R1.5)}$$

$$CH_3O_2 + NO \rightarrow CH_3O + NO_2 \quad \text{(R1.6)}$$

The production rate of O_3 is determined by the photolysis of NO_2. Thus, the equilibrium between NO and NO_2 is the important factor for O_3 production. In conditions where the actinic flux is strong enough for the rapid exchange between NO and NO_2 to take place, PSS can be established in a matter of minutes.

The expression that results from the steady state analysis of reactions R1.1 to R1.3 has been named the photostationary state relation or the Leighton ratio (φ) (Leighton, 1961):

$$\varphi = \frac{JNO_2[NO_2]}{k_3[O_3][NO]} \quad \text{(Equation 1.1)}$$

where JNO_2 is the NO_2 photolysis rate (s^{-1}) and k_3 is the reaction rate constant of R1.3 (cm^3/molecules.s).

The Leighton ratio is used as a means of characterizing photostationary state. The ratio can be used as an indicator to test our current understanding of tropospheric chemistry mechanisms (Hauglustaine et al., 1996, Ridley et al., 1992). Numerous studies have investigated adherence to or deviation from PSS (Leighton ratio). It has been shown that due to the high NOx levels in urban areas the Leighton ratio is approximately equal to unity e.g. (Carpenter et al., 1998, Thornton et al., 2002, Yang et al., 2004). This is due to the removal of ROx radicals by NO_2 and as a result reactions R1.4 and R1.5 are insignificant (Calvert, 1976). In other words, the PSS relation is expected to hold when reactions R1.1 and R1.3 are the main loss processes for NO_2 and O_3. The "classic Leighton ratio" (equation 1.1) is widely used in studies as a means of deducing the concentration of O_3, NO or NO_2 under photostationary (PSS) conditions. If two of the three concentrations are known the concentration of the third specie can be calculated using equation 1.1. While the equation may hold true in urban and polluted conditions where high NOx concentrations suppress any radical chemistry, this is not necessarily the case in rural or remote 'background' regions. In areas with lower NOx levels, the ratio is expected to deviate from unity (Hauglustaine et al., 1996, Hauglustaine et al., 1999, Mannschreck et al., 2004, Parrish et al., 1986, Volz-Thomas et al., 2003). This is due to the fact that in remote regions, low NO concentrations reduce the importance of reactions R1.4 and R1.5 as peroxy radical sinks. This results in the increase of peroxy radical levels, and consequently reactions R1.4 and R1.5 (reaction of NO with HO_2 and RO_2) compete with reaction R1.3 (reaction of NO with O_3). In this case, steady state NOx partitioning depends on peroxy radical concentrations:

$$\varphi = \frac{JNO_2[NO_2]}{(k_3[O_3]+k_4[HO_2]+\sum k_i[R_iO_2])[NO]} \qquad \text{(Equation 1.2)}$$

where k_3, k_4, and k_i are the reaction rates of R1.3, R1.4 and R1.5 respectively. In the above equation, R_iO_2 includes all organic peroxy radicals. Assuming that RiO_2 is negligible relative to CH_3O_2 in remote regions, the above equation is expressed as:

$$\varphi = \frac{JNO_2[NO_2]}{(k_3[O_3]+k_4[HO_2]+k_6[CH_3O_2])[NO]} \qquad \text{(Equation 1.3)}$$

In many previous studies, the above equations were used to theoretically estimate the concentrations of the peroxy radicals (Hauglustaine et al., 1996, Hauglustaine et al., 1999, Parrish et al., 1986, Thornton et al., 2002). However, studies show that there is disagreement between ROx concentrations estimated by this method and observed and model calculated ROx concentrations. Such a disagreement was also found in this study, as discussed in detail in Chapter four. Deviations from PSS can occur for the following reasons:

1. The main cause for such a disagreement is suspected to be an unknown oxidation pathway which can result in the additional oxidation of NO to NO_2. Since it is unaccounted for in the Leighton ratio, the existance of such a pathway would lead to a significant overestimation of the theoretically calculated ROx compared to measured or model calculated ROx. A class of reactants which is believed to be of importance are the halogen monoxides (XO) (Carpenter et al., 1998, Chameides et al., 1990, Chatfield and Crutzen, 1990, Kanaya, 2002). XO (ClO, BrO or IO) can convert NO to NO_2 via the reaction:

$$XO + NO \rightarrow NO_2 + X. \qquad \text{(R1.7)}$$

Halogen oxides have been observed in remote marine regions (Yang et al., 2004) and a possible XO contribution to the PSS of NOx and O_3 will be discussed in more detail later in the chapter.

2. Deviations also occur when loss processes for O_3 other than reaction R1.3 become significant; this results in O_3 no longer being in a steady state. The additional loss processes can be O_3 photolysis, reactions of O_3 with NO_2, alkenes and radicals.

3. At sunrise and sunset, deviations from unity are expected due to small JNO_2 values, therefore steady state assumptions are not valid.

4. If reaction time is not sufficient to quickly achieve a new steady state after perturbations in concentration of gases in an air mass e.g. due to source pollution, then PSS assumption is not valid.

5. Role of reservoir species such as PAN as additional NO_2 sources can result in deviations from PSS.

6. Reaction rates in the Leighton equation are also deemed extremely important for PSS calculations. The calculated ratios are significantly influenced by the uncertainties in the reaction rates of k_1, k_2 and k_3.

7. Uncertainties in the measured values of JNO_2, O_3, NO, NO_2 and ROx are also another important factor. It is extremely important to carry out accurate and precise

simultaneous measurements of the mentioned species in order to better understand the causes for deviations.

1.5 The remote marine boundary layer

The MBL is the lowest part of the troposphere that is in direct contact with the sea surface. About 70 % of the Earth's surface is covered by oceans, making processes in the MBL potentially significant for the whole atmosphere. The remote MBL is well suited to study the unperturbed chemical processes that drive NOx and O_3 photochemistry (Crawford et al., 1997, Monks et al., 1998).

Therefore, the pristine background atmosphere can be considered a "buffer" against the anthropogenic production and enhancement of O_3 occurring in polluted regions of the globe. The destruction of O_3 in the MBL is thought to be driven by significant O_3 photolysis rates in the presence of high concentrations of water vapour. However, the capacity to buffer O_3 is destroyed once long range transport and release of NOx from reservoir species kick in. The erosion of the O_3 buffering potential of the remote troposphere can be for example a result of direct anthropogenic emissions from shipping and aircraft.

Even though the MBL is an important region in terms of O_3 loss, surface atmospheric observations in this region are extremely sparse. In this study, in order to investigate the PSS of NOx and O_3 in the remote MBL, accurate and precise measurements of NO, NO_2, O_3, JNO_2, $JO(^1D)$, HO_2, OH, ROx and a range of meteorological parameters were carried out simultaneously. The measurement of all above parameters is required and necessary in order to study the NOx and O_3 PSS relationship accurately.

1.6 The photochemical O_3 production cycle

The chemistry of the remote background troposphere is dominated by the two gases methane (CH_4) and carbon monoxide (CO). In continental regions, where anthropogenic and biogenic emissions greatly impact the VOC composition of the atmosphere, the chemistry is more complicated than that of CH_4 and CO alone. However, the basic elements of the chemistry are similar.

The reactions in the photochemical O_3 formation cycle of CO in the troposphere are as follows (Crutzen, 1974):

$$CO + OH \rightarrow CO_2 + H \qquad \text{(R1.8)}$$

$$H + O_2 + M \rightarrow HO_2 + M \qquad \text{(R1.9)}$$

$$HO_2 + NO \rightarrow OH + NO_2 \qquad \text{(R1.4)}$$

$$NO_2 + h\nu \rightarrow NO + O \qquad (\lambda<424\ \text{nm}) \qquad \text{(R1.1)}$$

$$O + O_2 + M \rightarrow O_3 + M \quad \text{(R1.2)}$$

$$\mathbf{net: CO + 2O_2 + h\nu \rightarrow CO_2 + O_3} \quad \text{(R1.10)}$$

where M is a third body, e.g. N_2 or O_2. Due to low NO concentrations, the self-reaction of HO_2 and RO_2 can become competitive with NO reactions. Reactions which are known to compete with R1.4 are as follows:

$$HO_2 + HO_2 \rightarrow H_2O_2 + O_2 \quad \text{(R1.11)}$$

$$HO_2 + RO_2 \rightarrow ROOH + O_2 \quad \text{(R1.12)}$$

$$RO_2 + RO_2 \rightarrow \text{products} \quad \text{(R1.13)}$$

$$HO_2 + OH \rightarrow H_2O + O_2 \quad \text{(R1.14)}$$

Reactions R.11, R.12, R.13 and R.14 do not oxidize NO to NO_2; therefore O_3 can not be formed via NO_2 photolysis. In addition, the reaction of HO_2 and O_3 results in O_3 destruction:

$$HO_2 + O_3 \rightarrow OH + 2O_2 \quad \text{(R1.15)}$$

Also if O_3 is dissociated by actinic radiation it can produce an excited oxygen atom ($O(^1D)$) which can in turn react with water to form two OH radicals (reactions R1.16 and R1.17). This is a major source of OH in both clean and polluted air:

$$O_3 + h\nu \rightarrow O_2 + O(^1D) \qquad (\lambda<320 \text{ nm}) \quad \text{(R1.16)}$$

$$O(^1D) + H_2O \rightarrow 2OH \quad \text{(R1.17)}$$

The net O_3 destruction is the total sum of reactions: R1.8, R1.9, R1.15, R1.16 and R1.17.

$$\mathbf{net: CO + H_2O + 2O_3 + h\nu \rightarrow CO_2 + 2O_2 + 2OH} \quad \text{(R1.18)}$$

When reaction R1.4 occurs and HO_2 reacts mainly with NO, the production cycle of O_3 exceeds the destruction cycle. This is due to the fact that reaction R1.4 is about 1000 times faster than reaction R1.11 (DeMore et al., 1997). NO mixing ratios above approximately 15 ppt_v can result in net O_3 production. Therefore the NO concentration is the most important factor in determining the net O_3 production or destruction.

As mentioned above, in addition to CO, CH_4 also contributes to O_3 production:

$$CH_4 + OH \rightarrow CH_3 + H_2O \quad \text{(R1.19)}$$

$CH_3 + O_2 + M \rightarrow CH_3O_2 + M$ (R1.20)

$CH_3O_2 + NO \rightarrow CH_3O + NO_2$ (R1.6)

$CH_3O + O_2 \rightarrow CH_2O + HO_2$ (R1.21)

$HO_2 + NO \rightarrow OH + NO_2$ (R1.4)

$NO_2 + h\nu \rightarrow NO + O$ (λ<424 nm) (x 2) (R1.1)

$O + O_2 + M \rightarrow O_3 + M$ (x 2) (R1.2)

net: $CH_4 + 4O_2 + h\nu \rightarrow CH_2O + H_2O + 2O_3$ (R1.22)

where "(x 2)" represents the necessity of the reaction occurring twice to obtain the net reaction. In these cycles, NO is converted to NO_2 through the reactions; R1.3, R1.4, R1.5 and R1.6. NO_2 is rapidly converted back into NO through photolysis. Taking into account the reaction rates and the concentrations of reactants, the conversion reactions between NO and NO_2, a photostationary state equilibrium can be reached within a few minutes in the daytime. Due to the rapidity of photochemical conversion between NO and NO_2, the sum of their mixing ratios is generally treated as a single variable, i.e. NOx. Photochemical O_3 production can only occur in the presence of NOx, CO, or hydrocarbons. When elevated levels of NOx are present, the oxidation of CO and hydrocarbons leads predominately to the formation of tropospheric O_3 (Ridley et al., 1992). However, in the remote marine boundary layer, under conditions of high actinic flux and high humidity, ozone is destroyed (Crutzen, 1974, Monks et al., 1998). If the NO/O_3 ratio drops below ca. 1/4000, the self-reaction of hydroperoxy radicals is favoured over the reaction with NO, and O_3 is slowly destroyed, rather than produced (Liu et al., 1987).

Since the reaction of peroxy radicals with NO leads to net O_3 production (R1.4 and R1.5), the rate of O_3 production $P(O_3)$ can be expressed as follows:

$$P(O_3)=\{k_4[HO_2]+k_5[RO_2]\}[NO] \quad \text{(Equation 1.4)}$$

where k_4 and k_5 are the rate constants of reactions R1.4 and R1.5 respectively (Crawford et al., 1997). On the other hand, reactions R1.15, R1.16, R1.17 and R1.23 lead to net O_3 loss, $L(O_3)$.

$OH + O_3 \rightarrow HO_2 + O_2$ (R1.23)

$L(O_3)$ can be expressed as:

$$L(O_3) = k_{15}[HO_2][O_3]+k_{17}[O(^1D)][H_2O]+k_{23}[OH][O_3] \quad \text{(Equation 1.5)}$$

where k_{15}, k_{17} and k_{23} are the rate constants of reactions R1.15, R1.17 and R1.23 respectively. The net O_3 photochemical tendency, $T(O_3)$, can be expressed as the difference between the production and loss rates (Crawford et al., 1997):

$$T(O_3) = P(O_3) - L(O_3) \quad \text{(Equation 1.6)}$$

1.7 The fate of NOx and photochemical cycle termination

As mentioned previously, after NO is emitted it is rapidly converted to NO_2. NO_2 can react with H_2O heterogeneously and form nitrous acid (HONO):

$$2NO_2 + H_2O \rightarrow HONO + HNO_3 \quad \text{(R1.24)}$$

However, it is worth mentioning that during the day HONO is formed as a result of the following reaction:

$$OH + NO + M \rightarrow HONO + M \quad \text{(R1.25)}$$

Because HONO photolysis is rapid during daytime, significant concentrations of HONO are not generated:

$$HONO + h\nu \rightarrow NO + OH \quad \text{(R1.26)}$$

NO_2 reacts with RO_2 to form peroxy organic nitrates:

$$NO_2 + RO_2 + M \rightarrow RO_2NO_2 + M \quad \text{(R1.27)}$$

RO_2NO_2 plays a role as a reservoir of NOx. NO_2 is produced through thermal decomposition of RO_2NO_2:

$$RO_2NO_2 + M \rightarrow NO_2 + RO_2 + M \quad \text{(R1.28)}$$

The nitrate radical, NO_3, is formed via the reaction of NO_2 with O_3.

$$NO_2 + O_3 \rightarrow NO_3 + O_2 \quad \text{(R1.29)}$$

Subsequently, NO_3 reacts with NO_2, forming N_2O_5 in a reversible reaction:

$$NO_2 + NO_3 + M \leftrightarrow N_2O_5 + M \quad \text{(R1.30)}$$

N_2O_5 can be also converted to HNO_3 through hydrolysis on surfaces and droplets:

$$N_2O_5\,(g) + H_2O\,(l) \rightarrow 2HNO_3\,(aq) \quad \text{(R1.31)}$$

Reaction R1.31 is believed to be a strong source of atmospheric HNO_3 (Ljungstrom and Hallquist, 1996). Through this reaction, NOx contributes to the acidification of aerosol particles and cloud droplets, which subsequently impact ecosystems in the form of acid rain. Over the past decade, the emissions of SO_2 have been dramatically reduced in most industrialized countries and therefore the relative importance of HNO_3 has increased.

NO_3 is rapidly photolysed during daytime but at night takes over the role of OH as the most reactive radical in the troposphere:

$$NO_3 + h\nu \rightarrow NO_2 + O \qquad \text{(R1.32a)}$$

$$NO_3 + h\nu \rightarrow NO + O_2 \qquad \text{(R1.32b)}$$

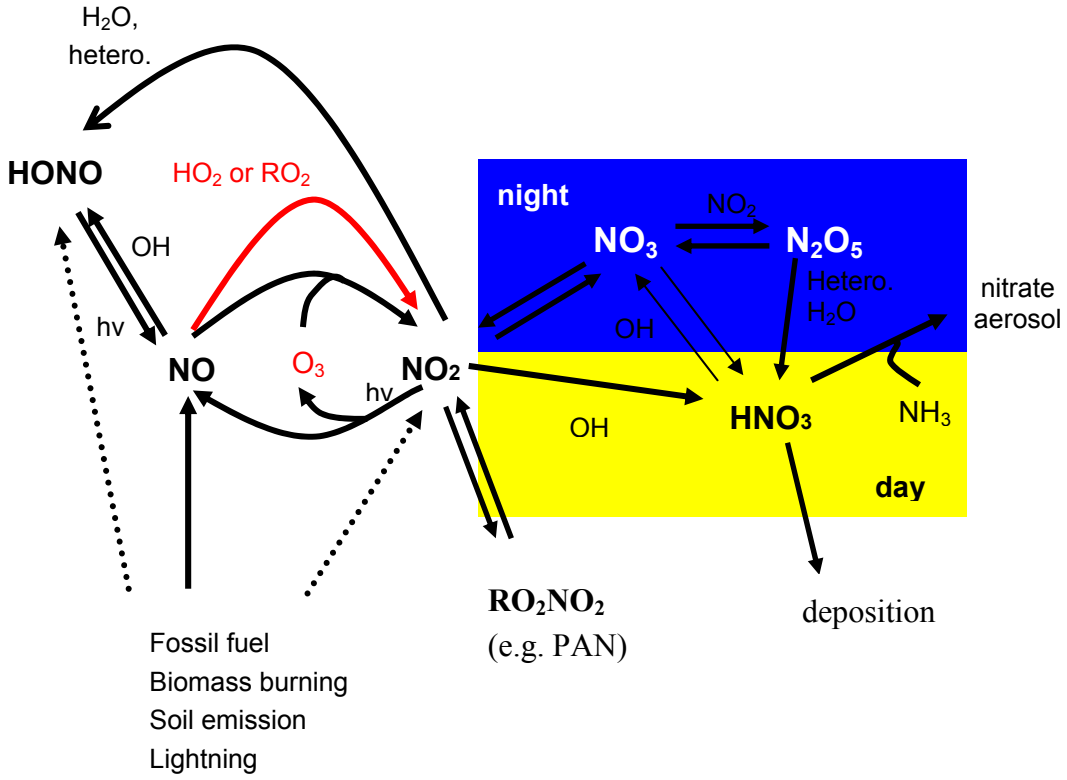

Figure 1.2 Cycle of tropospheric NOx chemistry (adapted from (Richter, 2009)).

Termination of the photochemical chain occurs when NO_2 reacts with OH to form HNO_3:

$$OH + NO_2 + M \rightarrow HNO_3 + M \qquad \text{(R1.33)}$$

This reaction removes both HOx and NOx from the atmosphere. HNO_3 is formed through several other pathways in the absence of sunlight:

$$N_2O_5\,(g) + H_2O\,(g,l) \rightarrow 2HNO_3\,(g, aq) \qquad \text{(R1.34)}$$

NO_3 (aq) + H_2O (l) → HNO_3 (aq) + OH (aq) (R1.35)

NO_3 + RH → HNO_3 (g) + R (R1.36)

Subsequently, HNO_3 is removed from the atmosphere through dry and wet deposition onto the earth's surface and is rapidly taken up by droplets and aerosols. The key loss process for reactive nitrogen is through conversion to and loss of HNO_3, with about half of the total loss of HNO_3 being due to wet deposition and one third due to dry deposition. The loss of aerosol nitrate by particle sedimentation contributes a further 15 to 20 %. The direct loss of NOx due to dry deposition of NO_2 contributes less than 10 % to the total budget (Joeckel et al., 2006). The chemistry of tropospheric NOx is illustrated in a simplified sketch in figure 1.2.

1.8 Halogen Chemistry in the MBL

A widespread effect of halogens on tropospheric oxidants in the MBL has been suggested by a number of theoretical and observational studies (Dickerson et al., 1999, Galbally et al., 2000, Vogt et al., 1996, von Glasow et al., 2004, Yang et al., 2005). However, there is a great deal of uncertainty due to the lack of observations representative of the pristine MBL (Leser et al., 2003, Read et al., 2008). Halogens are known to be involved in many reaction cycles that can affect the oxidation power of the atmosphere. This is done both directly via reaction of Cl with hydrocarbons and indirectly by affecting the main oxidants of the atmosphere HOx, O_3 and NOx. Most current assessments of O_3 chemistry in the troposphere do not take into account the effects of halogen chemistry and as a result possibly overestimate O_3 concentrations, or the contributions of O_3 sources. In a modelling study it was shown that halogen reactions could change the global O_3 budget by 5 to 20% (von Glasow et al., 2004). It is known that the sum of particulate and gaseous halogen concentrations maximize in the marine troposphere. Chloride is the most abundant halogen in the ocean and exists in the form of sodium chloride. Bromide is also present in the ocean, but is much less abundant than chloride. Iodine compounds are even rarer than the other two halogens. The chemistry of the fourth halogen, fluoride, is not discussed here as it is found in the form of the very un-reactive species HF in the atmosphere.

1.8.1 Halogen release and its effect on O_3 in the MBL

Reactive halogen compounds are released into the MBL by the photodecomposition of organic halogen compounds emitted from the oceans such as bromoform ($CHBr_3$) and also via inorganic halogen compounds released from sea-salt aerosol through the action of acidic compounds (Galbally et al., 2000).

Droplets of sea spray are continuously emitted from the ocean. The sea spray contains bromide and chloride salts, which can be converted in a series of steps into bromine and chlorine containing compounds (e.g. Br_2 and BrCl) which are essentially water insoluble. Br_2 and BrCl are then in turn released from the droplet into the

atmosphere and subsequently broken down by sunlight resulting in bromine and chlorine atoms. These atoms can react with O_3 to produce halogen oxide (XO):

$$X + O_3 \rightarrow XO + O_2 \qquad (X=Cl, Br, I) \qquad (R1.37)$$

XO can be rapidly photolyzed, resulting in the reproduction of O_3. The speed of photolysis for the different halogen monoxides is: IO>BrO>ClO (Dr. R. Sander, personal communication 2009). In order for net O_3 destruction to take place, XO must react with HO_2, NO_2, or another XO. It is thought that the main halogen related O_3 destruction in the remote MBL occurs via the reaction of XO with HO_2:

$$XO + HO_2 \rightarrow HOX + O_2 \qquad (R1.38)$$

$$HOX + h\nu \rightarrow X + OH \qquad (R1.39)$$

$$\text{Net: } \mathbf{O_3 + HO_2 \rightarrow OH + 2O_2} \qquad (R1.40)$$

The reaction of XO with HO_2, through reaction R1.38, can result in a decrease in the $[HO_2]/[OH]$ ratio and subsequently reduce O_3 production. Halogen oxides also cause a decrease in the NO/NO_2 ratio, through reaction with NO:

$$XO + NO \rightarrow X + NO_2 \qquad (R1.7)$$

The formation of NO_2 through reaction R1.7 does not lead to an increase in O_3 concentrations because a halogen atom is formed, which will subsequently destroy O_3 via reaction R1.37. Figure 1.3 illustrates the effect of halogen monoxides on the O_3 cycle in the troposphere in a simplified sketch (von Glasow and Crutzen, 2007).

Even though the mixing ratio of XO is small (ppt_v) in the remote MBL, the cycle does contribute to O_3 destruction. In a study carried out by Duce et al. it was concluded that bromine and chlorine are lost from sea salt particles, while iodine is enriched relative to the composition of the sea water (Duce et al., 1965).

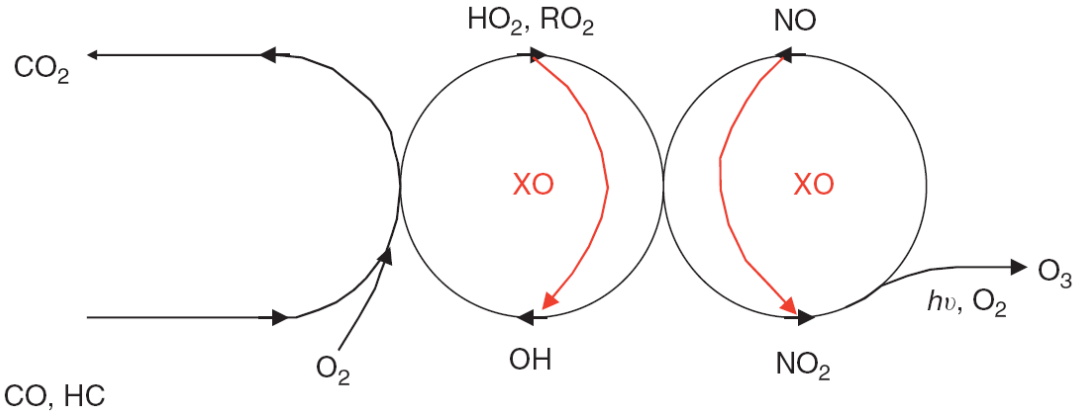

Figure 1.3 Chemical interactions of halogen monoxides with O_3 and NOx in the troposphere.

Iodine oxide is thought to have a different source from bromine and chloride because the concentrations of iodine compounds in the ocean are too small to account for observed IO concentrations. This source is believed to be marine algae and phytoplankton. These species produce organic iodine containing molecules that are photolyzed by sunlight to produce iodine atoms. These then decrease O_3 using the same sequence of reactions as for bromine atoms (von Glasow, 2008).

1.8.2 The remote MBL and halogen release

Several formation mechanisms of reactive halogens have been suggested, but the majority are only possible in the presence of significant mixing ratios of NOx, which is not the case in the remote MBL. However, bromine and chlorine release into gaseous phase from sea salt aerosols is a widely observed phenomenon not only in the polluted MBL, but also in the remote MBL. Therefore it is believed that there are means, other than acid displacement, to release reactive halogens from the sea salt aerosol.

Vogt et al. have suggested a possible mechanism for bromine and chlorine release from sea-salt aerosol in pristine MBL conditions (Vogt et al., 1996). In an autocatalytic mechanism, they propose that hypobromous acid (HOBr) is scavenged by the sea salt aerosol. The bromide to chloride ratio in sea water is approximately 1/700. Therefore HOBr reacts with chloride:

$$HOBr + Cl^- + H^+ \leftrightarrow BrCl + H_2O \quad \text{(R1.41)}$$

HOBr also reacts with bromide:

$$HOBr + Br^- + H^+ \leftrightarrow Br_2 + H_2O \quad \text{(R1.42)}$$

Due to the high chloride to bromide ratio, R1.41 is much more important than R1.42. A substantial fraction of BrCl, produced from R1.41, will react with bromide, leading to autocatalytic Br activation:

$$BrCl + Br^- \leftrightarrow Br_2Cl^- \quad \text{(R1.43)}$$

$$Br_2Cl^- \leftrightarrow Br_2 + Cl^- \quad \text{(R1.44)}$$

Reactions R1.43 and R1.44 are found to be established very quickly. The resulting BrCl and Br_2 have very low solubility and are subsequently released into the gas phase. After escape of Br_2 into the gas phase it is photolyzed (R1.45) and the Br formed then goes on to destroy O_3 (R1.46).

$$Br_2 + h\nu \rightarrow 2Br \quad \text{(R1.45)}$$

$$2(Br + O_3) \rightarrow 2\,(BrO + O_2) \quad \text{(R1.46)}$$

$2(BrO + HO_2) \rightarrow 2(HOBr + O_2)$ (R1.47)

Net: $2HO_2 + H^+ + 2O_3 + Br^- + h\nu \rightarrow HOBr + 4O_2 + H_2O$ (R1.48)

Reaction R1.47 closes the autocatalytic cycle of bromine activation. The described chemical mechanism is shown in a simplified illustration in figure 1.4.

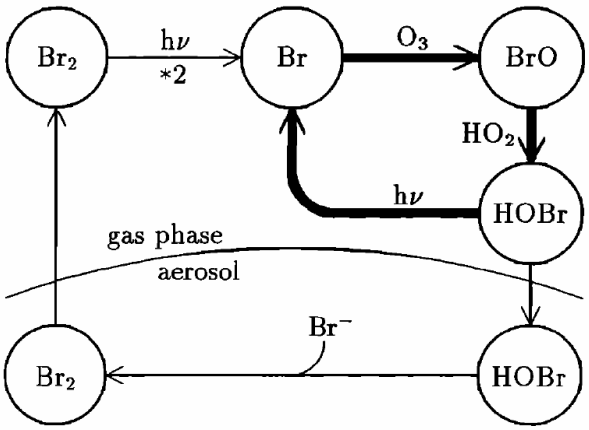

Fig 1.4 The autocatalytic cycle of bromine activation. Thin lines represent the activation of sea-salt bromide. Thick lines represent the gas-phase O_3 destruction chain (Sander and Crutzen, 1996).

1.8.3 Halogen release and pH dependence

The efficiency of halogen release is believed to be strongly pH dependant. Central to the transformation of inactive bromide to reactive gas phase bromine are reactions R1.41 and R1.42, which are only effective at acidic pH. In the MBL, freshly generated sea salt aerosol has a pH of approximately 8-9 (Sander and Crutzen, 1996). The pH can be reduced via the uptake of SO_2 or methane sulfonic acid. In polluted MBL air, the uptake of strong acids such as H_2SO_4 and HNO_3 reduces the pH to less than 2. In remote regions, the pH is expected to reach 5.5 (Keene et al., 2002).

The role of pH in the efficiency of bromine release from the aqueous phase was studied in the lab (Fickert et al., 1999). At a pH of less than 6.5, at least 90% of HOBr was released into the gas phase as Br_2. It was found that bromine was not released following uptake onto non-acidified solution. Fickert et al. concluded that a pH of less than 7 is necessary in order for halogen release to take place from the sea salt aerosol particles. High dimethyl sulphide (DMS) concentrations, which are probable in the austral summer, result in SO_2 formation in the remote MBL. The formation of SO_2 can subsequently lead to halogen activation in the MBL.

Even though the main source for halogens in the MBL is sea salt aerosol particles, Vogt et al. have suggested that sulphate particles also play an important role in bromine recycling, i.e. the transformation of HOBr and HBr to the more easily photolyzable species Br_2 and BrCl (Vogt et al., 1996). They found that the transformation is approximately an order of magnitude faster on sulphate aerosol than

on sea salt aerosol, mainly due to the higher surface area and lower pH of the sulphate aerosol.

It is important to note that due to the stronger wind speed over the Southern Ocean, sea-salt production for the latitude bands above 30 °S accounts for nearly 40% of global sea-salt production. A strong seasonal variation in the sea salt production due to the natural variability of sulphate acidity in aerosols is observed over the Southern Ocean. This is not the case over the Northern Atlantic Ocean, where due to the acidic anthropogenic pollution there is a lack of significant variability (Yang et al., 2005).

1.8.4 Field observations and model results in the MBL

Direct measurements of reactive halogen species in the MBL are very difficult as experienced by several groups in the past. However, a number of modelling studies have explored halogen chemistry in the remote MBL, even though the lack of kinetic data and missing information made solid assessments difficult.

In a recent study, Yang et al. used an off-line three-dimensional tropospheric chemical transport model (*p*-TOMCAT) to study the tropospheric bromine chemistry budget (Yang et al., 2005). Figure 1.5 shows the horizontal distribution of monthly mean surface BrO during daytime hours, 0900-1500 local time. The lowest values are over the continents (less than 0.1 ppt_v). The highest mixing ratios are found at high latitudes corresponding to high surface BrO mixing ratios. The low mixing ratios of BrO at low latitudes (less than 0.5 ppt_v) are due to the relatively weak marine wind and as a result of small sea salt Br emission.

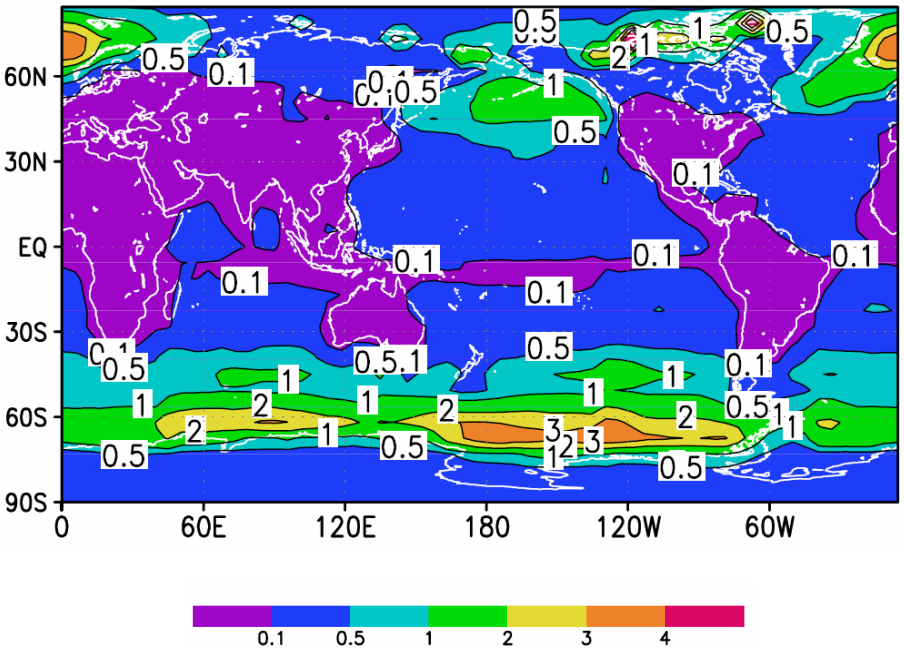

Figure 1.5 Horizontal distribution of monthly mean daytime BrO (ppt_v) in March in the model surface layer (Yang et al., 2005).

Von Glasow et al. predicted a distinct diurnal variation of BrO in low NOx regimes with the use of a one dimensional box model (MISTRA) (von Glasow et al., 2002). Peaks were seen in the morning and evening with values in the range of 2.5 – 4 ppt_v, with noontime values of 1.5 ppt_v. The diurnal variation was a result of the wavelength dependency of the chief BrO production and sink reactions. The main production reaction is the photolysis of Br_2 and BrCl which results in the production of a Br radical, which then reacts with O_3. The latter reaction is more efficient at the longer wavelength radiation, which dominate during morning and evening hours.

BrO was first detected in the MBL by Leser et al. over the northern Atlantic Ocean (Leser et al., 2003). The maximum BrO value mixing ratio measured was in the order of 2.4 ± 2.1 ppt_v. However, the averaged value was much lower at 0.7 ± 0.2 ppt_v. On quite a number of measurement days the mixing ratios lay below the detection limit of 1-3 ppt_v. Table 1.3 gives an overview of measurements of XO in various locations in the boundary layer.

Table 1.3 Measurements of XO in the BL, adapted from (von Glasow and Crutzen, 2007)

Species	Location	Max. mixing ratio(ppt_v)	References
ClO	Great salt Lake	15	(Stutz et al., 2002)
BrO	Mace Head, Ireland	6	(Saiz-Lopez et al., 2004)
	Mid. Lat. MBL	2.4	(Leser et al., 2003)
	Salt lakes (Caspian sea, Great Salt Lake)	220	(Stutz et al., 2002, Wagner et al., 2001)
	Antartic, Arctic	30	(Friess et al., 2004)
	Cape Verde	2.5	(Read et al., 2008)
IO	Mace Head, Ireland	7.2	(Saiz-Lopez et al., 2006)
	Tasmania	2.2	(Allan et al., 2000)
	Kerguelen Island	9.8	(Hönninger, 2002)
	Arctic	0.73	(Hönninger, 2002)
	Cape Verde	1.4	(Read et al., 2008)

The role of halogen compounds in the remote MBL troposphere is still an unresolved issue and major uncertainties remain in the origin and fate of halogen atoms.

1.9 Research objectives and thesis outline

It is important to note that the main difference between this study compared to previous studies is that this study was done in the remote open ocean where there is almost no influence from local pollution which is seen in continental and coastal regions of the globe. In order to avoid the possibility that results might be skewed by either local sources of pollution or other regional effects, ship born studies on the open ocean are essential, especially in a region with a low biological productivity.

Chapter two of this thesis is dedicated to the instrumental techniques used to measure NO, NO_2 and O_3. The chemiluminescence detector (CLD) deployed during the campaign is discussed in detail. The instrumental setup, sampling system and instrumental details of other relevant instruments used during the campaign are also discussed.

Chapter three covers observations in the MBL during the southern ocean cruise which took place during March 2007, subsequently referred to as MD160.

Chapter four investigates the photostationary state of NOx and O_3 in the remote southern Atlantic Ocean using the Leighton ratio. We also examine organic peroxy radicals and hydroperoxy radicals measured during the cruise and compare their concentrations with values derived from models and theoretically calculated data.

Chapter five investigates the O_3 budget based on both the theoretically assumed and measured peroxy radical concentrations in the remote MBL. O_3 production is calculated based on the PSS expression. The O_3 compensation point in the remote MBL of the southern Atlantic Ocean is also studied.

In order to achieve a direct comparison of measurement data with model output, an atmospheric chemistry general circulation model was used to simulate concentrations of trace gases along the exact MD160 cruise track. The results of the comparison are presented in Chapter six.

The last chapter of this thesis is a summary of conclusions resulting from the investigations carried out within this thesis.

Chapter 2: Instrumentation

In order to better understand the chemical and physical processes in the atmosphere, it is necessary to measure minor atmospheric components down to mixing ratios of parts per trillion. Therefore, developments of measurement techniques are essential in order to further our current knowledge of trace gases. O_3 is a photochemical pollutant and a greenhouse gas, which makes highly accurate measurements of ozone and its precursor's desirable both in aspects of global warming and air quality.

In the first part of this chapter, the current state of the art measurement methods and instrumental techniques will be briefly reviewed. In the second part, the high resolution 3-channel chemiluminescence detector (CLD) deployed during the MD160 cruise will be described in detail.

2.1 Measurement of NO and NO_2

There are a variety of techniques available for the measurement of NO and NO_2 concentrations. Since the introduction of the chemiluminescence (CL) technique by Fontijn et al., this method has been widely used to measure NO (Fontijn et al., 1970). The principle of this method is based on the detection of photons which are emitted from the excited NO_2 molecules produced as a result of the reaction of NO and O_3. This process is described in detail in section 2.2. Ridley and Howlett were the first to report a design for NO measurements at mixing ratios below $100ppt_v$ (Ridley and Howlett, 1974). There have been significant improvements and the method can now be used to detect NO at the ppt_v level.

NO_2 measurements, however, have proven to be more difficult in comparison to NO. Several methods have been developed to measure atmospheric NO_2, namely:

Photolytical conversion-chemiluminescence detection method (PLC-CL)
Metal catalytic converter-chemiluminescence detection method
Photo-fragmentation two-photon laser-induced fluorescence (PT-TP-LIF)
Luminol chemiluminescence technique (LC)
Differential optical absorption spectroscopy (DOAS)
Tunable diode laser absorption spectroscopy (TDLAS)
Laser induced fluorescence (LIF)
Cavity ring down instrument
Fourier transform

The most common technique used to measure NO_2 is the photolytical conversion (PLC) of NO_2 to NO, followed by CL detection of the converted NO (Ryerson et al., 2000). It is believed to be the most reliable system in converting NO_2 to NO and has higher selectivity than the metal catalytic converter (Gao et al., 1994). The biggest advantage of this method is that the PLC instrument is compact and easy to utilize in field campaigns. A variety of commercial PLC-CL instruments are also available, which use a Xenon arc lamp as a light source. However, the limit of detection (LOD)

of these instruments is still relatively high, on the order of 50 ppt_v for 60s integration time and a confidence interval of 1σ. A number of groups have optimized the PLC-CL method and have developed instruments with low LODs in the order of approximately 10 ppt_v (Del Negro et al., 1999). Bradshaw et al. have utilized a method which replaces CL detection of NO with a two photon laser induced fluorescence technique (Bradshaw et al., 1999). They have reported LOD of 1 ppt_v for NO_2 using a PF-TP-LIF instrument.

Another method which has been widely used to detect NO_2 is the luminal chemiluminescence technique (LC) (Wendel et al., 1983). Instruments based on this method are also commercially available. Gas phase NO_2 reacts with the luminal solution on its surface and consequentially results in fluorescence. LC is a direct and sensitive method. However, its greatest disadvantage is that it is non-specific i.e. O_3, PAN and other peroxy nitrates are also detected with high efficiency (Fehsenfeld et al., 1990).

Another method which has been developed in order to measure atmospheric NO_2 is based on the differential optical absorption spectroscopy (DOAS) technique (Platt et al., 1979). The major disadvantage of the DOAS method is the necessity of long optical paths, which causes limitations in terms of mobility and spatial resolution.

2.2 Basic principles of the CL method

The measurement principle of the CLD is based on the gas phase chemiluminescent reaction of NO with O_3 to form NO_2 in the excited state. The spontaneous deactivation of excited NO_2 (NO_2*) occurs with the emission of light (R2.3), provided that the excited state has a sufficiently short radiative lifetime and quenching through collision is kept small through low pressure in the reaction vessel (reaction 2.4). The number of photons emitted from the chemiluminescent reaction is proportional to the mixing ratio of NO. If one reactant is supplied in excess, the chemiluminescence intensity can be used to quantify the other reactant's mixing ratio. NO_2 is measured in the same way as NO, but with preceding catalytic conversion to NO. In this study, the conversion is accomplished through the use of a blue light converter (BLC), which is explained in detail in section 2.5. O_3 is measured via the inverse procedure using excess NO.

To measure the small mixing ratios of NO, the sample air is mixed with an excess of O_3 and the chemiluminescence intensity of the reaction is monitored. Clough and Trush investigated the reaction mechanisms between NO and O_3 in detail (Clough and Thrush, 1967). They reported the most important chemical reactions in this method:

$$NO + O_3 \rightarrow NO_2 + O_2 \qquad \text{(R2.1)}$$

$$NO + O_3 \rightarrow NO_2^* + O_2 \qquad \text{(R2.2)}$$

$$NO_2^* \rightarrow NO_2 + h\upsilon \qquad \text{(R2.3)}$$

$$NO_2^* + M \rightarrow NO_2 + M \qquad \text{(R2.4)}$$

The reaction rates for the above chemical mechanism were measured by Schurath et al. (Schurath et al., 1981) and are as follows:

$k_1 = 2.3 \cdot 10^{-12} \exp(-1475\ K/T)$ $[cm^3 molecules^{-1} s^{-1}]$ (Equation 2.1)

$k_2 = 2.9 \cdot 10^{-12} \exp(-1951\ K/T)$ $[cm^3 molecules^{-1} s^{-1}]$ (Equation 2.2)

$k_3 / k_4 = 1.3 \cdot 10^{14}$ $[molecules\ cm^{-3}]$ (Equation 2.3)

The fraction of NO_2* resulting from the reaction between NO and O_3 (reaction 2.2) at 25 °C is calculated as:

$$\frac{k_2}{(k_1+k_2)} = 0.2 \quad \text{(Equation 2.4)}$$

The fraction of NO_2* molecules which emit light as a result of spontaneous deactivation, at 25 °C and 6 hPa, are calculated as:

$$\frac{k_3}{(k_3+k_4*[M])} = 8.9*10^{-4} \quad \text{(Equation 2.5)}$$

In the equation above, [M] is the number density in the reaction chamber with the unit molecules·cm^{-3}. From equations 2.4 and 2.5 it is concluded that only approximately 0.02 % of the reaction between NO and O_3 leads to chemiluminescence (Hegglin, 2004). This indicates the need for the optimization of the dimension, geometry and reflectivity of the reaction chamber in order to guarantee that the majority of photons produced through chemiluminescence reactions are detected by the photomultipliers (PMT). In parallel the small number also reflects the need for the use of high sensitivity PMTs. In order to keep collisional quenching low and to reach a high quantum yield, the reaction chamber pressure of the CLD is maintained at approximately 12.6 hPa.

In each channel, a PMT converts the light energy (photons) into electrical impulses. These are accumulated by a counter over a specified integration time interval.

The measured intensity (S_{NO}) is obtained through:

$$S_{NO} = F_{NO} * \chi_{NO} \quad \text{(Equation 2.6)}$$

where F_{NO} represents the sensitivity of the analyzer and χ_{NO} represents the mixing ratio of the reactant. The sensitivity is determined through calibrations which are described in section 2.4. It is dependant on the mass flow through the reaction chamber and slightly dependant on the PMT temperature.

The total measurement signal (S_{tot}) includes the S_{NO} signal, an interfering signal (S_I) and also a signal produced by the dark current of the PMT (S_D). S_I is produced through the reaction of interfering atmospheric compounds with O_3. Therefore the total signal consists of:

$$S_{tot} = S_{NO} + S_I + S_D \quad \text{(Equation 2.7)}$$

To account for S_I and S_D, CL detectors are operated in two modes: the pre-chamber and main-chamber mode. During the main-chamber measurement mode O_3 is supplied directly into the sample air at the main-chamber inlet. The reaction-chamber pressure, volume and flow rate are optimized in a way to ensure that the NO oxidation reaction happens directly in front of the PMT. The total signal resulting from the main chamber reaction is referred to as S_{main}. In the pre-chamber mode O_3 is fed into the sample air at the inlet to the pre-chamber located upstream of the main chamber (see figure 2.1). The reaction between NO and O_3 is approximately two orders of magnitude faster than any other known CL reactions with O_3 (Volz and Drummond, 1984). The chemiluminescence produced by the fast reaction between NO and O_3 occurs to a large fraction in the pre-chamber, where it cannot be detected by the PMT of the main chamber. The pre-chamber signal, S_{pre}, therefore only consists of S_D and the slow interfering chemiluminescence reactions, S_I. A very small fraction of the NO + O_3 signal ($\alpha * S_{NO}$) may still be detected by the PMT and therefore may need to be accounted for. The above considerations can be summarized in the following equations:

$$S_{main} = S_{NO} + S_I + S_D \quad \text{(Equation 2.8)}$$

$$S_{pre} = (\alpha * S_{NO}) + S_I + S_D \quad \text{(Equation 2.9)}$$

The subtraction of the pre-chamber signal (equation 2.9) from the main chamber signal (equation 2.8) leads to the elimination of the S_I and S_D:

$$S_{main} - S_{pre} = (1-\alpha) * S_{NO} \quad \text{(Equation 2.10)}$$

Equation 2.11 is obtained through the combination of equations 2.6 and equation 2.10:

$$[NO] = \frac{S_{main} - S_{pre}}{(1-\alpha * F_{NO})} \quad \text{(Equation 2.11)}$$

The mixing ratio of NO can be obtained through equation 2.11. Both F_{NO} and α can be determined by calibration with a known amount of NO calibration standard. In the equation below, S_{pre}^{NO} and S_{pre}^{SA} represent pre-chamber signals during NO calibration and background measurement with synthetic air (SA) respectively. S_{main}^{NO} is the main chamber signal during the NO calibration:

$$\alpha = \frac{S_{pre}^{NO} - S_{pre}^{SA}}{S_{main}^{NO}} \quad \text{(Equation 2.12)}$$

2.3 The ECO-Physics CLD 790 SR

The instrument used on the MD 160 cruise is a high resolution and high sensitivity 3-channel CLD (ECO-Physics CLD 790 SR). It is equipped with three measurement channels, which are independent of one another allowing simultaneous in-situ measurements of NO_2, NO and O_3.

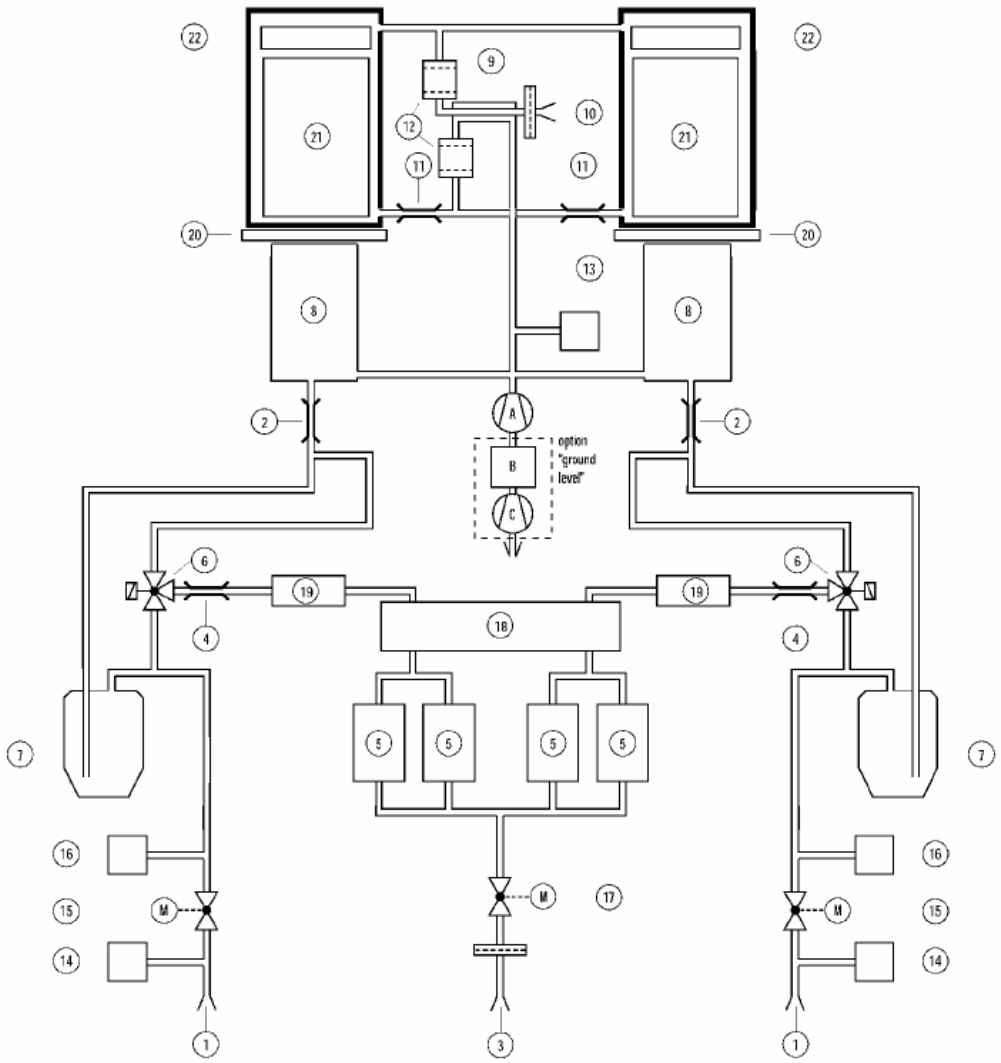

Figure 2.1 Schematic of a 2-channel CLD 790 SR (source: ECO Physics CLD 790 SR manual, ECO Physics, Switzerland). The two channels above are for NO and NO_2 measurements. (A) Scroll pump, (B) ozone scrubber, (C) membrane pump, (1) sample inlet, (2) sample flow restrictor, (3) O_2 inlet with filter, (4) ozone flow restrictor, (5) ozone generators , (6) solenoid valves, (7) pre-chambers, (8) main chamber, (9) permeation tube, (10) dry air inlet with filter, (11) PMT flushing outlet with flow restrictor, (12) filter with drying agent, (13) pressure sensor "reactor", (14) pressure sensor "inlet", (15) pressure regulator "sample", (16) pressure sensor "back", (17) pressure regulator, O_2 inlet , (18) damper, (19) pre-volume, (20) red filter, (21) photomultiplier (PMT), (22) high-voltage module.

The instrument was originally manufactured as a two channel system by ECO Physics, Inc. Dürnten, Switzerland. However, the instrument has been modified and optimized to a great extent, in order to improve the resolution and sensitivity needed

for use in unpolluted regions of the atmosphere. The modifications include the addition of a third channel for the measurement of O_3 and optimization in some of the main components of the instrument. The modifications were designed and carried out within the Optical Spectroscopy Group at the Max-Planck Institute for Chemistry, Mainz. The basic principles have already been discussed in detail in the last section. The sampling and subsequent measurement will be described here. Letters and numbers in this section refer to figure 2.1 which is a schematic of a 2-channel CLD. In the modifications to the instrument, the pressure regulator (15) and sensor (16) have been replaced by a mass flow controller. The third channel (O_3 channel) has the same construction principle as the other two channels (NO and NO_2 channel) lacking only the pre-chamber and ozone-generators.

A scroll pump (A) evacuates the main chamber and thereby results in a vacuum which facilitates the flow of air through the CLD. An additional membrane pump is used for measurements done on board the MD160 cruise due to the long sampling line. The inlet pressures are controlled by flow restrictors (2) and mass flow controllers which maintain a constant mass flow of 1.5 SLM per channel through the reaction chambers of the NO and NO_2 channel. The O_3 channel has a flow rate of 0.3 SLM. O_3, which is the reactant for the NO measurements, is generated by ozone-generators (5) from pure oxygen (purity 5.0, Air Liquide, Germany) added to the sample air. The rate of this addition is approximately 250 sccm per channel.

The measurements during the MD 160 cruise were conducted in a quasi-continuous mode. In each cycle, 6 pre-chamber measurements were followed by 24 main chamber measurements. Therefore the duration of the pre-chamber mode was 12 s then a switch to the main chamber mode was made for a period of 48 s. Therefore a complete cycle of pre-chamber and main-chamber mode was 60 s in total.

The dark current signal of the instrument (S_D) is dependent on the PMT temperature. For this reason the PMTs (21) are cooled down to around -30 °C which decreases the dark current signal effectively. To inhibit condensation and consequent freezing of the PMTs, which could result in a possible electrical flashover, the PMT housing is flushed with dry air continuously. For this purpose, ambient air passes through a filter (10) into a permeation tube (9) where it is dried to a dew point below -40 °C. The air subsequently passes through a filter with a drying agent (12), in this case silica gel filters. The dry air flow is kept constant via a flow restrictor (11).

Reactions of O_3 with the adsorbed compounds on the chamber walls may contribute to the interfering signal, S_I. A layer of polished gold covers the inside of the pre-chambers (7) and the main chambers (8) to reduce these effects and also to increase reflectivity.

The spectrum emitted by excited NO_2 molecules ranges from 500 to 3100 nm. A red filter (20) positioned between the reaction chamber and the PMT blocks the radiation below 600 nm, removing a large fraction of the photons produced by interfering compounds and ensuring optimal NO selectivity.

The third channel used for the O_3 measurement follows the same construction principle, lacking only the pre-chamber and the ozone generators. For the O_3 measurement, excess NO in N_2 ([2.046 ± 0.041] Volume-%, Air Liquide, Germany) was added from a gas bottle.

2.4 Calibration System

The performance of the three channels is somewhat influenced by changes in the operating conditions. In order to ensure data quality, the instrument was calibrated several times during the campaign by the addition of standard gas directly to the sample lines of the three channels. Gas bottles, mass flow controllers and valves were part of the calibration set-up. They were either located directly on the CLD rack or, in the case of the O_3 calibrator, standing next to the rack.

The sensitivity of the CLD is defined by its response in counts to an NO signal and is determined by calibration gases with known mixing ratios. During the MD 160 cruise, NO in N_2 ([2.191 ± 0.044] Vol-ppm_v, Air Liquide, Germany) was used as a calibration gas. The gas had a flow of 3.93 sccm and was diluted to mixing ratios of approximately 2 ppb_v by synthetic air (SA). This standard was compared to a primary standard ([4.83 ± 0.05] ppm_v, NIST, USA) after the campaign. Synthetic air was supplied during the campaign from a gas bottle (Air Liquide, Germany) which was additionally filtered by a PURAFIL cartridge. The sensitivity of the NO and NO_2 channels were calibrated a minimum of once per day.

The O_3 channel was calibrated using a commercial O_3 calibrator, (model TE49C, Thermo instruments GmbH, Germany) several times during the campaign. The only gas required for this measurement is SA which is fed directly into the O_3 calibrator. Subsequently, O_3 is produced by the O_3 calibrator based on the specified set points e.g. 0 ppb_v, 10ppb_v, 20 ppb_v…100 ppb_v, etc. The value measured by the CLD is read and compared to the actual set point value of the O_3 calibrator.

The background signal of the channels was determined with SA measurements. The NO channel produced an average background signal of approximately 1 ppt_v. The NO_2 channel, however, produced an average background signal of 15 ppt_v. This is discussed in section 2.5. The background signal was corrected for in the data.

The detection limit (DL) of a measured species is defined as the lowest detectable mixing ratio that an analyzer can measure. The DL of the measured species in this study was determined based on the reproducibility of the SA measurements carried out on a daily basis throughout the campaign. The DLs determined based on a 2σ confidence level and 60s integration time are 0.47 ppt_v, 0.51 ppt_v, and 18.2 ppt_v for the NO, NO_2 and O_3 channel respectively.

Noteworthy is the fact that for measurements carried out in the pristine background MBL during the MD160 cruise, the actual NO mixing ratios at night were close to 0 ppt_v. This is due to the complete conversion of NO to NO_2 and NO_3. Due to the lack of solar radiation at night, the back-conversion of NO_2 to NO does not take place and therefore in a remote location with no local sources of NOx, the NO mixing ratio is expected to equal zero. In this study, the measured night time values were compared to the STDEV of the SA measurements. Observations showed that they were in very good agreement; this indicates the good quality (purity) of the synthetic gas. As mentioned above, the night time values of NO are expected to equal zero, however due to instrumental offset, circa 1 ppt_v, they are close to zero.

Precision describes the reproducibility of a measurement, i.e. how close the values are together. The precision of the NO, NO_2 and O_3 channels deduced from the sum of the DL and the reproducibility of the infield calibrations was 0.47 ppt_v + 2.68 % (of total reading) for NO, 0.51 ppt_v + 2.68 % for NO_2, and 0.02 ppb_v + 1 % for O_3.

The accuracy of a measurement is defined as the nearness to the 'true' value. The accuracy in this study is calculated based on the total sum of accuracy of the calibration standard used and also the uncertainty due to the offset corrections. The accuracy for the NO_2 channel additionally contains the uncertainties in the conversion efficiency of the BLC. The accuracy is 1.4 ppt_v + 2 % for the NO channel, 1.5 ppt_v + 2 % for the NO_2 channel and 0.5 ppb_v for the O_3 channel.

The overall uncertainty of the mixing ratio of a species can be determined by use of the error propagation equation:

$$(\Delta C)^2 = \left(\frac{\partial C}{\partial E_1}\Delta E_1\right)^2 + \left(\frac{\partial C}{\partial E_2}\Delta E_2\right)^2 + \left(\frac{\partial C}{\partial E_3}\Delta E_3\right)^2 + \ldots \qquad \text{(Equation 2.13)}$$

In the above equation, E_x represents the different parameters with their uncertainties (ΔE_x). Therefore the total uncertainty based on the calculations of precision and accuracy is 1.5 ppt_v + 3.3 % (of total reading) for the NO channel, 2.2 ppt_v + 5.3 % for the NO_2 channel and 0.5 ppt_v + 1 % for the O_3 channel.

2.5 Principles of the blue light converter

The blue light converter (BLC) is a solid state photolytic NO_2 converter. The BLC used on the MD160 cruise was manufactured by Droplet Measurement Technologies, Colorado, USA. It uses an array of ultra violet light emitting diodes (UV-LED's) to photolyze NO_2 to NO at a wavelength of approximately 395nm:

$$NO_2 + h\upsilon \rightarrow NO + O \qquad \text{(R2.5)}$$

High specificity is achieved by the narrow spectral output of the LEDs. The peak absorption cross section for NO_2 is approximately reached at 390-400nm and that wavelength is also the wavelength range of the LEDs. This eliminates the conversion of potential interfering species such as HONO and NO_3, see figure 2.2.

The volume of the BLC photolysis cavity is nominally 17 mL, which provides a 1 s residence time at a flow rate of 1 SLM. The conversion efficiency (CE) of the BLC depends strongly on the residence time of the air sample in the cell. The residence time is a function of both cell flow and cell pressure. Lower pressure levels, result in shorter residence time inside the BLC and as a result lead to a decrease in the CE. Therefore, the CE of the BLC is highest at sea level pressure. The CE is also affected by the flow rate. High flow rates result in less residence time within the BLC and consequently lead to a lower CE. The efficiency of the converter was determined by gas phase titration (GPT) of NO with O_3, several times before and during the campaign using a GPT instrument (ANSYCO GmbH, Karlsruhe, Germany).

This calibration technique is based upon the rapid gas-phase reaction between NO and O_3 to produce stoichiometric quantities of NO_2 in accordance with the following equation:

$$NO + O_3 \rightarrow NO_2 + O_2 \qquad \text{(R2.1)}$$

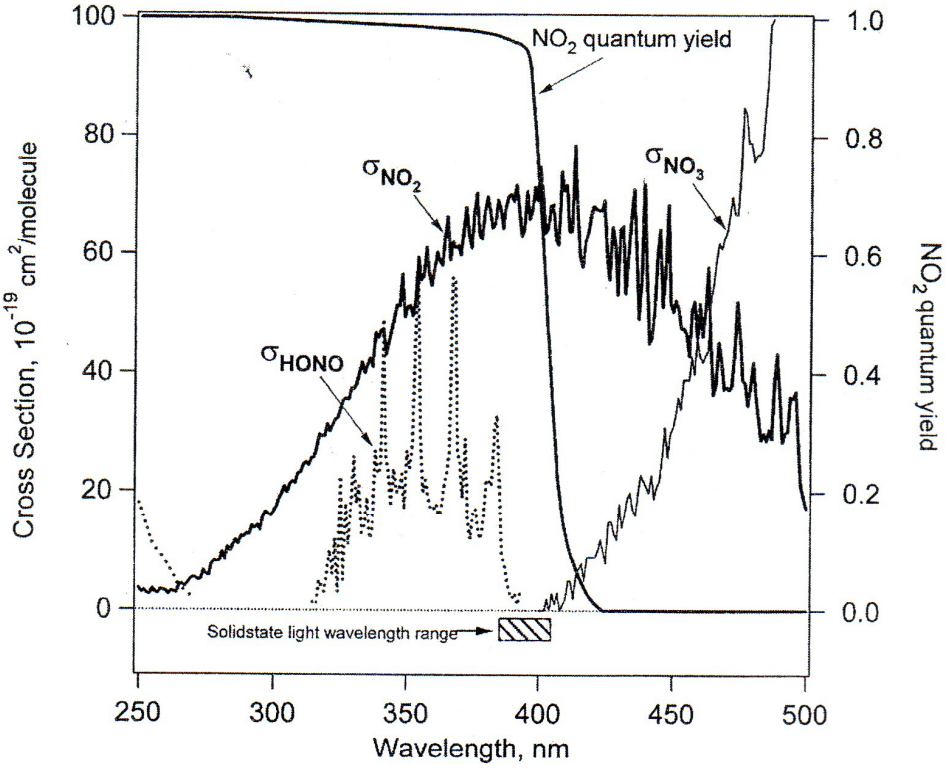

Figure 2.2 BLC spectral information. The solid state light wavelength range of the LED's eliminates the affect of interfering species (source: BLC instrument manual, Droplet measurement technologies, USA).

For this purpose both SA and NO calibration gas were used. The quantitative nature of this reaction is such that when the NO concentration is known, the concentration of NO_2 can be determined. O_3 is added to NO in a dynamic calibration system, and the NO channel of the CL detector is used as an indicator of changes in NO concentration. A UV lamp is located inside the GPT instrument for the purpose of generating O_3. Upon addition of O_3, the decrease of NO concentration observed in the calibrated NO channel is equivalent to the concentration of NO_2 produced. From these values the CE of the BLC can be estimated.

It was observed that the efficiency of the BLC did not change significantly through the course of the campaign. The CE is a parameter that is used to calculate the NO_2 from the NOc value and NO which are measured by the CLD. The relation between these three terms is expressed as the following:

$$NO_2 = (NOc-NO)*CE \qquad \text{(Equation 2.14)}$$

The CE of the BLC used during the MD160 cruise changed slightly over time. In the beginning of the campaign it was 58 %, this number changed to 59 % towards the end of the campaign with an uncertainty of (±1.8 %). The uncertainty due to the noise was a factor of two higher in the beginning of the campaign. On several occasions during the campaign the BLC was switched off for short periods of time during background measurements and calibration periods. No change was evident in the concentrations measured during calibration periods with the switching on and off of the BLC.

During the background measurements, an offset of 15 ppt_v was observed. This offset decreased substantially once the BLC was switched off. The cause of this offset is not known, but it may be due to out gassing from the silica gel, which the LEDs are embedded in, at the opposite ends of the BLC device. The offset was corrected for in the dataset.

2.6 Instrumental set up and sampling system

Due to campaign taking place in the remote MBL, much time was spent on organization and preparation of the instrumentation, required materials and spare parts prior to the start of the campaign. Due to space limitations inside the container the CLD instrument and its components had to be set up in a space efficient manner inside a rack. The rack was secured to the floor and walls of the container, to prevent shifting due to the rolling of the ship. Safety standards for the materials used for electronic components, the gas bottle racks and compressed air regulators were met. The CLD instrument was set up inside a container which was located on the deck of the ship. Two alarm systems were installed within the container in case of gas leakage in the measurement system, which represents a toxic hazard. Air was sampled through a polytetrafluoroethylene (PTFE)/Teflon inlet line which was mounted on top of the atmospheric mast at a height of 10m above the foredeck and approximately 20-25m above the sea surface (figure 2.3). From there, an inlet line was installed to the container. The Teflon inlet line was placed inside black tubing in order to prevent photochemistry taking place in the inlet line. The total length of the inlet line was 17.1m and consisted of ½ inch Teflon tubing (outer diameter). The last meter of the inlet line consisted of ¼ inch Teflon tubing.

Figure 2.3 The position and setup of the inlet line on the atmospheric mast during the MD 160 cruise.

During the campaign, the membrane pump maintained a flow rate of 19.2 SLM. The CLD preserved a total flow rate of 2.25 SLM through the use of a scroll pump. A peroxide analyser (Aero-laser AL2021) shared the inlet line with the CLD instrument

and maintained a flow rate of 3 SLM. Therefore a total flow rate of 24.45 SLM was maintained in the inlet line. This corresponds to a retention time of 3.4 seconds. The data was corrected for the residence time.

Calibrations for the inlet line were carried out using a commercial GPT instrument. The standard GPT procedure is carried out once in front of the inlet line and another time without the inlet line, directly connected to the instrument. Through a series of steps and comparison of the measured values in the two mentioned modes, the amount of NO lost in the line can be estimated. In this campaign it is estimated that NO loss due to residence in the inlet line is less than 2 %.

2.7 Electrical and electronic system

The CLD instrument is equipped with a serial port interface, allowing the instrument to be connected to a computer for data collection and remote control. The operation of the instrument is facilitated by an extensive computer program. The computer stores the measured data and instrumental parameters. The computer also controls the switching of the valves for different calibration modes and stores the set-points of the mass flow controllers. The voltage of the electrical power supply to the CLD is kept at a constant value of 28 Volts.

2.8 Instrumental details of other relevant instrument

In the course of data analysis, several parameters measured with other instruments were used. The most important details of the instruments are given below:

OH and HO_2 were measured with the HORUS instrument (HydrOxyl Radical measurement Unit based on fluorescence Spectroscopy), which uses laser-induced fluorescence (LIF) of the OH molecule, based on the fluorescent assay by gas expansion (FAGE) technique. A detailed description of the instrument is given elsewhere (Martinez et al., 2008). The time resolution for OH and HO_2 data was 10s. Precision for 60 s integration time and a confidence level of 1σ is 0.017 ppt_v for OH and 0.1 ppt_v for HO_2. The accuracy is ±35 % for a confidence level of 2σ. The detection limit of this instrument is defined as 2σ precision, assuming it is limited by the background noise (Dr. M. Martinez, personal communication, 2009).

The photolysis rate of NO_2, JNO_2, was measured using two (up- and downward) 2π-steradian (sr) filter radiometers (Meteorologie consult GmbH, Germany), and thus providing 4π-sr photolysis rates. This instrument has a precision of 5 % for 1 s data and an accuracy of 10 %. The commercially built JNO_2 radiometer determines the rate of the in-situ NO_2-photolysis in the atmosphere via a continuous measurement of the actinic flux in the appropriate wavelength of the 4π-steradian-hemisphere. The basic design is adapted from the device described by Junkermann et al. (Junkermann et al., 1989). The principles of JNO_2 filter radiometry are explained in detail by Volz-Thomas et al. (Volz-Thomas et al., 1996). Modifications have been made so that the dependence of the output signal on the angle of the incident light is minimized by using a set of quartz diffusers. The radiometer is insensitive to atmospheric parameters and does not consist of any moveable parts. The radiometer is annually

calibrated at the research centre KFA-Jülich using a set of master radiometers. Long term calibrations of this type of filter radiometer shows a small variation (below 2 %, 1σ) during one year.

O_3 was also measured during the campaign by a UV-absorption instrument (Thermo-Electron, model 49C, USA) every minute. Air was sampled from an inlet at the top of the atmospheric mast. This type of instrument has shown good stability and reproducibility (Gros et al., 1998). The estimated uncertainty is better than 5 % for this instrument. The UV instrument was calibrated after the cruise at the world calibration centre for surface ozone, carbon monoxide and methane (hosted at Empa, Duebendorf, Switzerland) and a correction factor was applied to the data set. A comparison between O_3 measured via the UV method and the CL method showed a very good agreement between the two data sets.

ROx was measured using a peroxy radical chemical amplifier (CA). The CA technique was introduced by Cantrell in the early 1980s and has been widely used since then (Parker et al., 2009). The detectors were calibrated by the addition of NO_2 and the chain length was calibrated by addition of known concentrations of CH_3O_2. The instrument was placed directly on top of the atmospheric mast above the foredeck. The sensitivity of the PERCA instrument to humidity is well known therefore a water correction has been applied to all data in this work (D. M. Brookes, personal communication, 2008). In principle, a data point was obtained every minute, however, due to calibrations, measurements are only available every other minute. PERCA data is only available from March 14th onwards due to instrumental failure in the beginning of the campaign. The uncertainty in the PERCA measurements leads to a calculated accuracy of 36 %.

The uncertainty and DL of the instruments are summarized in table 2.1. For each measurement the accuracy is determined by the larger of the two values (ppt_v or %).

Table 2.1 Total uncertainty of relevant instruments used in the PSS investigation

Parameter	Instrument	Uncertainty	Detection limit
NO	CLD	1.5 ppt_v+ 3.3 % (±2σ-60sec)	0.47 ppt_v
NO_2	CLD and BLC	2.2 ppt_v + 5.3 % (±2σ-60sec)	0.51 ppt_v
O_3	CLD	0.5 ppb_v+ 1 % (±2σ-60sec)	18.2 ppt_v
JNO_2	Filter radiometer	11 % (2σ,1sec)	$1.5x10^{-6}$ (s^{-1})
HO_2	LIF instrument	0.1 ppt_v + 35 % (±2σ-10s)	0.2 ppt_v
OH	LIF instrument	0.017 ppt_v + 35 % (±2σ-10s)	0.034 ppt_v
ROx	PERCA	10 ppt_v + 36% (±2σ-60sec)	10 ppt_v

Chapter 3: Observations in the marine boundary layer

The Marion Dufresne southern ocean cruise is referred to as the MD 160 cruise which took place during the late Austral summer. It is part of the OOMPH project (**O**cean **O**rganics **M**odifying **P**articles in both **H**emispheres). The MD 160 cruise began on March 1st, 2007 in Punta Arenas, Chile (70.85°W, 53.12°S) and ended on March 23rd, 2007 in La Reunion Island (55.36°E, 21.06°S). The research vessel crossed the southern Atlantic Ocean from west to east between approximately 60°S to 20°S. This region of the globe is dominated by prevailing strong Westerlies and is well-known for severe weather and sea conditions, often referred to as the 'Roaring Forties' and 'Furious Fifties'.

3.1 Navigation route and cruise conditions

The cruise track is shown as a white line in figure 3.1. The ship left Punta Arenas, Chile on the 01.03.2007, heading southeast until 09.03.2007 (26°W, 59°S). From there, the ship headed northeast towards South Africa, with the final stop in La Reunion Island.

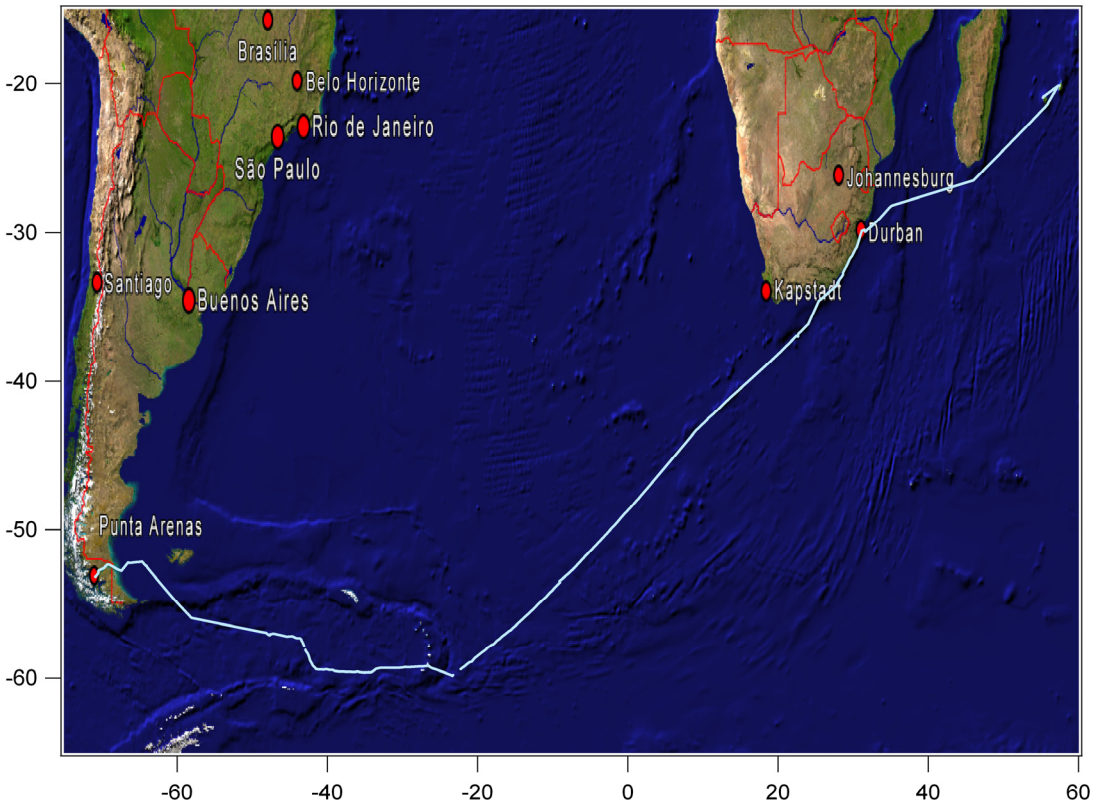

Figure 3.1 The white line represents the MD 160 cruise track. Marion Dufresne crossed the southern Atlantic Ocean from west to east between approximately 60 °S to 20 °S.

During the first part of the campaign, drifting icebergs from Antarctica were often seen and extremely cold air over the cold water of the polar oceans was encountered

During this period, there was also extensive cloud cover with periods of rain and to a lesser extent snow. This was in contrast to the second part of the campaign, when the ship cruised towards the African continent and as a result temperatures and actinic flux both increased. The NOx and reactive hydrocarbon concentrations measured during the campaign are among the lowest concentrations reported to date. On the MD 160 cruise, the prevailing wind direction was westerly, with wind speeds varying in strength from windless conditions to a maximum speed of 33 m s^{-1}. Gale force winds (>17 m s^{-1}) occurred occasionally during the cruise and the average wind speed was 10 m s^{-1} for the first half and 8 m s^{-1} for the second part of the campaign.

3.2 Back trajectories for MD160 cruise

Meteorological data and models allow the calculation of back trajectories for the encountered air masses during the cruise. Back trajectories show how an air parcel likely travelled prior to arrival at a specific site, i.e. the ship track in this study. They are an important tool in determining the origin and emission history of a given air mass. Back trajectories for the MD 160 cruise were provided by Prof. H. Wernli (University of Mainz, Germany). Meteorological data and the LAGRangian ANalysis TOol (LAGRANTO) were used to calculate the 10 day back trajectories (Wernli and Davies, 1997).

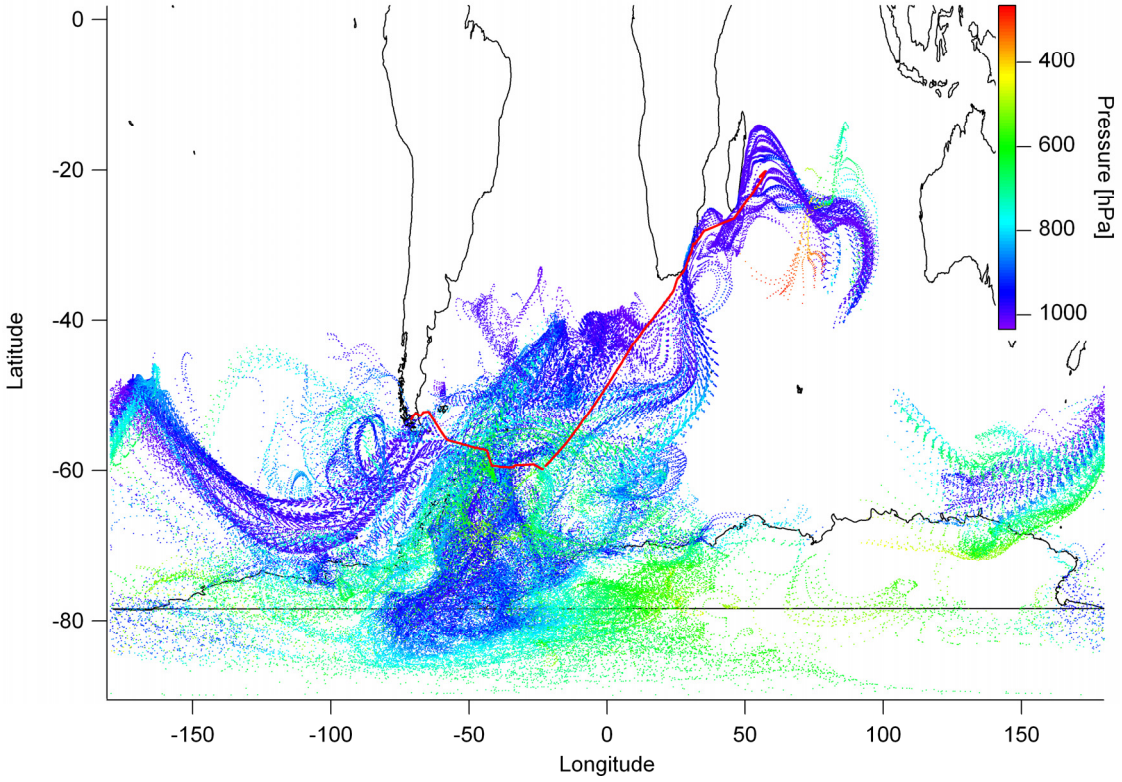

Figure 3.2 Air mass 10 day back trajectories of the cruise track for MD160. Trajectories were plotted using ITOSA, an IGOR™ based program developed by Dr. S. Wong-Zehnpfennig at the Max Planck Institute (MPI) for chemistry in Mainz.

Every 3 hours about 10 trajectories were started within a ± 30 minute time interval at the ship's position along the cruise track. The path of the trajectories was calculated using three-dimensional wind fields from the European Centre for Medium-Range Weather Forecasts (ECMWF). For the analysis, 6 hourly operational global analyses were complemented by intermediate 3 hourly forecasts interpolated onto a horizontal grid with a resolution of 1° latitude and 1° longitude. The horizontal resolution of the model was 25 km using 91 vertical levels. The computational time step for trajectory calculations was 30 minutes. All back trajectories calculated for MD 160 are plotted in figure 3.2. The 10 day backward trajectories show air mass origins from the southern Atlantic Ocean until March 21st. This air mostly comes from the free troposphere, subsiding to the boundary layer some time before measurement. However, air masses from within the boundary layer or lower pressure levels (300-400 hPa) were also found. Back trajectories for specific photostationary state study periods are presented in Chapter four. Since the majority of the time the air masses were transported directly from the Antarctic continent, therefore the likelihood of anthropogenic contamination is highly improbable.

3.3 Acquired data

A number of parameters were measured during the MD 160 cruise. The most common meteorological parameters were measured including sounding balloons, Laser Detection And Ranging (LIDAR) measurements, flux measurements and calculations of air flow dynamics and turbulence around the ship, the inlets and probe systems were performed. In-situ gas phase measurements included O_3, CO, OH, HO_2, ROx, NO and NO_2 concentrations as well as organic species like DMS, isoprene and halocarbons. Additional air samples were collected twice a day in electro-polished stainless steel canisters for subsequent VOC analysis. Instrumental details of relevant instruments used in this study have already been described in Chapter two.

Biological oceanic monitoring included the sampling of seawater several times a day for characterization as well as the determination of chemical and physical parameters, such as sea salinity, surface temperature and CO_2 concentrations. For aerosol chemical composition measurements, an Aerodyne High-Resolution-Time-of-Flight (AMS) was used to measure mass concentrations and species-resolved size distributions of non-refractory aerosol components in the submicron range (Zorn et al., 2008). For more information see www.atmosphere.mpg.de/enid/oomph.

3.4 Observations of NO, NO_2, O_3 and JNO_2

During the campaign, data was obtained by the chemiluminescent detector (CLD) from March 5th to March 20th, 2007. The CLD instrument ran the entire period of the campaign without any complications. Depending on the wind direction and course of the ship, the sampled air was occasionally contaminated by the ship's own stack emission. These events were automatically removed through a series of filtering steps which are described in detail in section 3.5. In figure 3.3, an overview of the ambient mixing ratios of NO, NO_2 and O_3 measured along the ship track by the CLD is presented. Missing data due to calibration is indicated with the grey boxes.

Figure 3.3 Time series of NO, NO_2 and O_3 mixing ratios measured on MD 160 with the CLD.

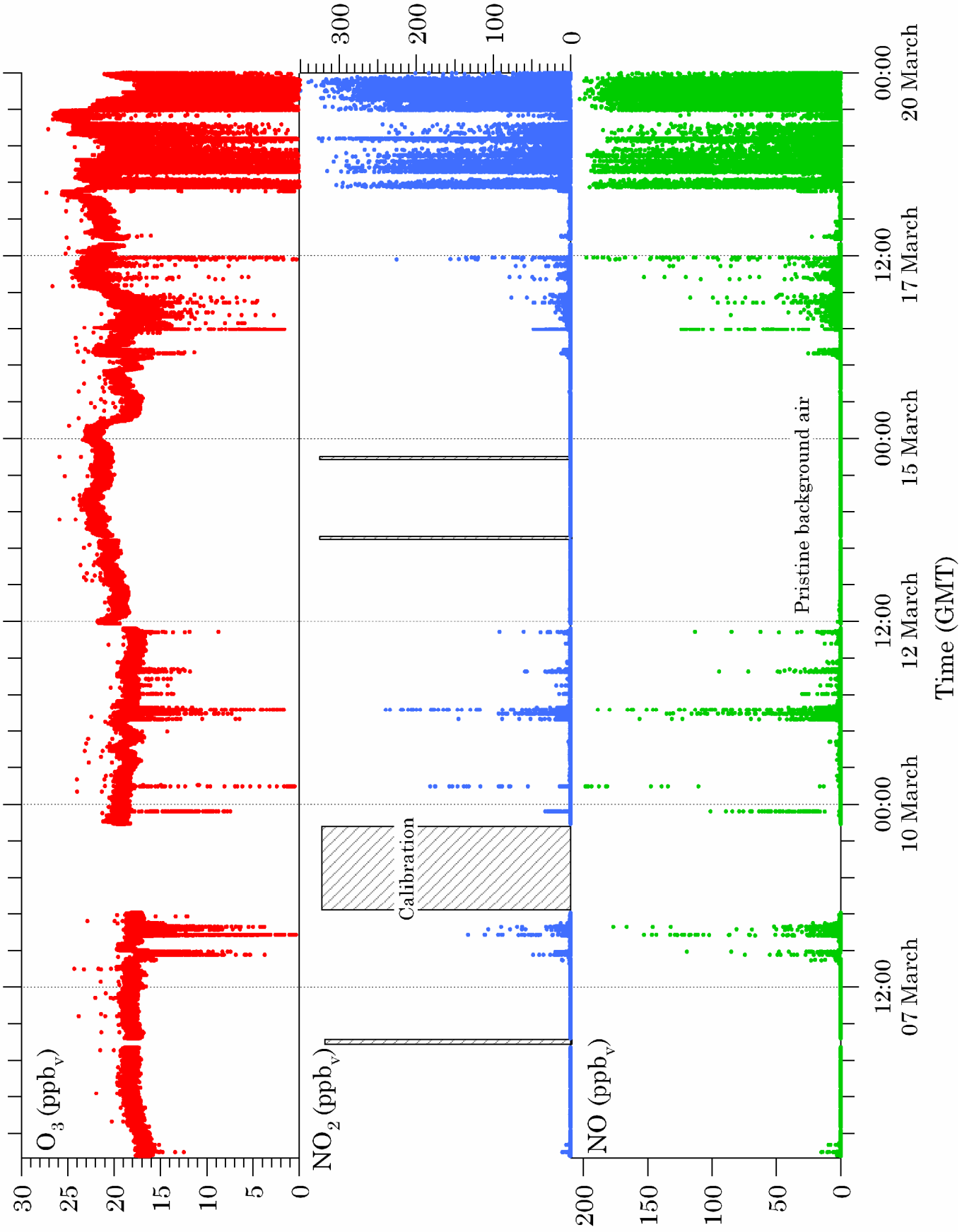

In this figure, all data is included and data has not yet been filtered, with the exception of calibration data, which has been removed and shaded with grey boxes. Data used to plot figure 3.3 are the original two second data.

Sharp spikes in the NO, NO_2 data and dips in the O_3 data in figure 3.3 correspond to contamination periods by the ship's own stack smoke. During these contamination periods, an excellent anti-correlation between NO_2 and O_3 can be seen in the data. This is expected, as the emitted NO titrates away the O_3 and produces NO_2 (R1.3).

An overview of the filtered NO data for the clean background conditions of the MBL is presented in figure 3.4. Note that the unit in figure 3.3 is ppb_v, while in figure 3.4 the NO mixing ratios are presented in ppt_v. It can be observed that the background NO mixing ratios was zero during the night. After sunrise, NO_2 is photo-dissociated to NO, resulting in an increase in the NO mixing ratio.

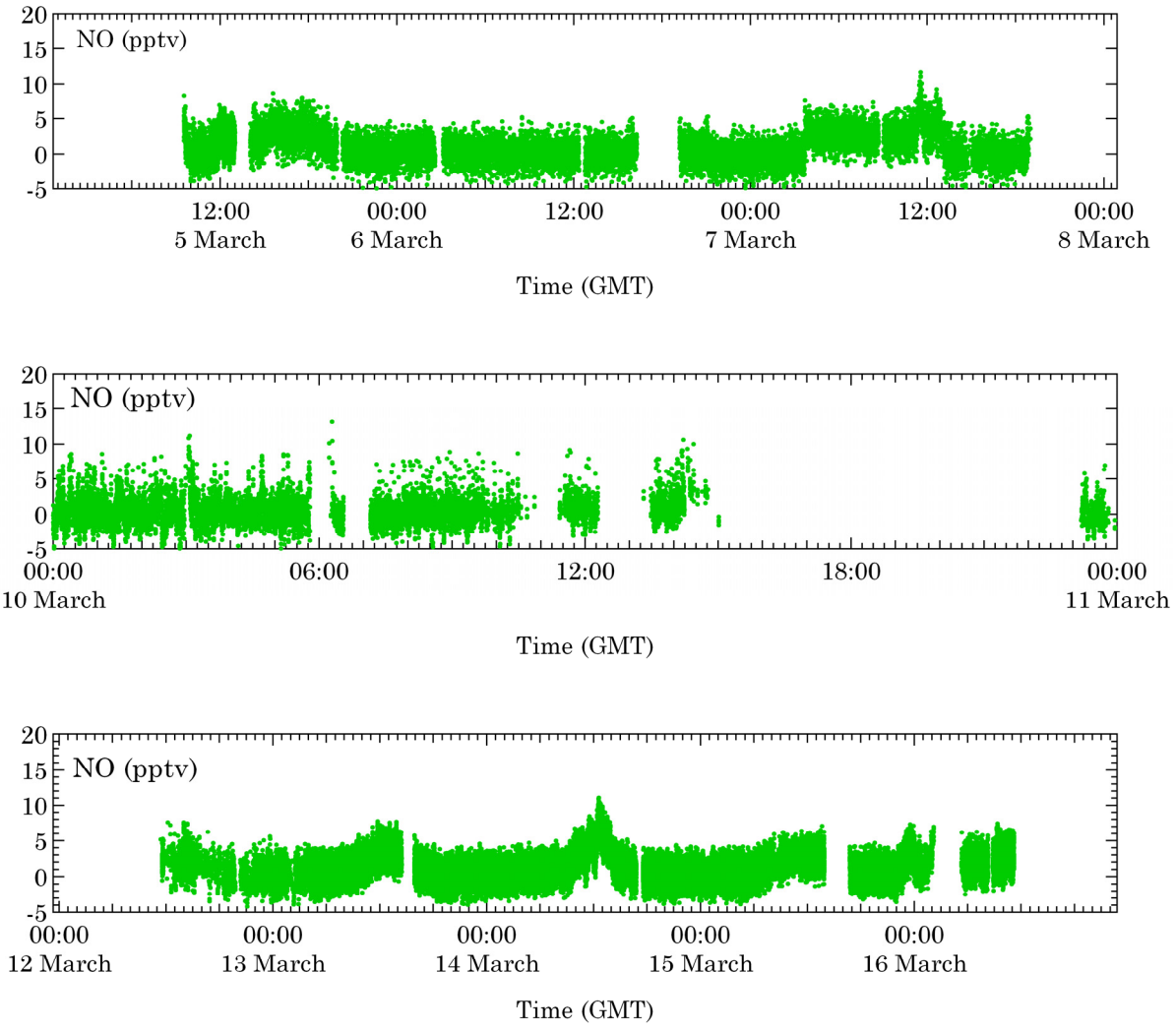

Figure 3.4 Zoom-in on the filtered NO data from figure 3.3 for several different periods, illustrates the low concentrations of NO in the clean background conditions of the MBL (2s data).

JNO_2 was also measured by the Optical Spectroscopy group during MD160 (see figure 3.5). JNO_2 can represent the degree of clearness of the sky. Spikes in the JNO_2 data, cause deviations from the bell shape and correspond to shading caused by clouds.

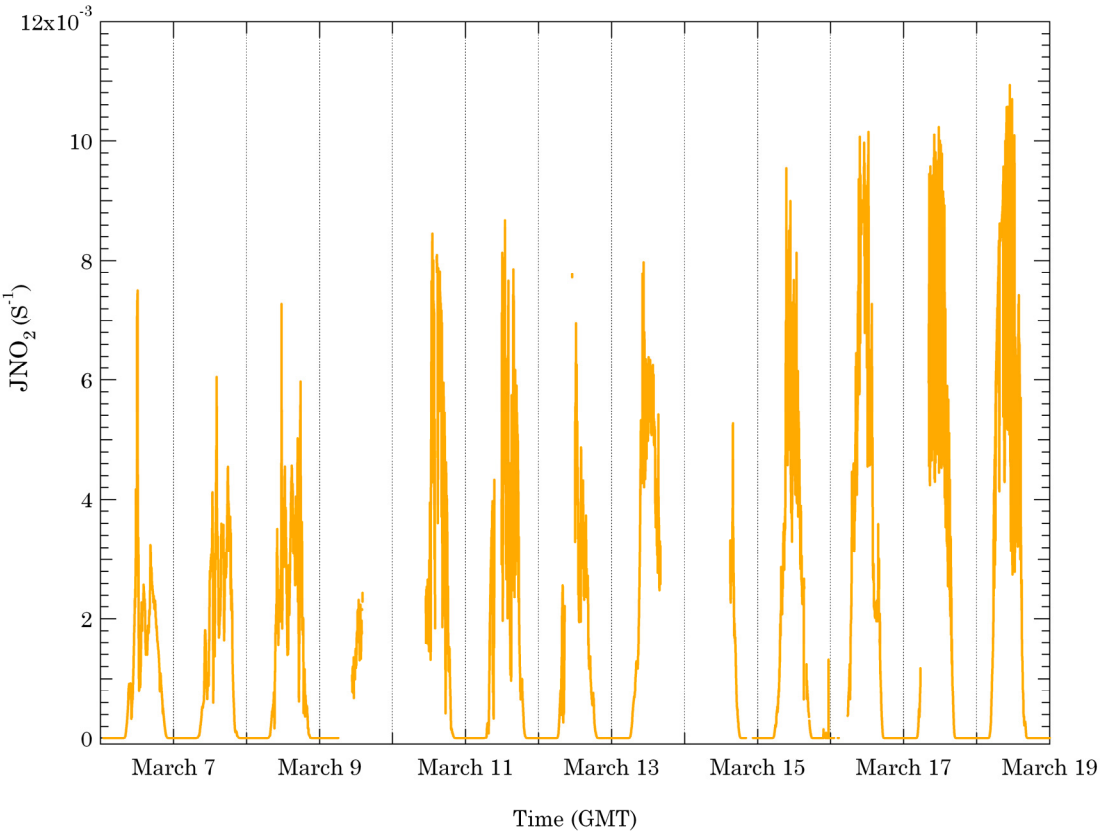

Figure 3.5 JNO_2 values measured during the MD160 cruise. Measurements started on March 6th and continued until the end of the campaign. Missing data is due to downtime of the instrument.

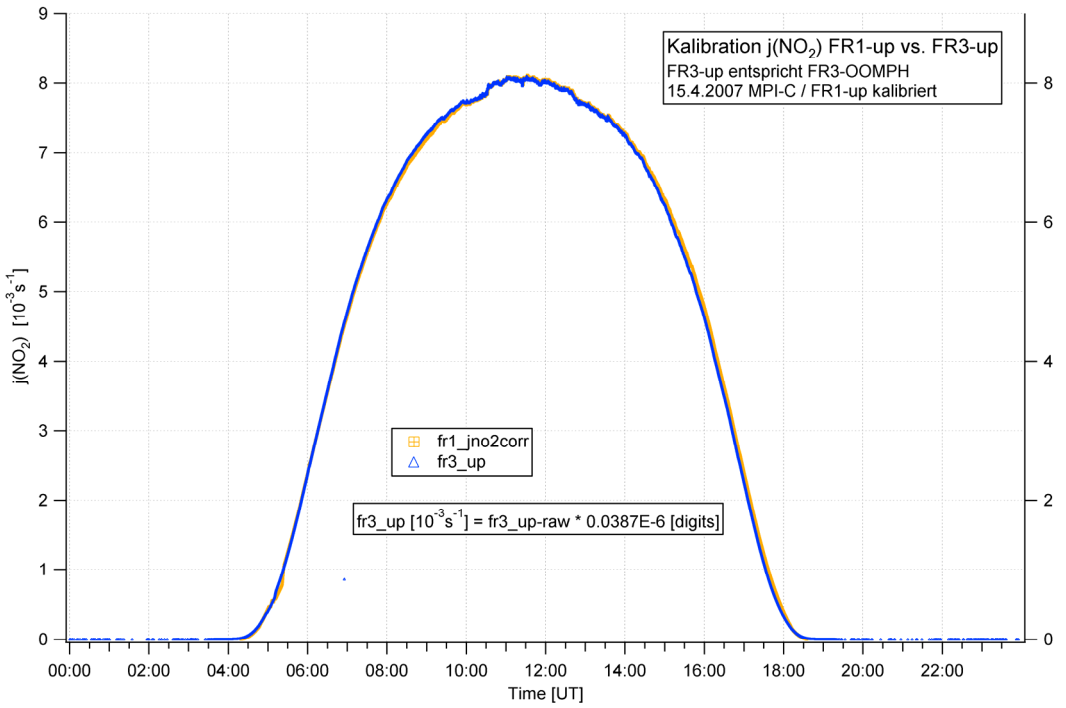

Figure 3.6 JNO_2 profile on a sunny day is bell shaped. The above calibration of the instrument was carried out by the optical spectroscopy group, MPI in Mainz.

An almost complete bell-shaped profile of the JNO_2 data can be seen in figure 3.6, which is actually a calibration measurement done at the MPI in Mainz after the MD160 campaign. As can be observed from the trend in JNO_2 data in figure 3.5, the maximum JNO_2 values increase as the ship moves from the South American continent towards the South African continent. Generally, in the beginning of the campaign, cloud cover was extensive. However, during the second part of the campaign clear sky conditions were often encountered. During the campaign, the O_3 photolysis frequency $JO(^1D)$ was also measured and was compared to the JNO_2 values which showed excellent agreement (not shown here). As expected, maximum JNO_2 and $JO(^1D)$ values were observed at noon on each day. Based on the calibration data plotted in figure 3.6, a correction factor was applied to the raw JNO_2 data.

The air and sea temperature were measured during the MD 160 by at least two different groups. Comparison of the two data sets showed very good agreement between the measurements. The air temperature for the specific study period in this investigation (March 13th to 19th) is plotted in figure 3.7 (data courtesy of Dr. M. Martinez).

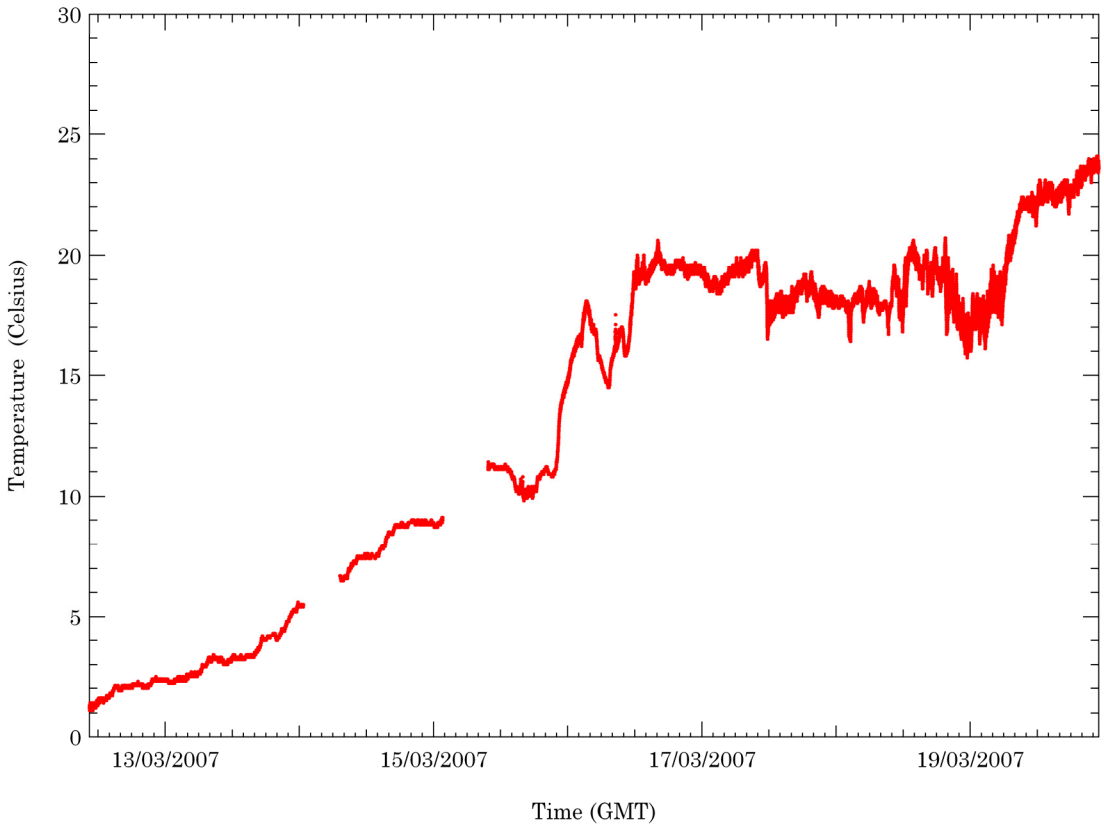

Figure 3.7 Air temperature measured during MD160, unit is in degrees Celsius.

An increase from around zero degrees Celsius (in the sub-Antarctic region) up to approximately 25 °C can be seen as the ship moves towards the African continent. Knowledge of the air temperature is crucial in calculating reaction rate constants from the Arrhenius equation for PSS studies.

3.5 Data Filtering

During a ship based campaign, the ship's own exhaust is at times a potential source of contamination for practically all kinds of atmospheric measurements. While using well positioned, inlets can support contamination-free sampling, depending on the wind direction it can also lead to a significant fraction of contaminated samples. This is especially true for campaigns where the ship has to pursue a tight schedule and the sampling points are fixed. It is extremely important in the case of PSS studies to remove all perturbed data as periods of contamination are regarded as non-PSS cases.

On the MD 160 cruise there were extended time periods with wind directions coming from behind the ship bringing exhaust from the stack, located in the middle of the ship, to the inlet, see figure 3.8. To reliably exclude the contaminated data from the dataset before further analysis, measurement data were filtered and time intervals with exhaust contamination were removed. A lot of time and effort was put into finding the optimum filtering process. The filtering was done based on a variety of techniques and criteria including wind data and NO measurements, which are explained in detail in this section. For data that were used in PSS calculations, additional JNO_2 filtering and a filter based on the uncertainty of the channels were implemented.

3.5.1 Removing exhaust contamination via wind filter

The criteria for data exclusion were observations of wind direction relative to the front of the ship, for which the CLD data showed signs of exhaust contamination.

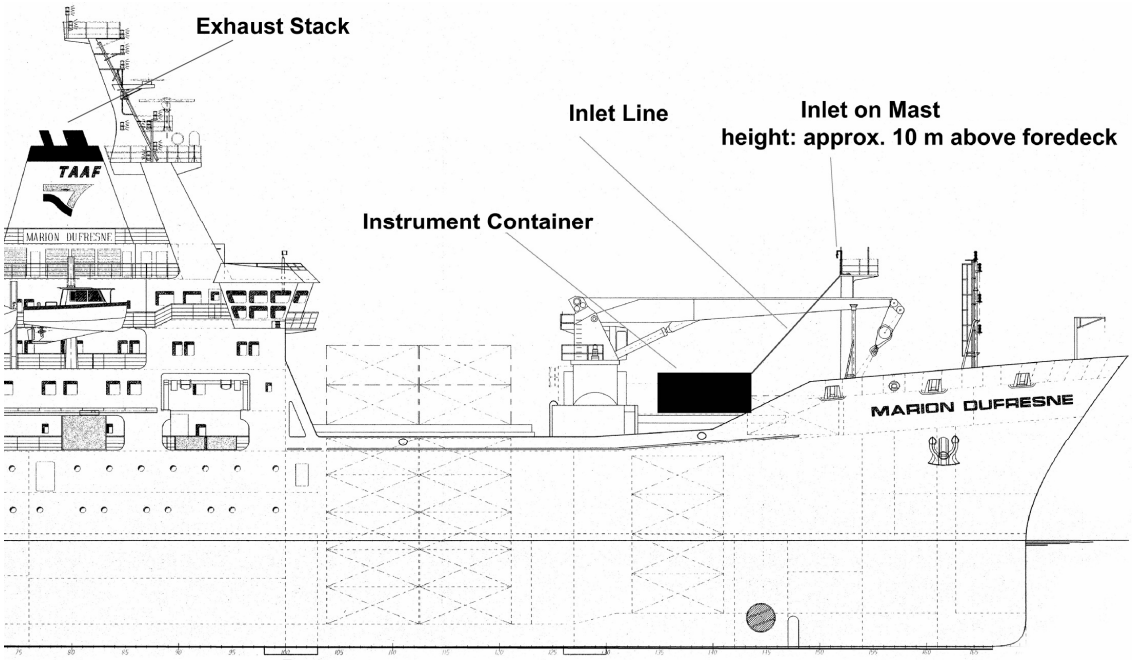

Figure 3.8 The Marion Dufresne. Indicated on this plot is the exhaust stack relative to the atmospheric mast and the instrument container. Wind coming from behind the ship towards the atmospheric mast resulted in data contamination (plot adapted from (Zorn et al., 2008)).

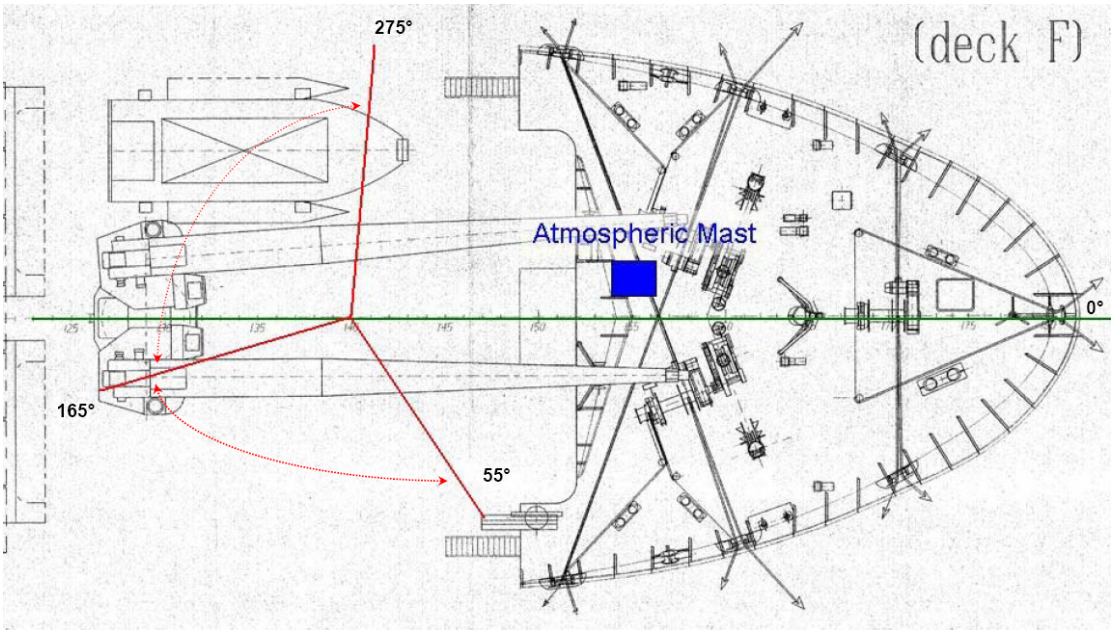

Figure 3.9 The wind filter automatically eliminated data when the wind direction was unsuitable, that is when the wind came from the back of the ship (between 55° and 275°). The blue box represents the atmospheric mast on top of which the sampling line was placed.

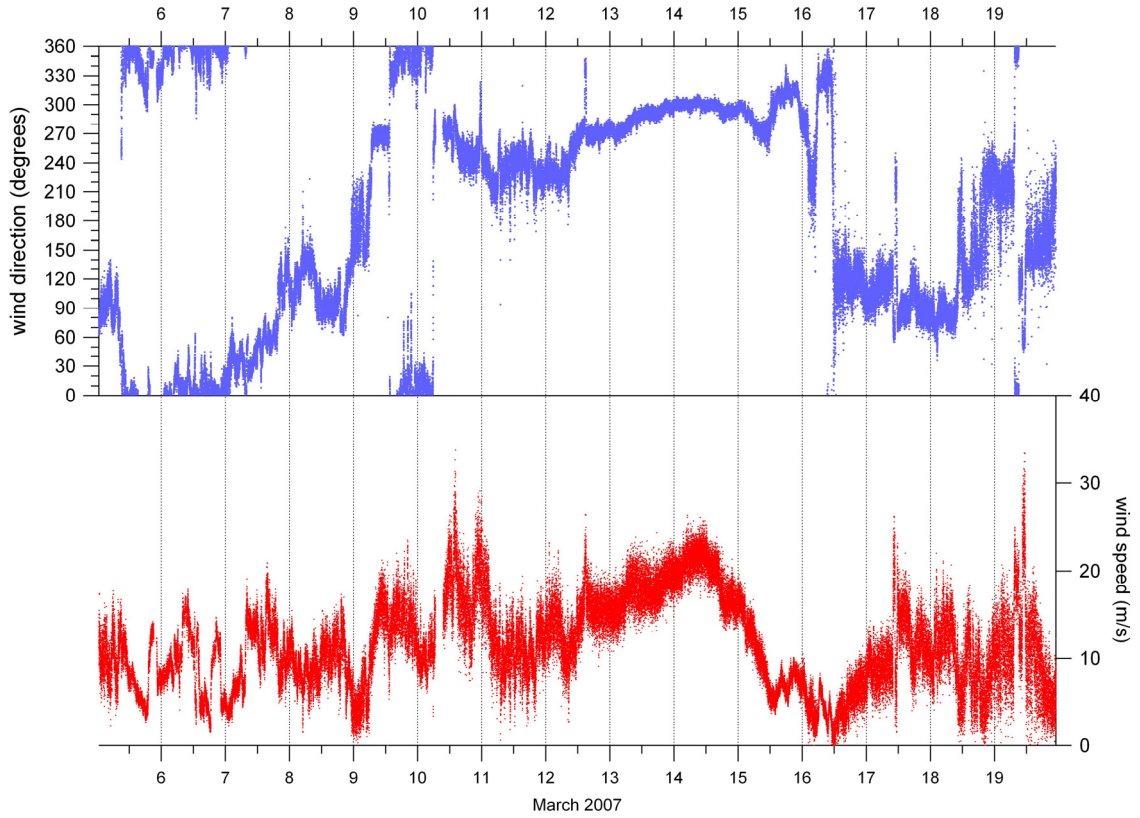

Figure 3.10 Wind speed and wind direction data during the MD160 cruise. Data shown here are from March 5th to 20th.

Exhaust contamination was generally observed when the wind came from a sector between 55° and 275° relative to the ship (0° is in the front, 180° in the back), see figure 3.9. NO is a trace gas that is directly affected by the stack exhaust. As the CLD carries out very fast measurements of NO i.e. every 2 seconds, therefore the process of filtering was relatively direct and straightforward. Once stack exhaust contamination started, it was immediately observed in the NO mixing ratios. The optimum angles used for filtering mentioned above were obtained through a trial and error process.

A filter procedure was written for the software program, IGOR Pro (Wave Metrics, INC), which was also used for data analysis. Data was automatically removed by the procedure when the wind originated from the 'contaminated' sector. After the automatic removal of the contaminated data a significant amount of time was spent in order to check the result manually. Obviously a considerable amount of data was lost during the filtering process but this was necessary in order to ensure data quality for subsequent analysis. The wind filtering of the data alone resulted in the removal of 53% of the data.

3.5.2 Contamination removal via a direct NO filter

While the use of wind direction (figure 3.10) is a good means of filtering contaminated data through observations, it is not sufficient and is considered an indirect filtering method. It is believed that an additional direct NO filter is more effective in removing contamination and should be used as a complimentary step for the removal of contaminated data via the wind direction method. For this purpose, 2 second NO data was used in order to identify and remove periods of stack contamination from the original data set. A good example of the direct effect of stack contamination on measurements was seen during two separate half hour periods when the ship turned away from the original ship track (March 12th and 17th). This test was carried out in order to see the effect of wind direction directly on the measurements. It was observed that once the direction changed from the contaminated sector (55° to 275° sector) to outside this sector, within seconds NO data went down to background values expected in the remote MBL. On return to the original ship route, the immediate effect of stack exhaust could be seen as sharp spikes in the NO data (figure 3.11). The green box indicates the period during which the ship turned away from its original route.

Many methods were well thought-out, reviewed and tested on how to optimize the use of NO data as a direct filter. The NO filter which was consequently used was a constant number which was obtained through several steps of calculation for each day of the campaign individually. In a first step, the average ± 3 standard deviation was calculated for 10 minute intervals from the original data set. In a second step, the average of the standard deviation obtained in the last step was taken over the course of one day. This calculation results in a constant number, which was used as a filter for the NO data. Any data points outside the uncertainty range are discarded automatically using a filtering procedure in the IGOR Pro software.

This approach is based on the principle that in the background conditions of the MBL there are hardly any changes to the concentrations of NO measured over a specific period of time and are therefore considered more or less constant. This was observed

during background period measurements unless pollution events occurred, e.g. stack exhaust was released into the atmosphere. As a result of this perturbation, sharp spikes and frequent rise and fall in NO concentrations was seen, which could also naturally be observed in the standard deviation.

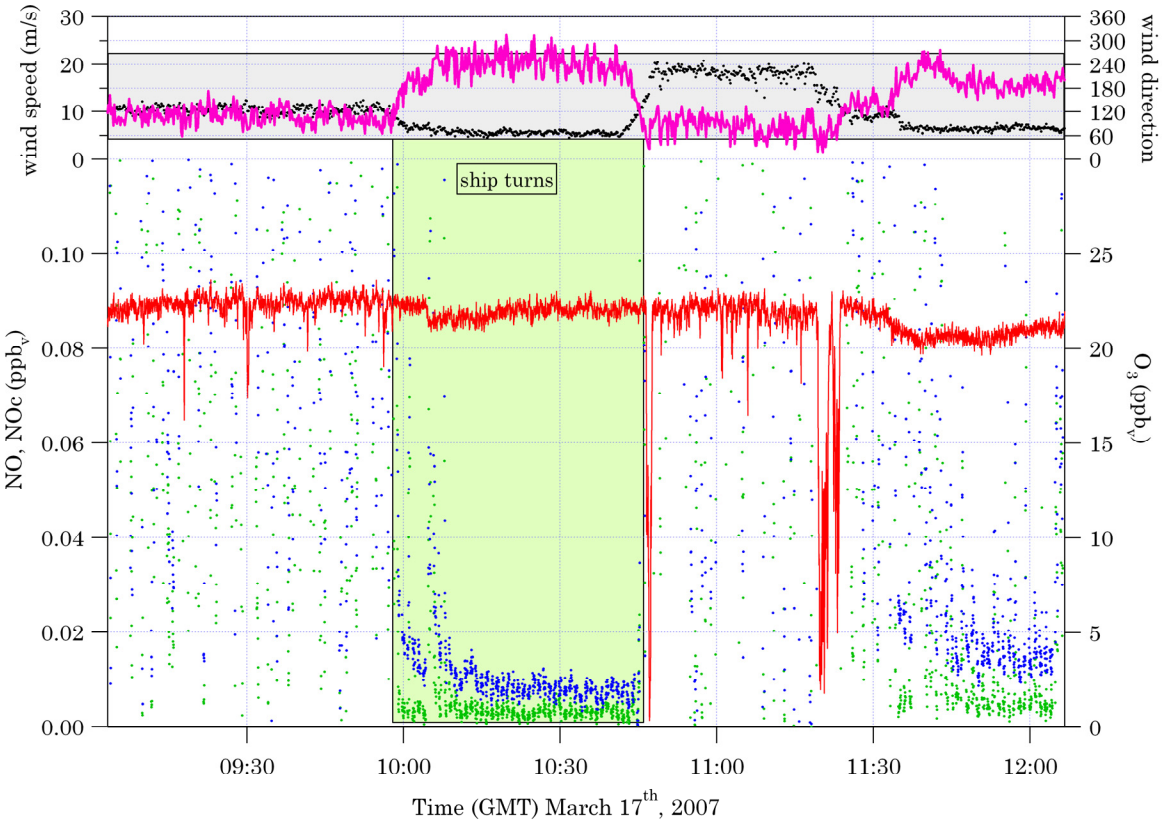

Figure 3.11 The affect of wind direction on measurement contamination on March 17th. Mixing ratios of the measured O_3 (red lines), NO (green dots), NOc (blue dots) and the wind speed (pink line) and wind direction (black dots) are plotted.

Therefore, the standard deviation is an excellent parameter and can give one an idea about the deviation from the normal background values directly as the perturbations take place.

3.5.3 Additional filtering for subsequent PSS calculations

In order to carry out precise and accurate PSS calculations for the data set in hand, two other additional filters were used. Due to the measurements being carried out in the remote MBL, the NO and NO_2 concentrations were very small and close to the detection limit of the instrument. As mentioned previously, NOx concentrations measured during the campaign are among the lowest measured concentrations ever reported. The CLD instrument used to measure NOx concentrations is a high resolution high sensitivity detector, with an excellent limit of detection. In general it is known that significant uncertainty can arise once measurements are made that are close or below the detection limit of an instrument. Therefore in order to ensure data quality, a third filter was set up using the total uncertainty based on the calculations of

precision and accuracy of the NO and NO_2 channels. Any data point which was below the total uncertainty of the relevant channel was excluded automatically. The 2σ uncertainty for the NO channel and NO_2 channel in this investigation are 1.5 ppt_v and 2.2 ppt_v respectively. There were concerns that this filter may affect the overall result of the analysis. Therefore PSS calculations were carried out using both an uncertainty filter and without. The result from the two sets of calculations did not show any significant changes to the overall outcome of the calculations.

It is well known that PSS calculations can be largely influenced by uncertainties in JNO_2. In this study, real time simultaneous measurements of the photolysis rate of JNO_2 were carried out in order to reduce uncertainties due to this parameter. However, at small JNO_2 values, e.g. sunrise and sunset, deviations are expected from unity, therefore steady state assumptions are not valid. Since sufficient solar radiation is essential for the NOx system to achieve PSS, only data for JNO_2 values >0.001 s^{-1} are used in this study. Any value below this range is automatically excluded from the data set.

Chapter 4: Investigation of NOx and O_3 photostationary state

Many aspects of photochemical processes taking place in the atmosphere are not well understood. The main objective of this study is to better understand the photochemistry of NOx and O_3 in the MBL, with special focus on ozone photochemistry in a pristine MBL with very low concentrations of NOx. The remote MBL is well suited to study the unperturbed chemical processes that drive NOx and O_3 photochemistry.

Measurements were carried out on board a research vessel, Marion Dufresne, crossing the southern Atlantic (28°S-57°S, 46°W-34°E) during the OOMPH campaign in March 2007. The southern Atlantic Ocean is much less anthropogenically affected than the northern Ocean and there are hardly any contributions from man-made sources. Measurements of NO, NO_2, O_3, HO_2, OH, ROx and JNO_2 and meteorological parameters were performed and therefore data was obtained over a vast spatial area. Back trajectories were also calculated to look into influences on the air masses encountered during the ship cruise. The concentrations of NOx measured during the campaign are among the lowest yet reported. The data obtained in the pristine Antarctic region is evaluated for consistency with photochemical steady state conditions (PSS).

Currently the size of the database needed to define non-urban NOx is limited. This is because only during recent years have techniques been available with sufficient sensitivity and range detectability to measure NOx in non-urban areas (ppt_v range). In the past, various studies have estimated or theoretically calculated NO_2 and ROx mixing ratios from other measured parameters such as NO, O_3 and HO_2. In this study, all parameters which are believed to be required to comprehensively investigate the PSS of NOx and O_3 in the remote MBL have been measured for the first time. This makes this study unique in the sense that measurements are done in a pristine MBL, without the effect of any anthropogenic pollution whatsoever. The use of high resolution instruments with very low detection limits has allowed us to obtain a data set which is apt for studying the PSS in the remote MBL. The VOCs and NOx levels reported during the MD 160 cruise are among the lowest to date. It is believed that this investigation will lead to a better understanding of the NO-NO_2-O_3 system in remote regions and advance our knowledge of photochemistry in the non-continental southern hemisphere.

4.1 Theory

As explained in detail in Chapter one, the Leighton ratio (φ) is a way of characterizing PSS:

$$\varphi = \frac{JNO_2[NO_2]}{k_3[O_3][NO]} \qquad \text{(Equation 4.1)}$$

The above equation has been widely used in previous investigations of PSS in continental and urban regions. In an air mass where NOx levels are low enough for peroxy radicals to be significant in NO oxidation, the PSS of NOx is expressed as:

$$\varphi = \frac{JNO_2[NO_2]}{(k_3[O_3]+k_4[HO_2]+k_5[RO_2])[NO]} \qquad \text{(Equation 4.2)}$$

However, even with the inclusion of HO_2 and RO_2 contributions in the Leighton ratio a systematic disagreement among actual observations, models and theoretically calculated concentrations of trace gases from the above ratio has been reported.

4.2 Results and discussion

4.2.1 Clean MBL data

The aim of this study is to investigate the PSS of NOx and O_3 in clean background conditions of the southern Atlantic Ocean. Therefore, only daytime data where background air masses were measured have been used in this study. All other data is either contaminated by stack smoke or is clean data, but due to being below the detection limit (DL), is automatically removed from the data set. This filtering process has already been explained in detail in Chapter three. All data used in the study are averaged over 1 minute. Analysis and comparison are only done for periods were all parameters required in order to calculate the PSS equations are available. Both GMT and local time, for periods used in this study are presented in table 4.1. The start and end coordinates of each period, i.e. longitude and latitude, are also mentioned for geographical orientation.

Table 4.1 Periods of clean background measurements used in this study

Day	Time(GMT)	Local time	Longitude	Latitude
13.03.2007	09:23 - 14:23	9:00 – 14:06	-5.8 to -4.2	-51.8 to -51.0
14.03.2007	14:56 - 16:45	15:08 – 17:00	3.2 to 3.7	- 46.9 to -46.6
15.03.2007	07:15 - 13:50	7:46 – 14:30	7.9 to 9.9	-44.0 to -42.9
16.03.2007	06:30 – 11:10	7:30 – 12:15	15.0 to 16.5	-40.5 to -39.8
17.03.2007	10:08 - 10:42	11:37 – 12:12	22.5 to 22.7	-36.9 to -37.0

Figures 4.1 to 4.10 illustrate the periods of clean background measurements carried out during MD 160 and the corresponding back trajectories for the study periods which have been used specifically in the PSS calculations in this chapter. The colour code below each plot is an indication of the pressure level, with a minimum pressure of 300 hPa in dark green corresponding to the free troposphere and a maximum of 1025 hPa in dark orange corresponding to sea surface pressure. Note that air masses with a pressure of more than 900 hPa are from within the marine boundary layer. In general for the period of study, the ten-day back trajectories show that air masses originate from Antarctica and the southern Atlantic Ocean. The majority of the time

the air mostly comes from the free troposphere, subsiding to the boundary layer some time before measurement.

The back trajectories show that air masses encountered on March 13th originate from Antarctica. They do not pass over the South American continent and the air masses which are measured subsequently are pristine background air from within the marine boundary layer.

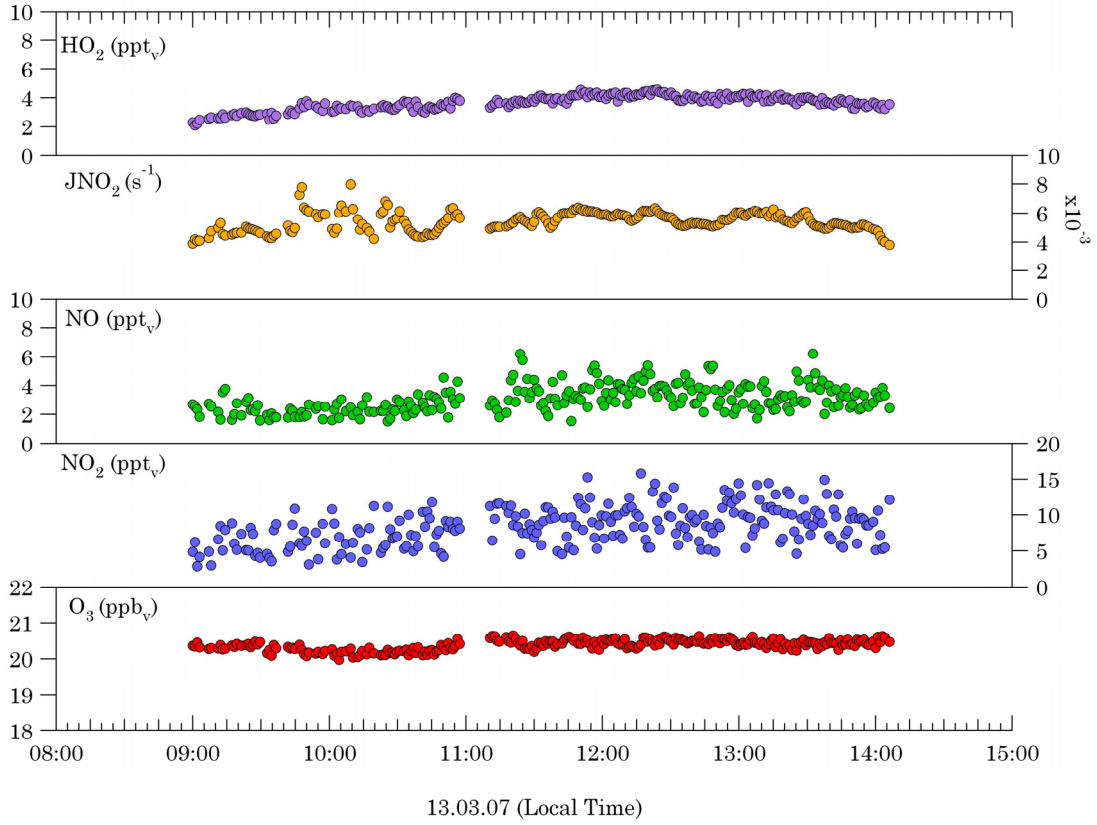

Figure 4.1 Mixing ratios of the measured O_3 (red circles), NO_2 (blue circles), NO (green circles), JNO_2 (yellow circles) and HO_2 (purple circles) in clean background MBL are plotted for the study period on March 13th 2007.

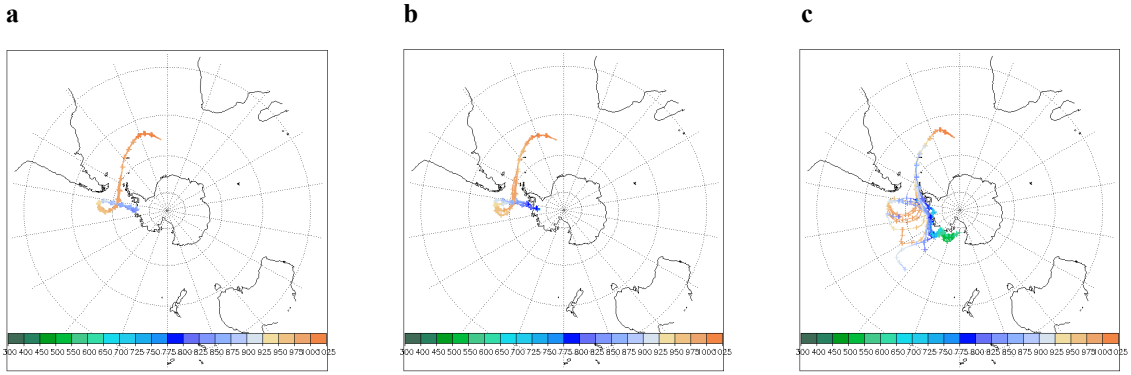

Figure 4.2 Calculated back trajectories for March 13th for the period of study. Plots a, b and c correspond to 9:00, 12:00 and 15:00 GMT respectively. The colour bar below each plot is an indication of the pressure level (300 to 1025hPa).

The concentrations of trace gases measured during the study period are relatively stable and do not change significantly over the study period. Ozone, NO, NO_2 and HO_2 mixing ratios are on average 20.4 ppb_v, 3.1 ppt_v, 8.4 ppt_v and 3.7 ppt_v respectively. The average temperature during the study period on March 13 was 3 °C.

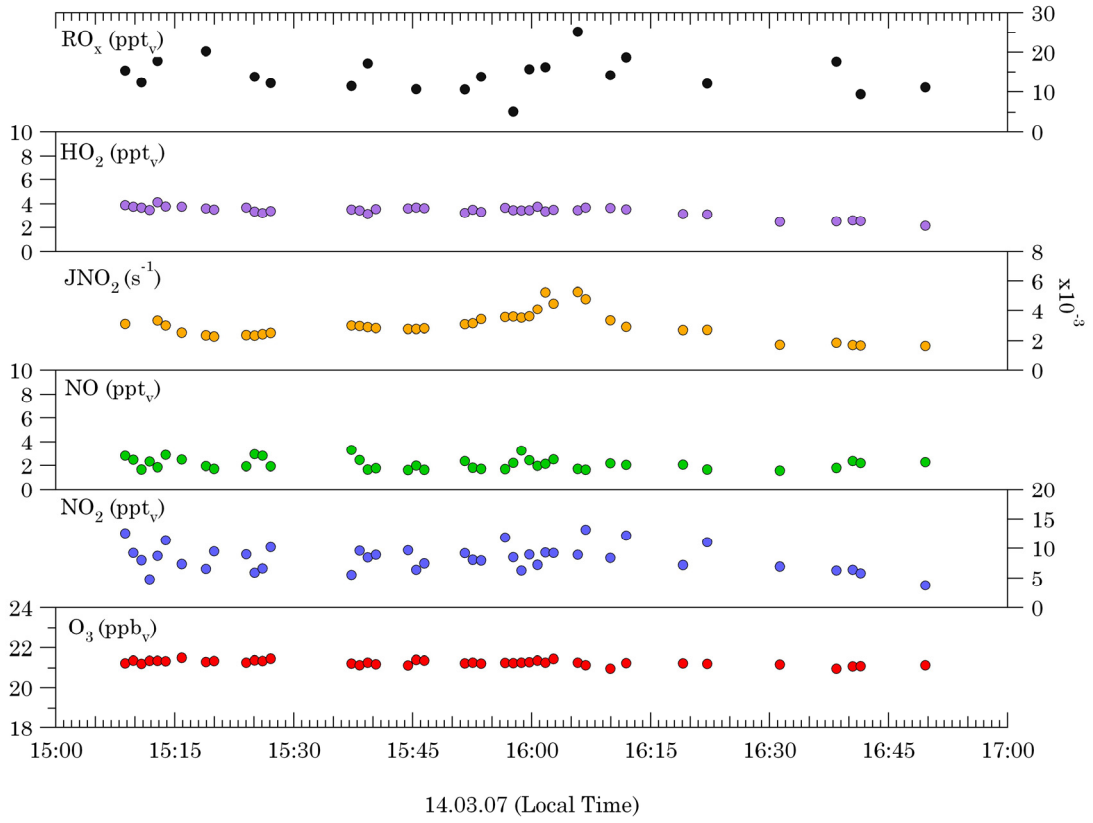

Figure 4.3 Mixing ratios of the measured O_3 (red circles), NO_2 (blue circles), NO (green circles), JNO_2 (yellow circles), HO_2 (purple circles) and ROx (black circles) in clean background MBL are plotted for the study period on March 14th 2007.

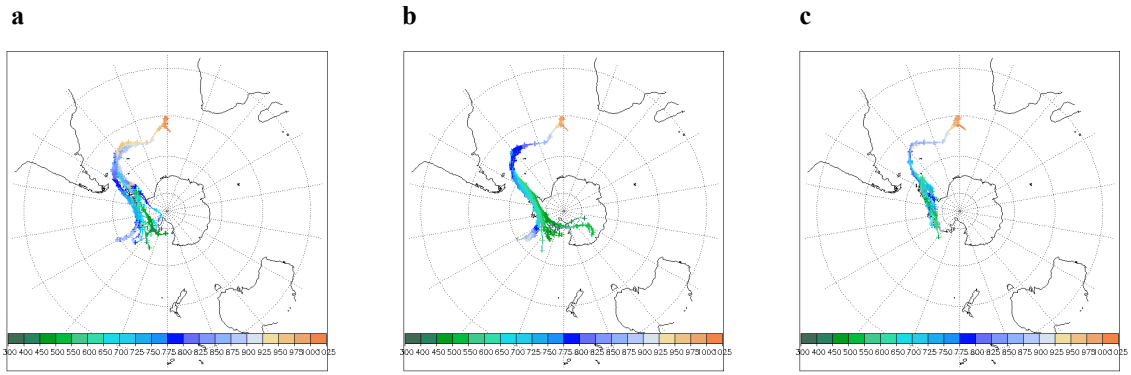

Figure 4.4 Calculated back trajectories for March 14th for the period of study. Plots a, b and c correspond to 12:00, 15:00 and 18:00 GMT respectively. The colour bar below each plot is an indication of the pressure level (300 to 1025hPa).

The average temperature during the study period on March 14th was 8 °C. Again the 10-day back trajectories indicate that the air masses encountered on March 14th originate from the continent of Antarctica, subsiding to the marine boundary layer

sometime before subsequent measurement. This period of study is relatively short with very little change in the background values of the trace gases. O_3, NO and NO_2 mixing ratios are on average 21.3 ppb_v, 2.1 ppt_v and 8.4 ppt_v respectively, while the radicals HO_2 and ROx have average mixing ratios of 3.4 ppt_v and 14.3 ppt_v, respectively.

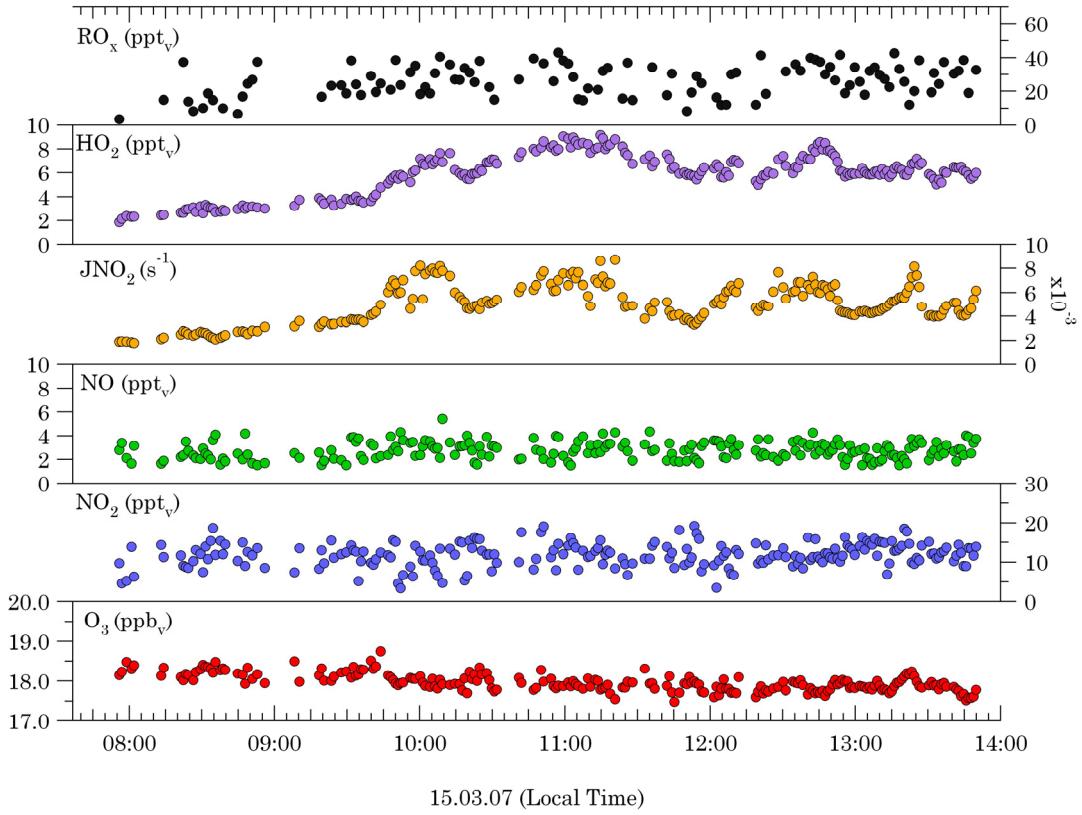

Figure 4.5 Mixing ratios of the measured O_3 (red circles), NO_2 (blue circles), NO (green circles), JNO_2 (yellow circles), HO_2 (purple circles) and ROx (black circles) in clean background MBL are plotted for the study period on March 15th 2007.

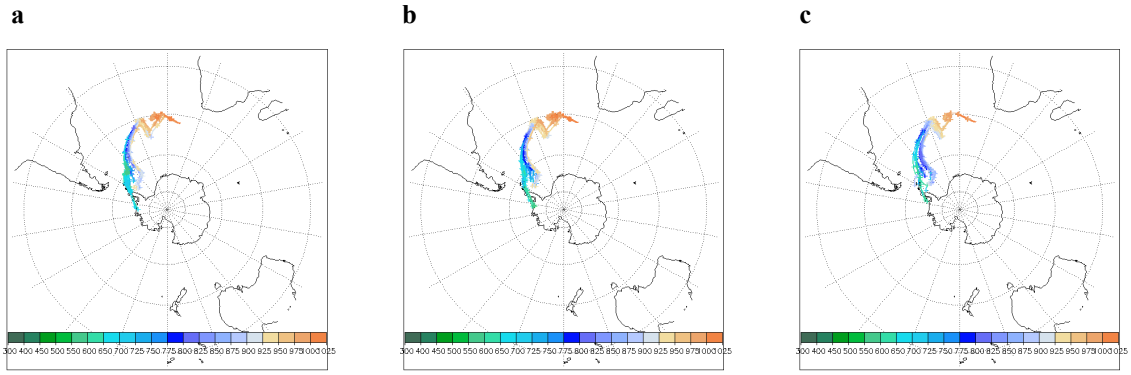

Figure 4.6 Calculated back trajectories for March 15th for the period of study. Plots a, b and c correspond to 9:00, 12:00 and 15:00 GMT respectively. The colour bar below each plot is an indication of the pressure level (300 to 1025hPa).

The 10-day back trajectories indicate that the air masses encountered on March 15th originate from the shores of Antarctica, subsiding from the free troposphere to the

marine boundary layer sometime before measurement. The average temperature during the study period on this day was 11 °C. Again on this day, there is very little change in the mixing ratios of O_3, NO and NO_2, which are on average 18 ppb_v, 2.8 ppt_v and 11.8 ppt_v respectively. However there is a general increase in the HO_2 and RO_2 mixing ratios with time, which correlates well with the increase in JNO_2 values and thus the level of photochemical activity.

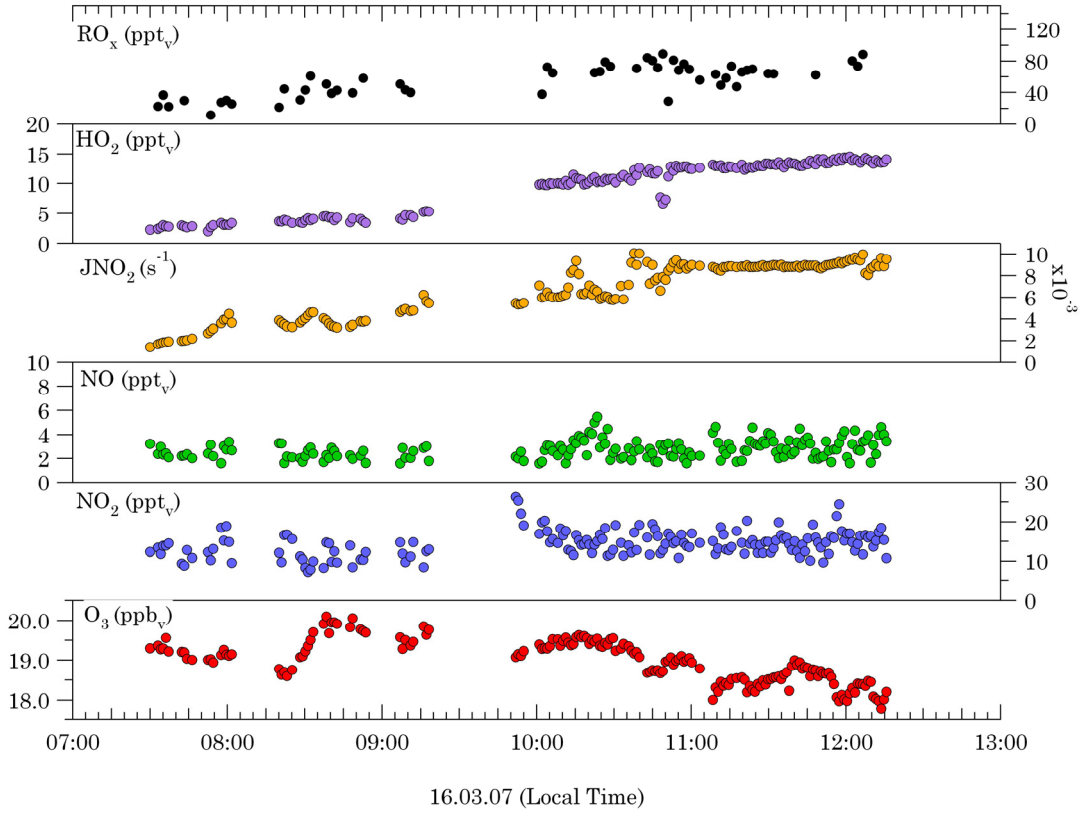

Figure 4.7 Mixing ratios of the measured O_3 (red circles), NO_2 (blue circles), NO (green circles), JNO_2 (yellow circles), HO_2 (purple circles) and ROx (black circles) in clean background MBL are plotted for the study period on March 16th 2007.

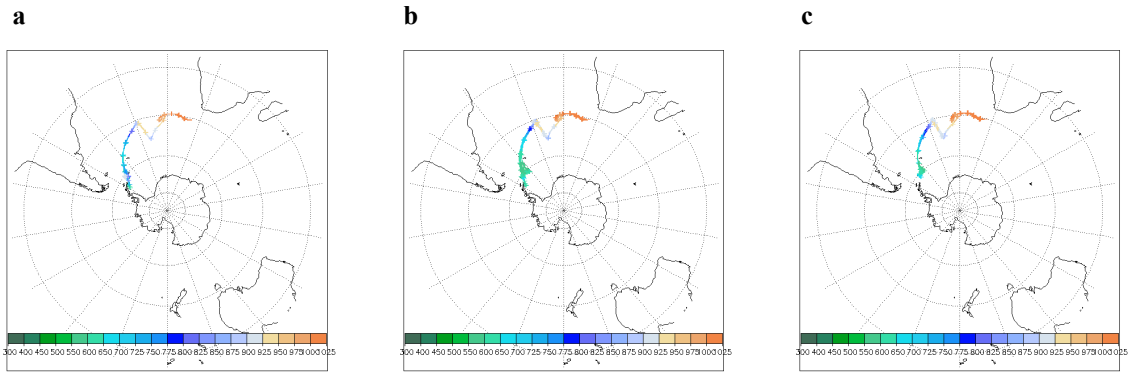

Figure 4.8 Calculated back trajectories for March 16th for the period of study. Plots a, b and c correspond to 6:00, 9:00 and 12:00 GMT respectively. The colour bar below each plot is an indication of the pressure level (300 to 1025hPa).

On March 16th, the ship is two days away from the coast of South Africa. The back trajectories, however, confirm that the air masses are from the South Atlantic Ocean and are not influenced by the African continent. The average temperature during this study period is on average 16 °C, with temperatures increasing as we go towards South Africa. Mixing ratios of O_3, NO and NO_2 are on average 19 ppb_v, 2.8 ppt_v and 14.4 ppt_v respectively.

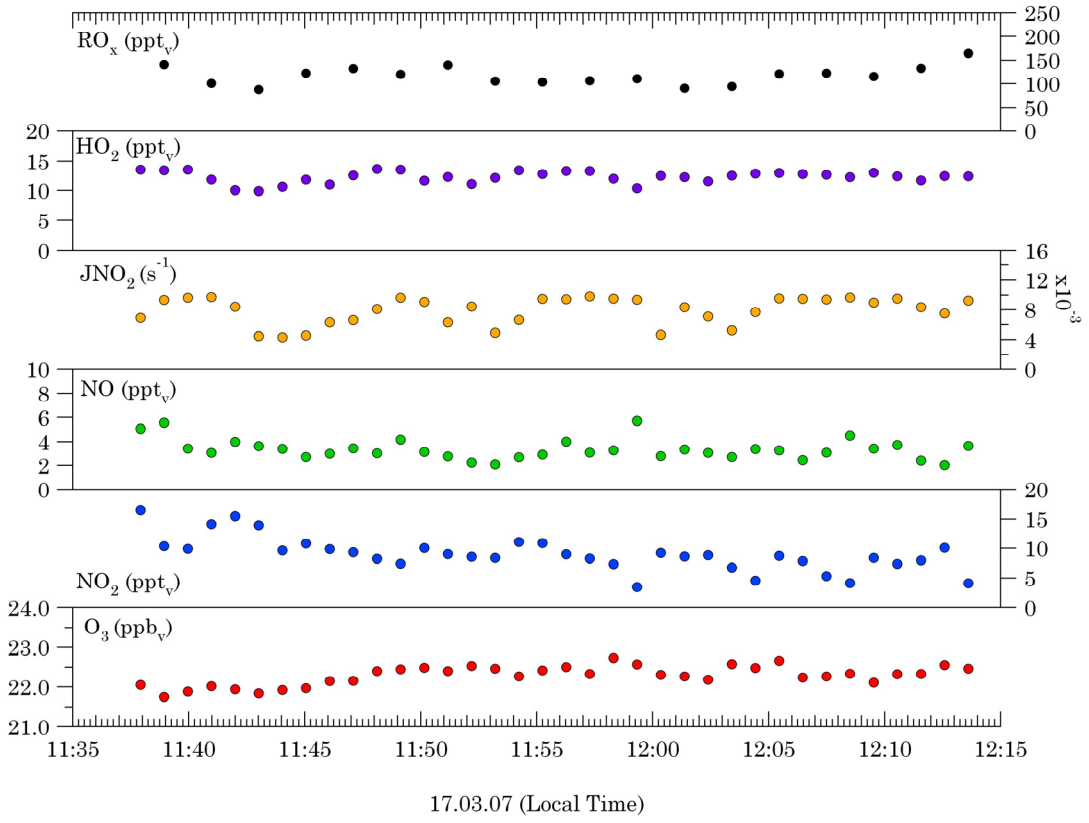

Figure 4.9 Mixing ratios of the measured O_3 (red circles), NO_2 (blue circles), NO (green circles), JNO_2 (yellow circles), HO_2 (purple circles) and ROx (black circles) in clean background MBL are plotted for the study period on March 17th 2007.

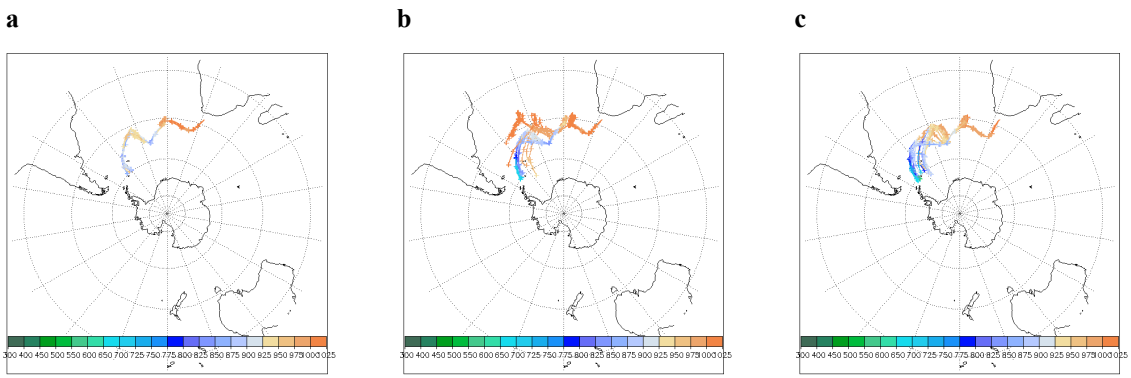

Figure 4.10 Calculated back trajectories for March 17th for the period of study. Plots a, b and c correspond to 6:00, 9:00 and 12:00 GMT respectively. The colour bar below each plot is an indication of the pressure level (300 to 1025hPa).

The last period of clean air that is used in this study, March 17th, is the result of the ship turning away from its original course, so that for the period shown in figure 4.9, the wind direction was directly from the front of the ship and therefore clean air masses could be measured for a short period of time. The average temperature on this day was 19 °C. The air masses originate from the southern Atlantic and had already subsided in the MBL for some time before being measured.

Apart from the data presented in table 4.1, data from two other periods were used which are not regarded as background conditions of the remote MBL (table 4.2).

Table 4.2 Data obtained from the measurement of non-pristine air masses used for comparison with background conditions

Day	Time(GMT)	Local time	Longitude	Latitude
15.03.2007	14:45 - 15:30	15:25 – 16:11	10.23	-42.8
19.03.2007	8:03 – 9:04	10:07 – 11:08	31.1	-29.9
19.03.2007	10:30 – 11:30	12:36 – 13:36	31.5	-29.8

On March 15th, during the period of time between 15:25 to 16:11 local time, very high mixing ratios of NOx were detected by the CLD instrument. The values went up from the background NOx mixing ratios of 18 ppt_v to a maximum of 1.5 ppb_v, and then decreased again to background concentrations, all in the time period of 45 minutes.

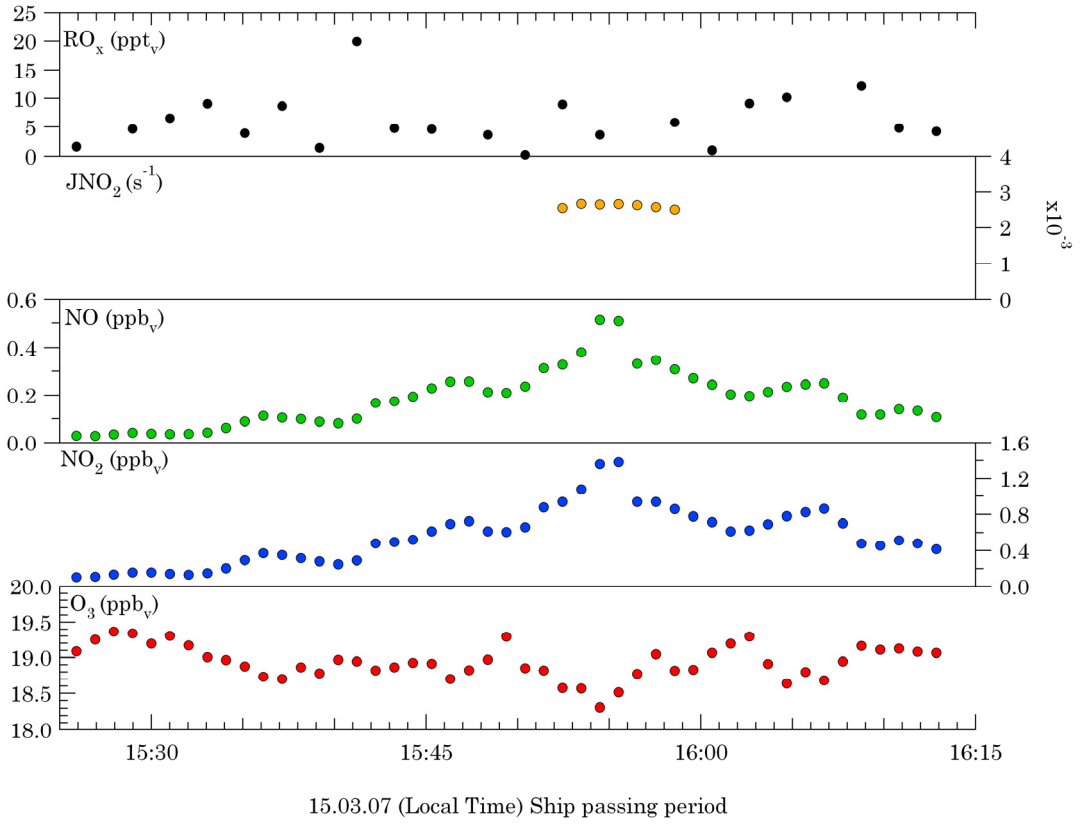

Figure 4.11 Mixing ratios of the measured O_3 (red circles), NO_2 (blue circles), NO (green circles), JNO_2 (yellow circles) and ROx (black circles) are plotted for the high NOx episode due to the passing of a second on March 15th 2007.

The high concentrations of NOx were due to the passing of a second ship, which was on collision course with the Marion Dufresne. O_3, NO and NO_2 were all measured during this period, however, due to technical problems, no HO_2 data is available for the period of this event. JNO_2 values are missing during the major part of the event. However, JNO_2 values are available when NOx levels are at their maximum concentrations of approximately 1.5 ppb_v. The two ships had several kilometres of distance between them and therefore it is believed that the air mass had time to process and for PSS to be established. This period is of course excellent in regard to studying the effect of the release of anthropogenic pollution into the pristine MBL and comparison with clean background conditions.

The second is from a period of time on the 19th of March where continental air was measured. Due to a change in wind direction, this period was not polluted by ship stack. This air mass is believed to be representative of air in Durban, South Africa (see figure 4.12).

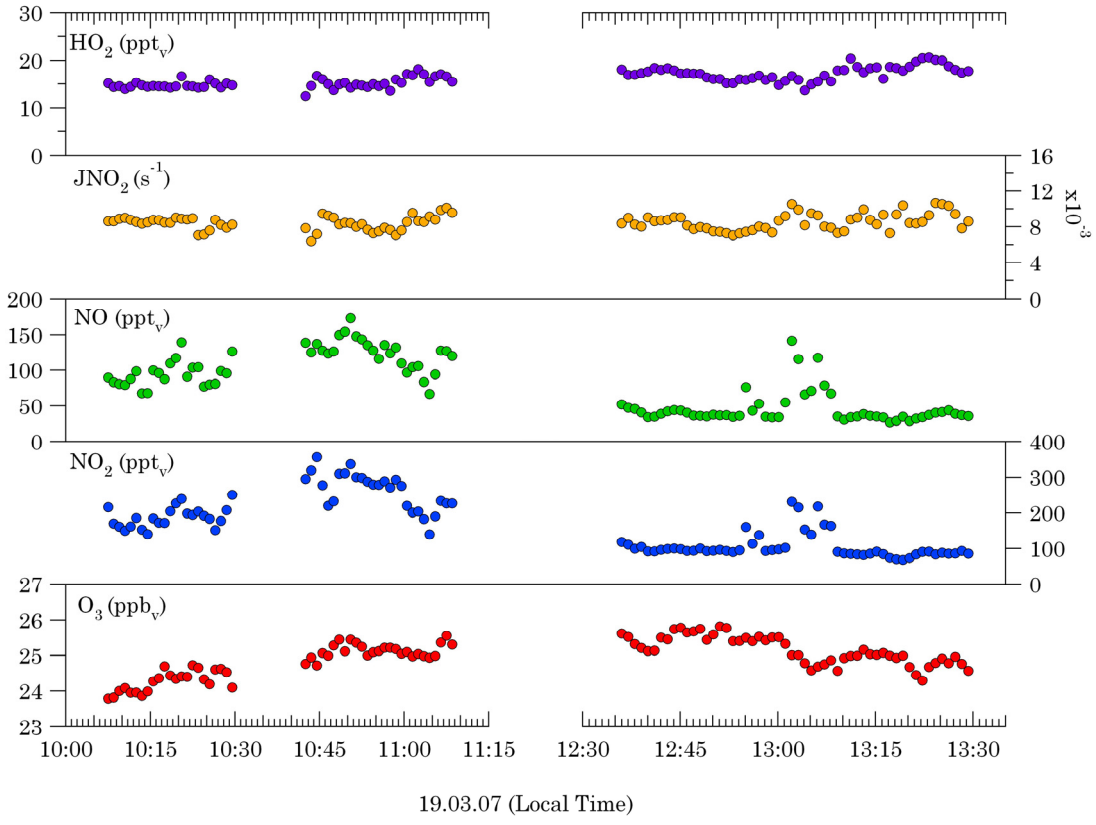

Fig 4.12 Mixing ratios of the measured O_3 (red circles), NO_2 (blue circles), NO (green circles), JNO_2 (yellow circles) and HO_2 (purple circles) are plotted for the African continental air masses measured off the coast of Durban on March 19th 2007.

In this study, based on the measurement principle, ROx is defined as the total sum of OH, RO, HO_2 and RO_2. The contributions of OH and RO to total ROx are sufficiently low that they can effectively be neglected from the following equation:

$$ROx = OH + RO + HO_2 + RO_2 \qquad \text{(Equation 4.3)}$$

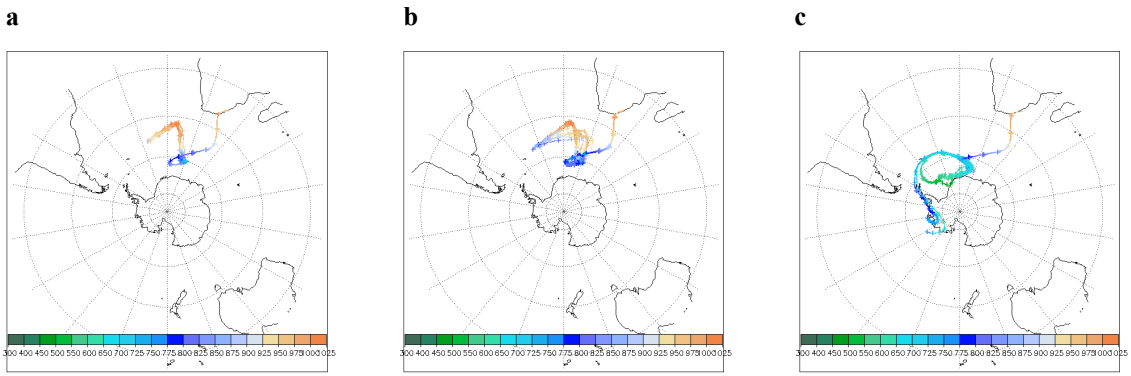

Figure 4.13 Calculated back trajectories for March 19th for the period of study. Plots a, b and c correspond to 6:00, 9:00 and 12:00 GMT respectively. The colour bar below each plot is an indication of the pressure level (300 to 1025hPa).

Since HO_2 was measured during the MD 160 cruise using a LIF instrument, RO_2 can in theory be derived from the total ROx (PERCA) signal. In regard to RO_2, it is generally known that the identity and concentration of each of the various organic peroxy radicals present in the air sample can not be determined. Such detailed measurements are not possible with the currently available techniques. Therefore, a set of assumptions based upon the chemical behaviours and composition of the peroxy radicals are generally made when carrying out PSS calculations.

Measurements by Mihelcic et al. have shown that during the daytime the RO_2/ HO_2 ratio is relatively constant and demonstrates values between approximately 0.75 and 1.0 regardless of the NOx levels in the atmosphere (Mihelcic et al., 2003). Therefore, from these observations it was assumed that HO_2 and RO_2 are present in nearly equal amounts in the atmosphere during daylight hours, $[RO_2] \approx [HO_2]$. Mihelcic also calculated the RO_2/HO_2 ratio using the Master Chemical Mechanism model (MCM). The model predicts the ratio of approximately unity, independent of the NO mixing ratio which varied between 0.05 and 10 ppb. The assumption that HO_2 and RO_2 concentrations are almost equal during the day has also been tested through comparison of measured and modeled data by Cantrell et al. (Cantrell et al., 2003).

The peroxy radicals were measured over the Pacific Ocean with NOx mixing ratios varying from 10 ppt_v to 10 ppb_v. In this case, it was inferred from the $HO_2/(HO_2+RO_2)$ ratio that HO_2 concentrations varied between half to twice as much HO_2 compared to RO_2. In the remote MBL, it is believed that the majority of the organic peroxy radical is in the form of methyl peroxy radical (CH_3O_2) (Dr. M. Martinez, personal communication). Therefore it is assumed that $[RO_2] \approx [CH_3O_2]$. This is due to the fact that CH_3O_2 is a product of the CH_4 oxidation chain, while all other hydrocarbon species have very low concentrations in the MBL. Therefore in this study, the reaction rates of CH_3O_2 were used for calculations involving RO_2.

4.2.2 A comparison between measured and calculated NO/NO_2 ratio

The NO/NO_2 ratio was calculated from 1 minute averages of observed NO and NO_2 for two days in clean background air masses, i.e. March 13th and 15th. The aim of this comparison is to investigate the effect of HO_2 and RO_2 radical concentrations on the

PSS ratio. The values are only calculated for daytime as the ratio is equal to zero during the night. Also near sunrise and sunset, measured values are less reliable since achievement of PSS is no longer expected due to slower NO_2 photolysis. The variation of the observed NO/ NO_2 ratio on March 13 is shown in figure 4.14 (red circles with error bars). Provided that the system is in PSS, the following ratios are expected to be good approximations for comparison with the observed ratio:

$$\frac{[NO]}{[NO_2]} = \frac{JNO_2}{k_3[O_3]} \qquad \text{(Equation 4.4)}$$

$$\frac{[NO]}{[NO_2]} = \frac{JNO_2}{(k_3[O_3]+k_4[HO_2])} \qquad \text{(Equation 4.5)}$$

$$\frac{[NO]}{[NO_2]} = \frac{JNO_2}{(k_3[O_3]+k_4[HO_2]+k_5[RO_2])} \qquad \text{(Equation 4.6)}$$

In the above equations, k_3, k_4 and k_5 are the reaction rate constants of NO with O_3, HO_2 and RO_2 (reactions R1.3, R1.4 and R1.5 of Chapter one). The three theoretically calculated ratios are also plotted in figure 4.14.

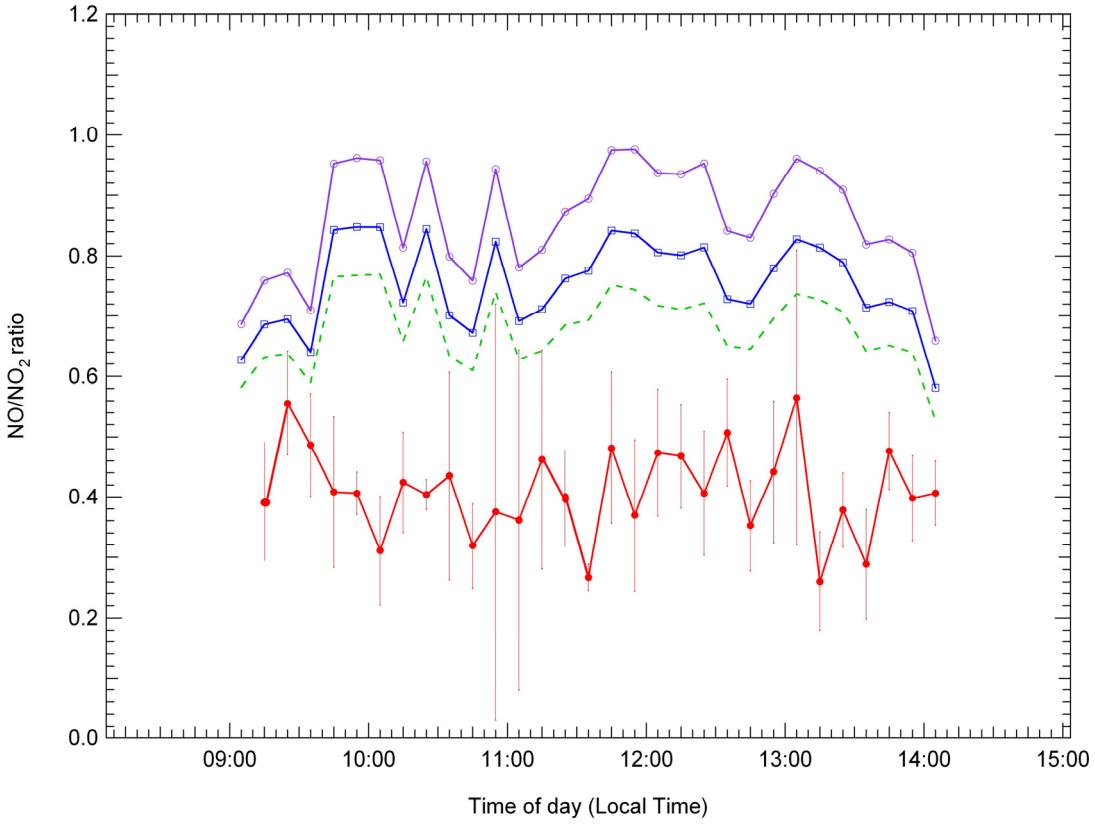

Figure 4.14 Observed NO/NO_2 ratios (solid circles with bars) compared with calculated values derived from equation 4.4 (open purple circles), equation 4.5 (open blue squares) and equation 4.6 (dashed green line) for March 13th, 2007.

Since PERCA data are only available from March 14th onwards, equation 4.6 was calculated based on the assumption that RO_2 concentrations approximately equal HO_2 concentrations. Therefore, the RO_2 concentrations in this calculation are equal to the concentration of HO_2. The uncertainties for equations 4.4, 4.5 and 4.6 derived from the uncertainty of the measurements are 14.9 %, 39.3 % and 52.9 %, respectively.

As can be observed in figure 4.14, the observed NO/ NO_2 ratio is significantly lower than those theoretically calculated. Equation 4.5, which does not include the effect of HO_2 and RO_2, has the most significant deviation from the observed ratio. With the addition of HO_2 and the theoretically assumed RO_2 to ratios B and C, respectively, the difference is accounted for to some degree. This may be an indication that there is a missing chemical mechanism for converting NO to NO_2, which is not accounted for in the PSS ratio and as a result leads to higher theoretically calculated NO/ NO_2 ratios. The average value for each ratio and also the standard deviation, maximum and minimum values are also presented in table 4.3.

Table 4.3 Average values, standard deviation, maximum and minimum values for March 13th

NO/NO_2 Ratio	Average	STDEV	Maximum	Minimum
Equation 4.4	0.86	0.09	0.98	0.66
Equation 4.5	0.75	0.07	0.85	0.58
Equation 4.6	0.68	0.06	0.53	0.77
(NO/NO_2) observed	0.41	0.08	0.57	0.26

The difference in the equation 4.4 average compared to the observed ratio is extremely high, with the value being more than double the value of the observed ratio. With the addition of HO_2 to the equation in equation 4.5, the difference slightly decreases. Nevertheless, there is still a significant difference of more than 80% between the actual observed values and equation 4.5. The effect of RO_2 on equation 4.6 is a decrease in the difference percentage. However, even with this addition the values for equation 4.6 are on average 66% higher than the average observed ratio.

The difference between the averages of the observed and theoretically calculated ratios (Δ) is calculated as:

$$\Delta = \left(\frac{\text{Ratio}_{\text{theory}} - \text{Ratio}_{\text{obs.}}}{\text{Ratio}_{\text{obs.}}} \right) * 100 \qquad \text{(Equation 4.7)}$$

In the above equation, '$\text{Ratio}_{\text{theory}}$' is the average theoretically calculated ratio (equations 4.4, 4.5 or 4.6) and '$\text{Ratio}_{\text{obs.}}$' is the averaged observed ratio.

Equations 4.4, 4.5 and 4.6 were also calculated for March 15th. For this period, a second "equation 4.6" was calculated using the observed data from the PERCA instrument (solid yellow lines). This ratio will be referred to as equation 4.6**'.**

As shown in figure 4.15, the observed NO/ NO_2 ratio, average of 0.24, is significantly lower than the theoretically calculated ratio, average of 0.75. Equation 4.4, which does not include the effect of HO_2 and RO_2, has the most significant deviation from the observed ratio. With the addition of HO_2 and assumed RO_2 to the equation the difference is accounted for to some degree (ratios 4.6 and 4.6' respectively). However, there is still a significant difference between the actual

observed values and the theoretically derived values, with the values for equation 4.6 being more than double the observed values.

With the addition of the observed PERCA data, the gap between the observed and calculated equation 4.6' comes to a minimum. During the morning hours, the agreement between the theoretically calculated equation 4.6' and the observed ratio is excellent. The fact that the PERCA data can close the gap between the theoretically calculated ratios and the observed ratios re-enforces the theory that indeed the high NO_2 concentrations measured during the campaign are not due to systematic errors of the CLD instrument. This is strong evidence, since the CLD instrument used to measure the NO_2 data and the PERCA instrument used to measure the ROx data are completely independent of each other and used separate inlet lines. However, they both indicate that based on the observations done in this study, there is an additional missing chemical mechanism converting NO to NO_2 in the remote MBL, which is not accounted for in the PSS ratio and therefore leads to much higher theoretically calculated NO/ NO_2 ratios.

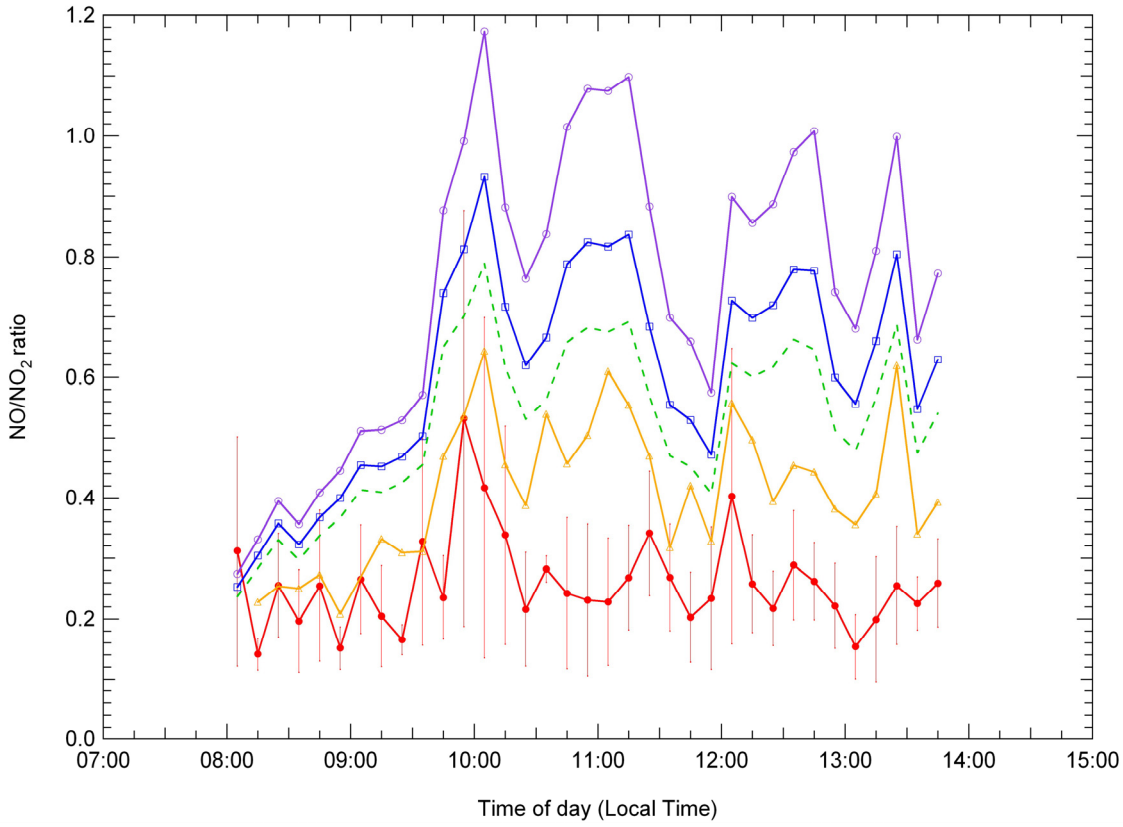

Figure 4.15 Observed NO/NO_2 ratios (solid red circles with bars) compared with calculated values derived from equation 4.4 (open purple circles), equation 4.5 (open blue squares), equation 4.6 (dashed green line) and equation 4.6' (yellow line) for March 15th, 2007.

The role of this oxidant is thought to be unimportant in air masses with high NOx concentrations. In the following sections, further evidence is provided on how this missing oxidation mechanism seems to be photochemically driven. Even though the PERCA and CLD measurements compliment each other, the PERCA signal is still regarded as unexpectedly high and goes against all evidence presented to date on the concentration of ROx in comparison to HOx (see section 4.2.5).

Table 4.4 Average values, STDEV, maximum and minimum values for each ratio on March 15th

NO/NO_2 Ratio	Average	STDEV	Max.	Min.
Equation 4.4	0.75	0.25	1.17	0.27
Equation 4.5	0.61	0.18	0.93	0.25
Equation 4.6	0.53	0.14	0.79	0.24
Equation 4.6'	0.42	0.12	0.64	0.21
(NO/NO_2) observed	0.24	0.14	0.73	0.1

Since OH and HO_2 were measured independently using a LIF instrument, these values are an asset when comparing total PERCA signal and the RO_2 values, which can be derived from the PERCA data once HO_2 and OH are known. What is interesting is the difference between the assumed RO_2 values and the actual RO_2 derived from the measured PERCA signal. Since OH and HO_2 were measured independently using a LIF instrument, these values are an asset when comparing total PERCA signal and the RO_2 values which can be derived from the PERCA data once HO_2 and OH are known. What is interesting is the difference between the assumed RO_2 values and the actual RO_2 derived from the measured PERCA signal.

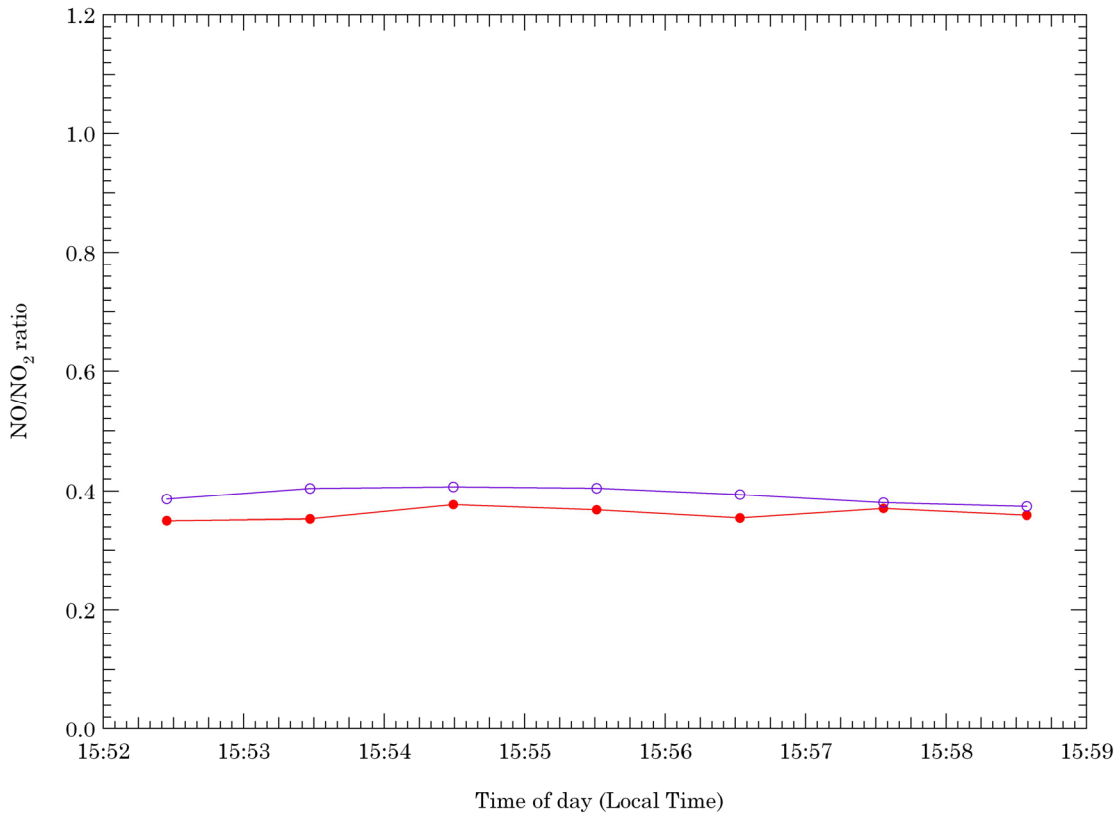

Figure 4.16 The observed NO/NO_2 ratios (solid red circles) and calculated equation 4.4 (open purple circles) for March 15th 2007 for the high NOx episode resulting from the passing of a second ship.

Even though the PERCA does close the gap between theoretically calculated values and the observed ratio during some periods of the day (figure 4.15), there is still a

difference between the average observed ratio and the averaged equation 4.6' for other periods of the day. This could be due to additional unknown chemistry or simply be due to the high uncertainty in the ratio which is expected in low NOx regimes.

For a comparison between the observed and calculated NO/NO_2 ratio during the pristine conditions mentioned above and a high NOx episode, data obtained during the passing of a 2nd ship on March 15th, has been used. As can be seen in figure 4.16 in contrast to the pristine background period, the observed NO/NO_2 ratio is in excellent agreement with the theoretically calculated equation 4.4. In addition, the calculation of the Leighton ratio revealed that PSS is established ($\varphi = 1$), even without the inclusion of the HO_2 and RO_2 concentrations into the equation. This confirms the theory that under high NOx conditions the peroxy radicals do not play a significant role in the photochemical processes governing the NOx- O_3 system. This indicates that under relatively high NOx conditions the PSS of NOx and O_3 seems to be well understood and that the theoretically calculated PSS ratio is in excellent agreement with observed values. It is therefore concluded that the Leighton ratio is only valid for conditions with a significant concentration of NOx and as seen from the above calculations not valid for clean background conditions of the remote MBL. Therefore, we conclude that the observed low NO/NO_2 ratios suggest a missing chemical mechanism.

4.2.3 Leighton equation and PSS

In this section, in order to compare the effect of the peroxy radicals on the Leighton ratio, calculations were done using both equations 4.1 and 4.2. In a later step, these two equations are compared. We assume that PSS is established, since conditions for the establishment of PSS, i.e. unperturbed air masses (stable concentrations of NOx and O_3) and sufficient radiation (JNO_2 filtering), are met for the study periods. The Leighton ratio calculated for each individual clean background period is presented in figure 4.17. The colour bar indicates the JNO_2 intensity. Note that the axis range of the JNO_2 values (the colour bar) are different on each individual day and should therefore not be compared directly with each other. In order to get a better overview, data from all periods of study mentioned in tables 4.1 and 4.2 have been plotted in figure 4.18.

Figure 4.18 illustrates the total Leighton ratio tendency during different NOx regimes. Measurements were carried out under different levels of pollution. Therefore the investigation of the Leighton ratio is divided into three distinctive periods of pristine background MBL conditions NOx <30 ppt_v, South African air mass 100 ppt_v < NOx < 500 ppt_v and the passing of the second ship 1 ppb_v < NOx < 2 ppb_v. The colour bar indicates the JNO_2 intensity.

During the pristine background periods of measurement, considerable deviation is seen from unity, as was predicted and expected from previous studies. However, noteworthy is the trend seen in the low NOx regime values of Φ that is of interest and goes against previous expectations. There is a clear trend in the pristine air masses which is seen in both the individually plotted periods in figure 4.17 and the overall plot in figure 4.18. It would have been expected that the maximum deviations from unity to be at the lowest end of the measured NOx values i.e. around 5 ppt_v and for the deviation to decrease with increasing NOx.

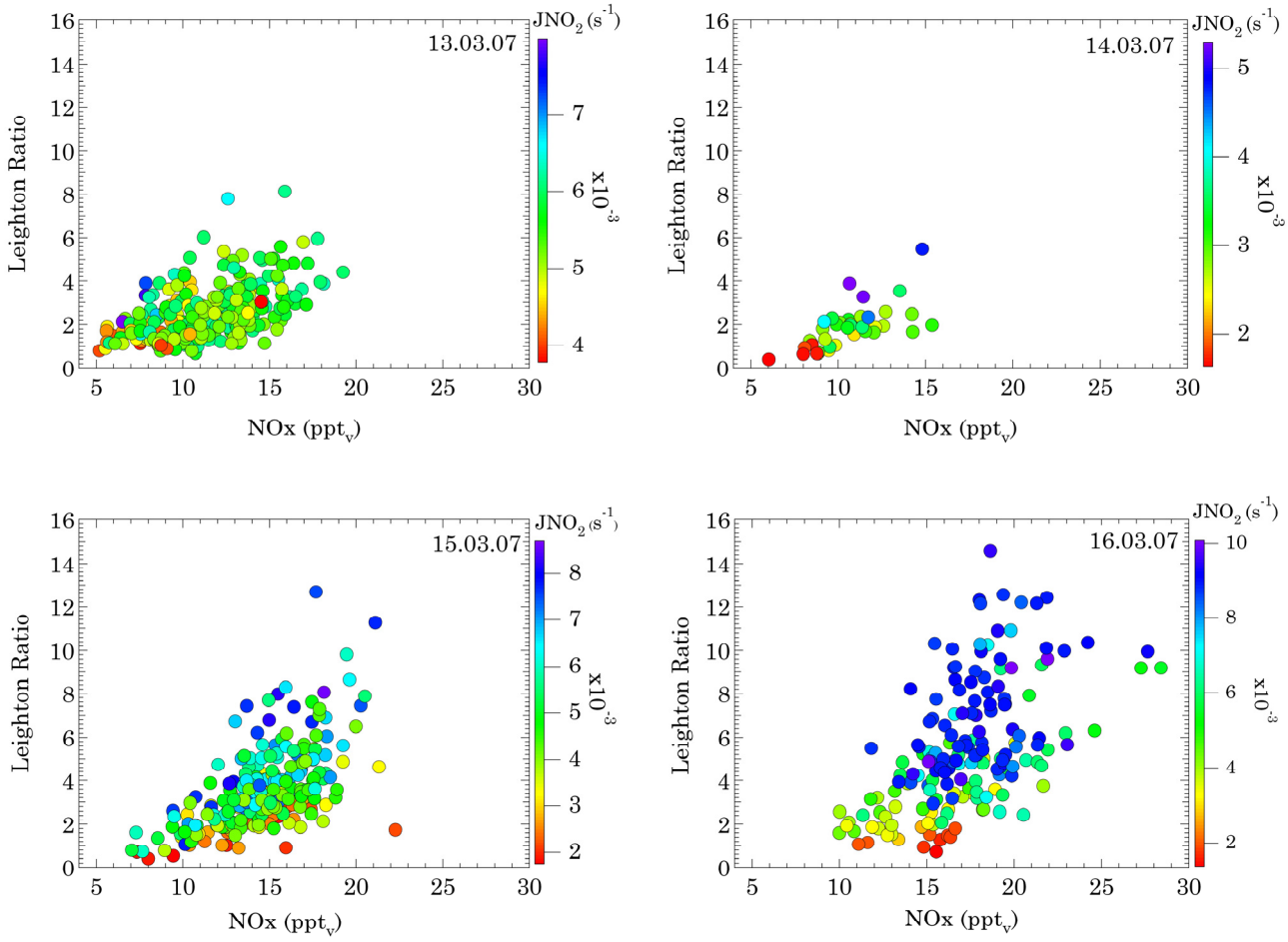

Fig. 4.17 The classic Leighton ratio (equation 4.1) for clean background conditions is plotted as a function of NOx mixing ratios. The colour coding corresponds to the JNO_2 intensity. Plots are for March 13th, 14th, 15th and 16th.

This trend is actually observed in the South African air masses and passing ship period i.e. with an increase in NOx mixing ratios, up to 2 ppb_v in this case, there is a decrease in the deviations and φ inclines towards unity. This is clearly in agreement with what has so far been observed and predicted by previous studies e.g. (Zoellner, 2008). However, one has to take into account that during these past two episodes where deviations do indeed decrease with increasing NOx, the NOx levels are already in the order of 100 ppt_v, which is relatively high compared to the clean background observations.

The JNO_2 colour coding clearly illustrates that the maximum deviations in Φ are not at the lowest NOx and JNO_2 values as predicted in previous studies. In fact, at NOx mixing ratios of less than 15 ppt_v the Leighton ratio is close to unity (within the uncertainty of Φ). What is observed is that the maximum deviations are at the highest NOx mixing ratios measured in the pristine MBL (between 15 to 25 ppt_v) and the highest JNO_2 intensity (approximately 0.01 s^{-1}), which is completely unexpected and could be an indication of photochemically driven chemistry.

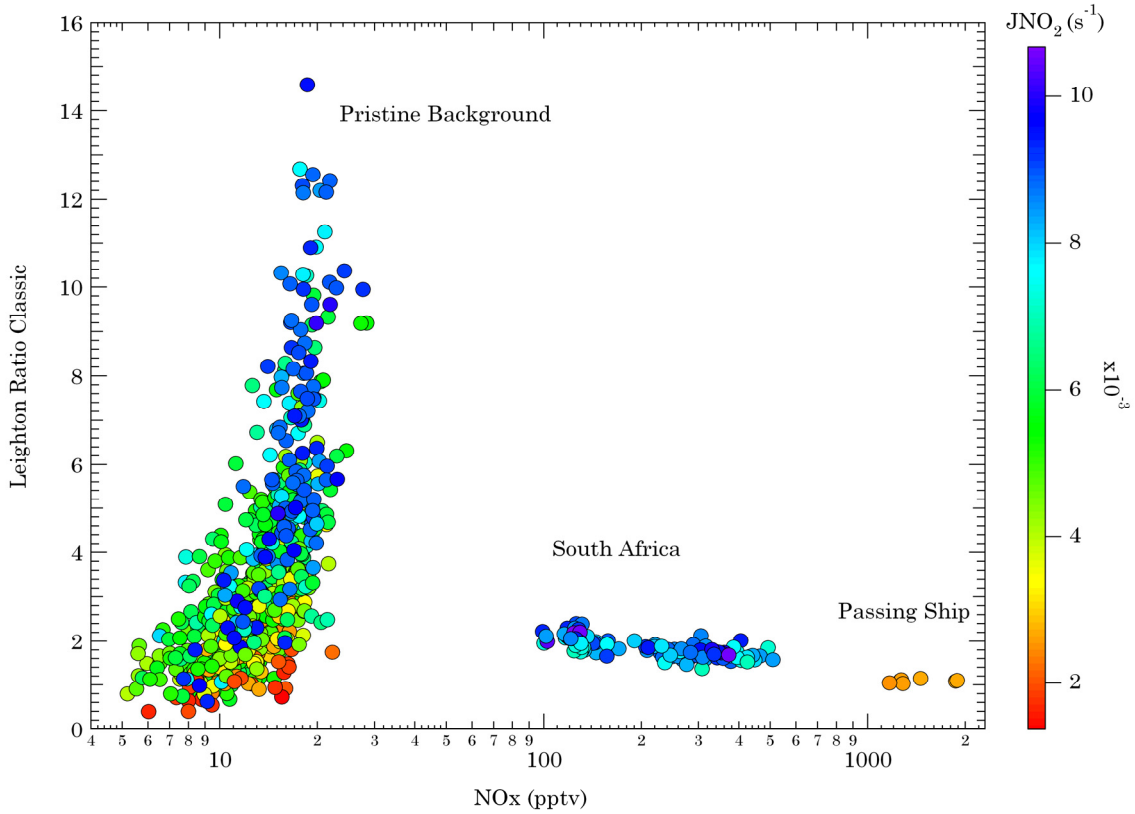

Fig 4.18 Leighton ratio values for all days are plotted against NOx mixing ratios (logarithmic scale). The colour bar indicates the JNO_2 intensity.

Unfortunately, no data is available for the region between 30 to 100 ppt_v. It is supposed that a trend might also be seen in this region, opposite to that of the 5 to 30 ppt_v NOx range. That is, with the increase in NOx levels the deviation of Φ would most likely decrease until it reaches the values of the continental air at 100 ppt_v. This would be due to the fact that with the increase in NOx mixing ratios, the reaction of NO with O_3 would be the main oxidation pathway to convert NO to NO_2 and therefore other pathways would be of insignificance. Reactions that would otherwise be rendered important in the pristine background conditions are of insignificance in higher NOx regimes. This result confirms the fact that the Leighton ratio should be used with the utmost caution in clean background regions as it can lead to gross errors. During measurement of South African air masses with NOx mixing ratios between 100 to 500 ppt_v, Φ is close to unity (within the ratio's uncertainty). When NOx levels are at the maximum value of 1.5 ppb_v, during the passing of a second ship, the ratio is equal to unity. The average JNO_2 value during this period is 0.003 s^{-1}. This again confirms the fact that Leighton ratio is an excellent tool and can be used to predict components of the NO-NO_2 and O_3 system for relatively high NOx regimes. However, at the same time the results from this study indicate that as there is a lack of thorough understanding of the chemistry of the remote background conditions of the globe, e.g. unknown oxidation pathways, the utmost care should be practised when using the ratio.

This study is unique in the sense that for the first time the PSS is investigated in a region with NOx levels observed on the order of 5 to 30 ppt_v. What is observed in figure 4.18 is a new phenomenon. Clearly this trend is interesting in the sense that at

low NOx levels there is possibly an unknown photochemically driven process which is of insignificance at NOx mixing ratios above 100 ppt_v. In order to further investigate and explain this trend, measurements need to be made in conditions where NOx mixing ratios are below 100 ppt_v. In an ideal situation, measurements should be carried out with both a BLC-CLD and a LIF instrument for inter-comparison, as was done during a recent campaign, DOMINO 2008, on the Northern Atlantic coast in Spain. Inter-comparison of data from the two different methods showed excellent agreement. However due to measurements being on land and not in the remote MBL during the recent campaign, observed NOx data was not in the exceptionally low ppt_v range measured during MD 160, therefore a comparison was only feasible for relatively higher NOx concentrations.

In a second step in order to investigate the effect of HO_2 and RO_2 on the Leighton ratio, calculations were done using Equation 4.2. Analysis could only be carried out for periods were peroxy radical data was available, therefore there are fewer data points in figure 4.19 compared to 4.18.

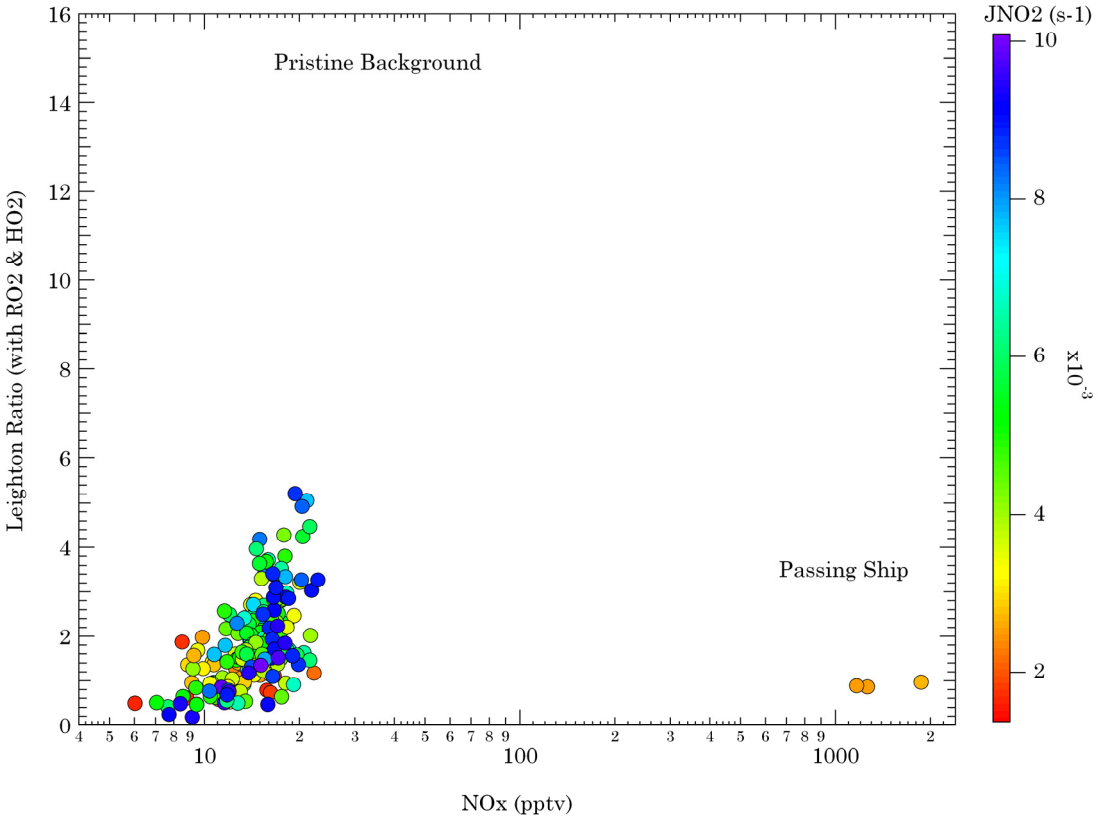

Figure. 4.19 Leighton ratio plotted as a function of NOx mixing ratios (logarithmic scale) using equation 4.2. The colour bar indicates the JNO_2 intensity.

The values for the passing ship period have not changed and are similar to those plotted in figure 4.18. This is a strong confirmation of the insignificance of ROx reactions in high NOx regimes. However, dramatic change can be observed in the Leighton ratio of the pristine background conditions. That is, the maximum deviation seen in figure 4.19 is approximately five, compared to the much higher value of 15 which was seen in figure 4.18. The new results for the PSS ratio are still high compared to unity; however they are significantly lower than results obtained through

the use of the classic Leighton ratio. This confirms the important role played by peroxy radicals in low NOx regimes. The trend seen in the deviation in the pristine background air masses does not change. In fact, the trend is exactly the same as in the case of the classic Leighton ratio and the maximum deviations from unity are again seen at around the 20-30 ppt_v NOx levels. Also, the trend seen in the higher JNO_2 intensity is also observed in this case, with maximum deviations being at the highest JNO_2 intensities. This may again be an indication for an unknown photochemically driven oxidant that can convert NO to NO_2 and therefore lead to significant deviations from unity.

For NOx mixing ratios in the ppt_v range the uncertainty resulting from the measurement of NO and NO_2 dominates the overall uncertainty which increases with decreasing NOx. Uncertainty rates for PSS calculations have been reported up to 60% (Mannschreck et al., 2004). The uncertainty in this study is mainly caused by the uncertainty in the NO and NO_2 concentration, and is less affected by the other parameters in the equation. The overall uncertainty in φ can be calculated through the sum of the individual uncertainty in each parameter using the following equation:

$$\Delta\varphi = \sqrt{\varphi^2 . \sum \left(\frac{\Delta X_i}{X_i} \right)^2} \qquad \text{(Equation 4.8)}$$

X_i in the above equation stands for JNO_2, NO, NO_2, HO_2, O_3 and RO_2, depending on which form of the PSS equation used. For example, for equation 4.1 the uncertainty would be calculated as equation 4.8:

$$\Delta\varphi = \sqrt{\varphi^2 . \left(\left(\frac{\Delta JNO_2}{JNO_2} \right)^2 + \left(\frac{\Delta NO_2}{NO_2} \right)^2 + \left(\frac{\Delta k_3}{k_3} \right)^2 + \left(\frac{\Delta O_3}{O_3} \right)^2 + \left(\frac{\Delta NO}{NO} \right)^2 \right)} \qquad \text{(Equation 4.9)}$$

With the addition of parameters to the equation, the resulting additional uncertainties are added to the total uncertainty of the ratio. The uncertainties for equations 4.1 and 4.2 in this study are 16.1 % and 53.2 % respectively. Clearly, these limits are insufficient to explain the discrepancy shown in the figures above.

4.2.4 Comparison between filtered and unfiltered data

There were concerns that the third "DL" filter (see section 3.5.3 of Chapter three) may affect the outcome of the analysis due to the removal of data below the detection limit of the CLD. Therefore, the PSS calculations were carried out using both the DL filter (results shown in figure 4.18) and without (see figure 4.20). The y-axis on figure 4.20 has been plotted up to an axis range of Φ=16 in order to make an exact comparison to figure 4.18. The filtered data are represented as green circles and the unfiltered data as red circles. Since the filter only removes data below the DL, no difference is seen in the values for the South African and passing ship periods. A comparison of the two data sets for the pristine background conditions revealed that there were no significant changes in regard to the overall outcome of the calculations.

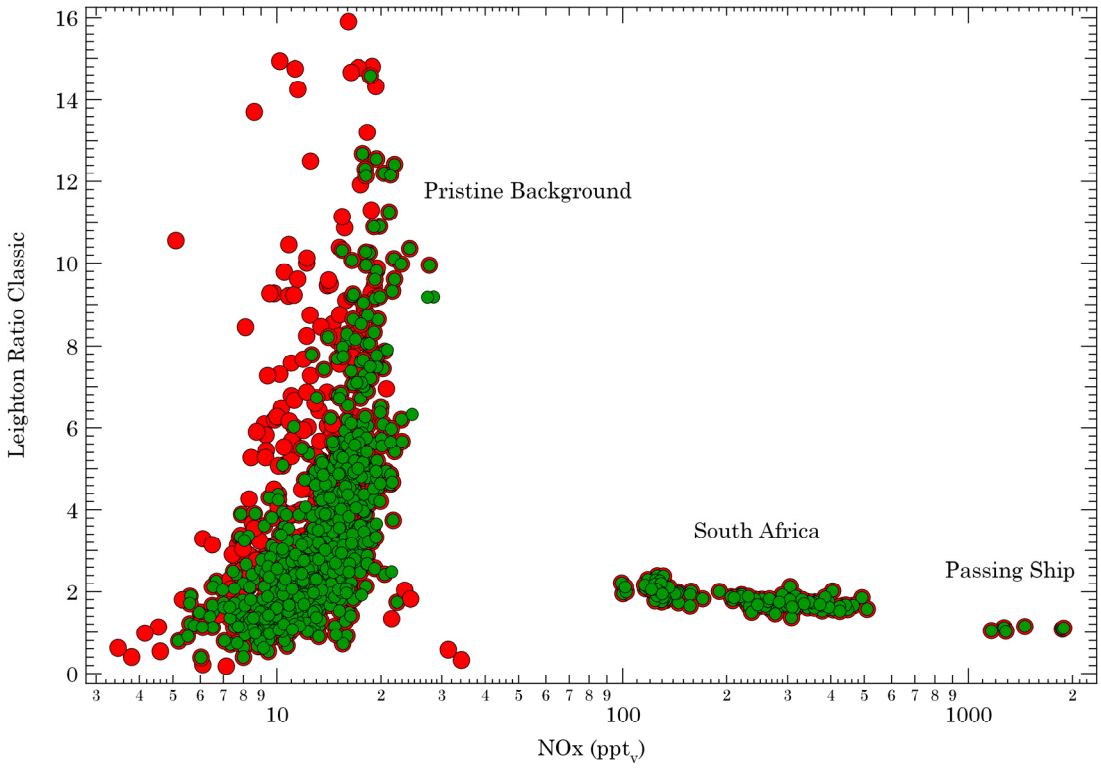

Figure 4.20 Leighton ratio values for all days are plotted against NOx mixing ratios (logarithmic scale) for both the filtered and unfiltered data sets. Green and red circles represent the filtered and unfiltered data respectively. The axis here is limited to Φ=16.

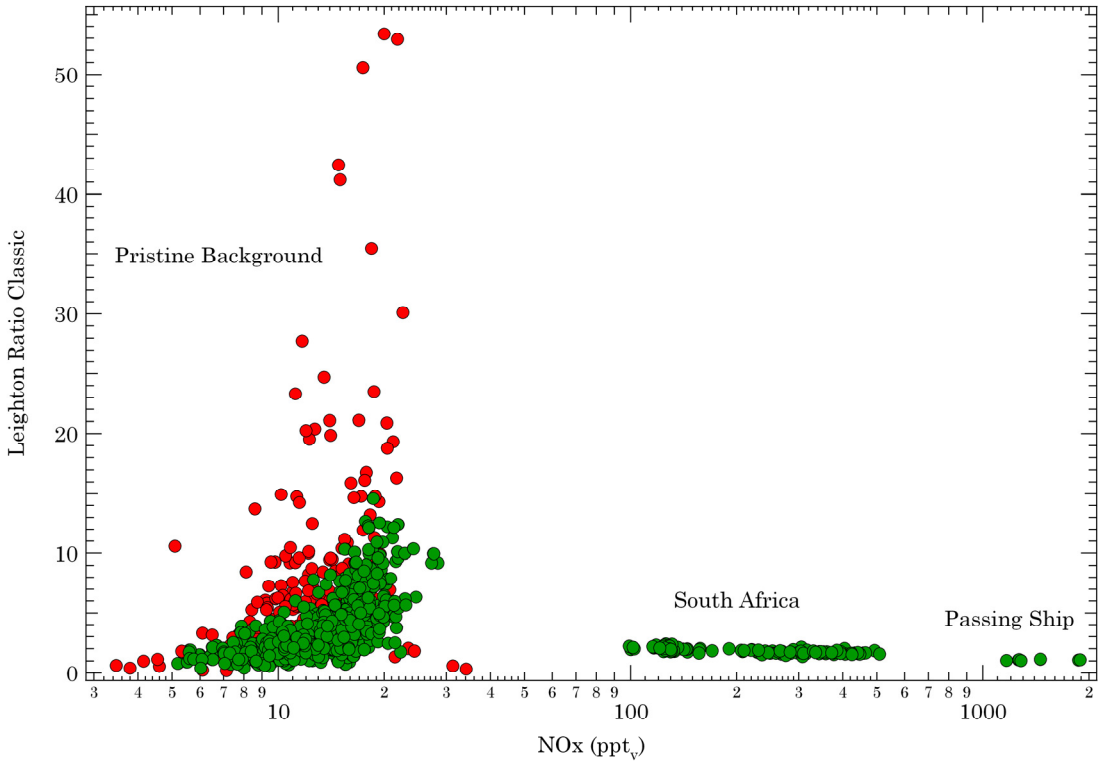

Figure 4.21 Leighton ratio values for all days are plotted against NOx mixing ratios (logarithmic scale) for both the filtered and unfiltered data sets. Green and red circles represent the filtered and unfiltered data respectively.

In fact, as can be observed in the figure above the overall deviation of the Leighton ratio from PSS in the pristine background air demonstrated the same trend. Maximum deviations in the Leighton ratio are again at the higher end of the NOx mixing ratios measured in the pristine MBL. The comparison between filtered and unfiltered data has been made a second time in figure 4.21 with the axis range set at a maximum of Φ=55 to include all data from the unfiltered dataset.

4.2.5 Comparison between observed and calculated NO_2

In order to better understand the significance of the deviations in the Leighton ratio, in this section we look directly at the theoretically calculated NO_2 which can be derived from the PSS equation in the form of:

$$[NO_2]\text{calc.} = \frac{(k_3[O_3]+k_4[HO_2]+k_5[RO_2])[NO]}{JNO_2} \qquad \text{(Equation 4.10)}$$

A direct comparison between the observed NO_2 and the theoretically calculated NO_2 derived from equation 4.10 is made in the form of a ratio between these two values.

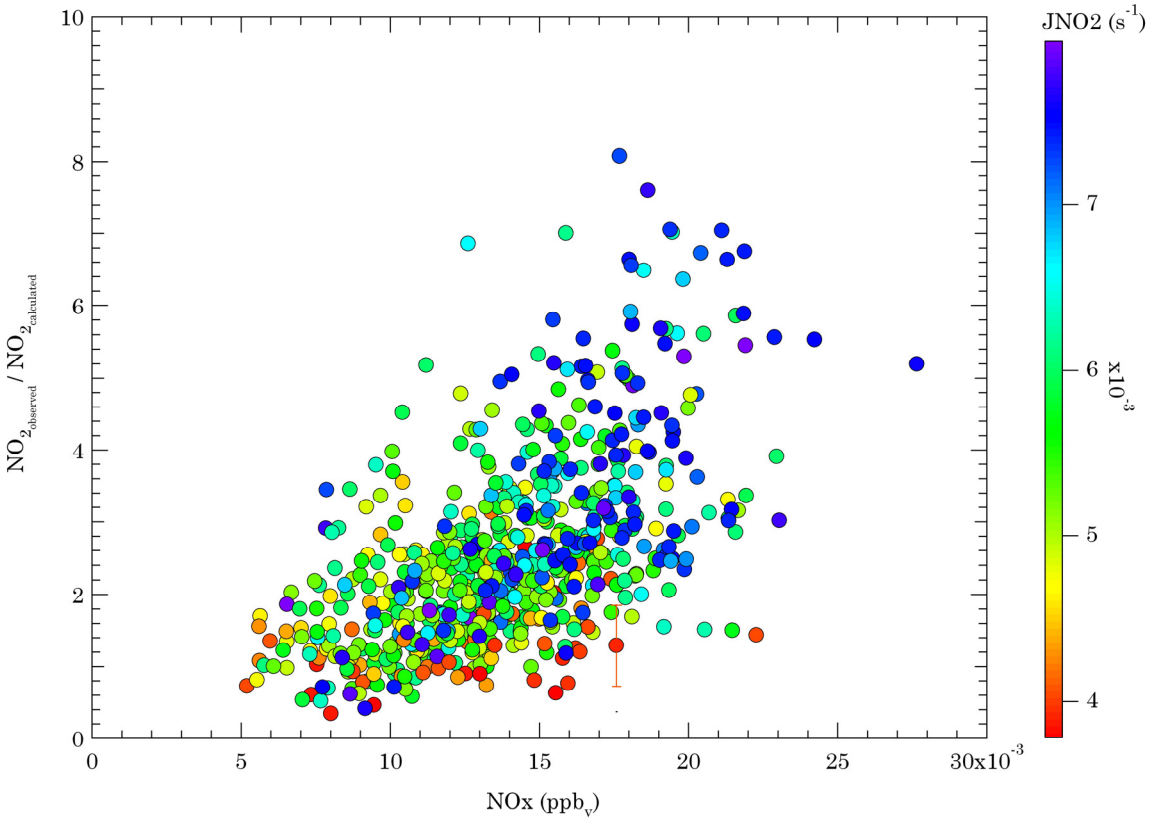

Figure 4.22 The observed NO_2 to calculated NO_2 ratio is plotted as a function of NOx mixing ratios for the pristine background air masses of the MD 160 cruise. The colour bar represents the JNO_2 intensity. The error bar on the single point is for an estimate of the uncertainty factor in this study.

The ratio between the measured and theoretically calculated NO_2 would be expected to equal unity if indeed these two values were equal. However, the ratio which has been plotted as a function of NOx mixing ratio in figure 4.22 clearly indicates that this is not the case. The uncertainty for the theoretically calculated NO_2 is 52.7%. In fact, at the deviation point maxima, NO_2 observations are on average a factor of 7 higher than the theoretically calculated NO_2 values. This clearly indicates the role of a chemical process which converts additional NO to NO_2. The maximum deviations are correlated to periods with the highest JNO_2 intensity. The periods with the relatively low JNO_2 intensities are actually the periods where the ratio approaches unity. This clearly indicates that the additional NO to NO_2 conversion process is photochemically driven as it has its biggest impact on the ratio during periods when JNO_2 is highest. The same calculations were done for the high NOx episodes in that case the calculated and observed values were more or less in good agreement.

4.2.6 Organic peroxy radicals and hydroperoxy radicals

4.2.6.1 Previous observations and assumptions

Numerous studies and experiments have been carried out where measurements of peroxy radicals were compared with those obtained through models and theoretically calculated values. These combined field and modelling investigations of the peroxy radical budget and of ozone formation have been undertaken to test the current understanding of photochemistry. These measurements were carried out under different levels of pollution, ranging from 0.1 ppb_v to more than several ppb_v of NOx (Cantrell et al., 1997, Carpenter et al., 1998, Hauglustaine et al., 1996, Volz-Thomas et al., 2003). Generally, RO_2 concentrations calculated from assuming PSS were significantly higher than directly measured values.

4.2.6.2 Observed HOx vs. ROx mixing ratios

Observed OH, HO_2 and ROx values are presented in figure 4.23. Noteworthy is the axis range for the three species. Maximum OH values are a little over 1 ppt_v. HO_2 goes up to a maximum of 18 ppt_v while the ROx mixing ratios maxima reaches approximately 200 ppt_v.

As can be observed from figure 4.23, the HO_2 and OH mixing ratios are very low, as would be expected in the remote MBL of the southern Atlantic. However, the total ROx data obtained from the PERCA instrument is unexpectedly high. It is generally believed that the ROx signal is the sum of the following species:

$$ROx = OH + RO + HO_2 + RO_2 \qquad \text{(Equation 4.11)}$$

As the concentrations of OH and RO are extremely low, their effect on the total sum of ROx can be assumed to be negligible. This would leave the two parameters HO_2 and RO_2 as the main components of the total ROx signal. Since the concentration of HO_2 is known, RO_2 can be derived from the equation above. This calculation resulted

in extremely high RO_2 levels compared to HO_2 observations. This is in contrast to expectations as discussed in the end of part 4.2.1. In the next sections, we would like to investigate the possible reason for such an extremely large difference between RO_2 and HO_2 measurements. In order to further understand this issue we have examined the problem from different aspects using a variety of observations, models and calculations.

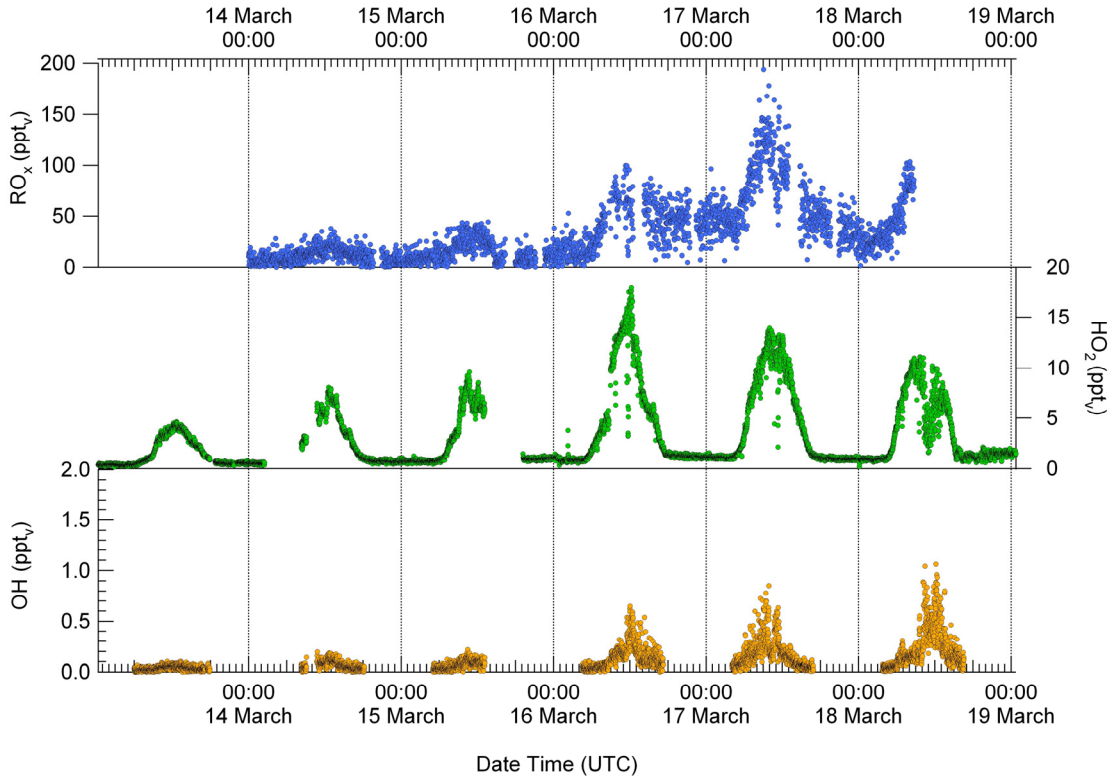

Figure 4.23 Diurnal profiles of OH, HO_2 and ROx from March 13th to 19th.

4.2.6.3 CO/CH_4 ratio

A back-of-the-envelope calculation that is used in order to get an estimate on the levels of RO_2 and HO_2 is the ratio between CO and CH_4. As discussed previously in Chapter one, the chemistry of the remote background troposphere is dominated by the two gases CH_4 and CO. CO reacts with OH, resulting in the formation of a hydrogen atom:

$$CO + OH + \rightarrow CO_2 + H \qquad \text{(R 4.1)}$$

In a consecutive step, this atom goes on to react with O_2 to yield HO_2:

$$H + O_2 + M \rightarrow HO_2 + M \qquad \text{(R 4.2)}$$

CH_4 also reacts with OH to produce CH_3:

$$CH_4 + OH \rightarrow CH_3 + H_2O \qquad \text{(R 4.3)}$$

In a successive step, CH_3 reacts with O_2 to yield CH_3O_2:

$$CH_3 + O_2 + M \rightarrow CH_3O_2 + M \qquad \text{(R 4.4)}$$

From the above reactions the following equation is derived:

$$\frac{K_{OH+CO}[CO]}{K_{OH+CH_4}[CH_4]} = \frac{P[HO_2]}{P[CH_3O_2]} \qquad \text{(Equation 4.12)}$$

The CO/ CH_4 ratio is in fact a good approximation of the formation rates of HO_2 to CH_3O_2, or RO_2 in general (Dr. H. Fischer, personal communication, 2009). If the production of HO_2 and RO_2 are equal then the ratio will equal unity. CH_4 and CO were both measured during the MD 160 cruise. The average CH_4 mixing ratio was 1.68 ppm_v (STDEV=0.02). This value is relatively low, as would be expected in the remote MBL of the southern hemisphere, compared to other parts of the globe. The average CO mixing ratio was 41.42 ppb_v (STDEV=2.85). The K_{OH+CO} and K_{OH+CH4} are the reaction rates for reactions R4.1 and R4.3, respectively.

We find that the ratio of the production terms $P[HO_2]/P[CH_3O_2]$ is 0.84. This can be directly compared with the results of a chemical box model, constrained by measurements (Stickler et al., 2007) and with the output of our chemistry general circulation model (Joeckel et al., 2006). This indicates that this production ratio is actually close to the concentration ratio $[HO_2]/[CH_3O_2]$ and validates the assumption that $[RO_2] \approx [CH_3O_2] \approx [HO_2]$, at least based on current knowledge and state of the art models.

4.2.6.4 ECHAM/MESSY Atmospheric chemistry model

In order to achieve a direct comparison of measurement data with model output, an atmospheric chemistry general circulation model was used to simulate concentrations of trace gases along the exact MD 160 cruise track.

The ECHAM/MESSy Atmospheric Chemistry (EMAC) model is a numerical chemistry and climate simulation system that includes sub-models describing tropospheric and middle atmosphere processes and their interaction with oceans, land and human influences (Joeckel et al., 2006). It uses the Modular Earth Submodel System (MESSy) to link multi-institutional computer codes. The core atmospheric model is the 5th generation European Centre Hamburg general circulation model ECHAM5 (Roeckner et al., 2006). For the present study EMAC was applied in the T42L90MA-resolution, corresponding to a quadratic Gaussian grid of approx. 2.8° by 2.8° in latitude and longitude with 90 vertical hybrid pressure levels up to 0.01 hPa. The model time step in this resolution is 12 minutes. Data was archived every 5 hours simulation time; along the OOMPH transects, data from the model were directly

sampled at model time step resolution. Simulation results from the model provided by Dr. P. Jöckel are plotted in figure 4.24.

For the period of study (i.e. the clean background period of March 13th to 16th), during daylight hours, CH_3O_2 and HO_2 have approximately the same concentrations. This is what would have been expected and in good agreement with results from previous studies and results from the CO/CH_4 ratio.

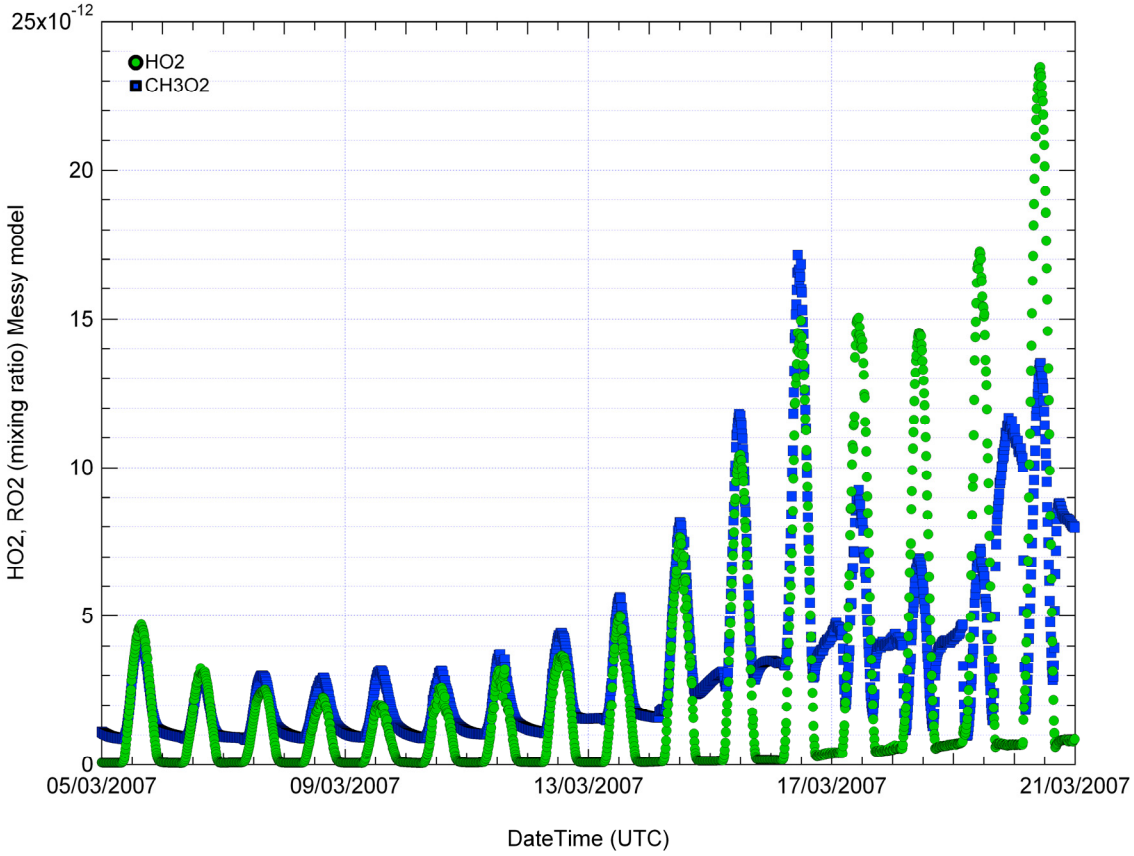

Figure 4.24 Results from the EMAC model simulations for HO_2 (green circles) and CH_3O_2 (blue squares).

4.2.6.5 Steady state box model

In order to investigate the consistency of the measurements and our current understanding of atmospheric radical chemistry, a simple photostationary state balance model was used to simulate the ambient HOx and OH concentrations. The steady-state box model was set up and constrained using data obtained on the MD 160 cruise. Steady state concentrations of OH and HO_2 were calculated. A model data point was calculated whenever the complete set of relevant data was available within a 10 second time frame. Model results provided by Dr. M. Martinez and Dr. H. Harder are plotted in figure 4.25.

PSS conditions were assumed for each of the radical species under consideration, i.e. both OH and HO_2 were assumed to be sufficiently short lived that they remain in

steady state with the ambient conditions. Under photostationary state conditions, the production and loss rates for each of the radicals are assumed to be equal.

$$\frac{d[X]}{dt} \approx 0 = Px - Lx \qquad \text{(Equation 4.13)}$$

where Px represents the total production rate for radical X, and Lx is the corresponding loss rate. This approach was able to reproduce the main features of the diurnal profiles of the radicals. As can be seen in figure 4.25, again the HO_2 and CH_3O_2 data have more or less the same concentrations. On March 16th and 17th there is slightly more CH_3O_2 at noon (a few ppt_v), but this amount would be expected. These results are in good agreement with the CO/CH_4 ratio and EMAC model predictions.

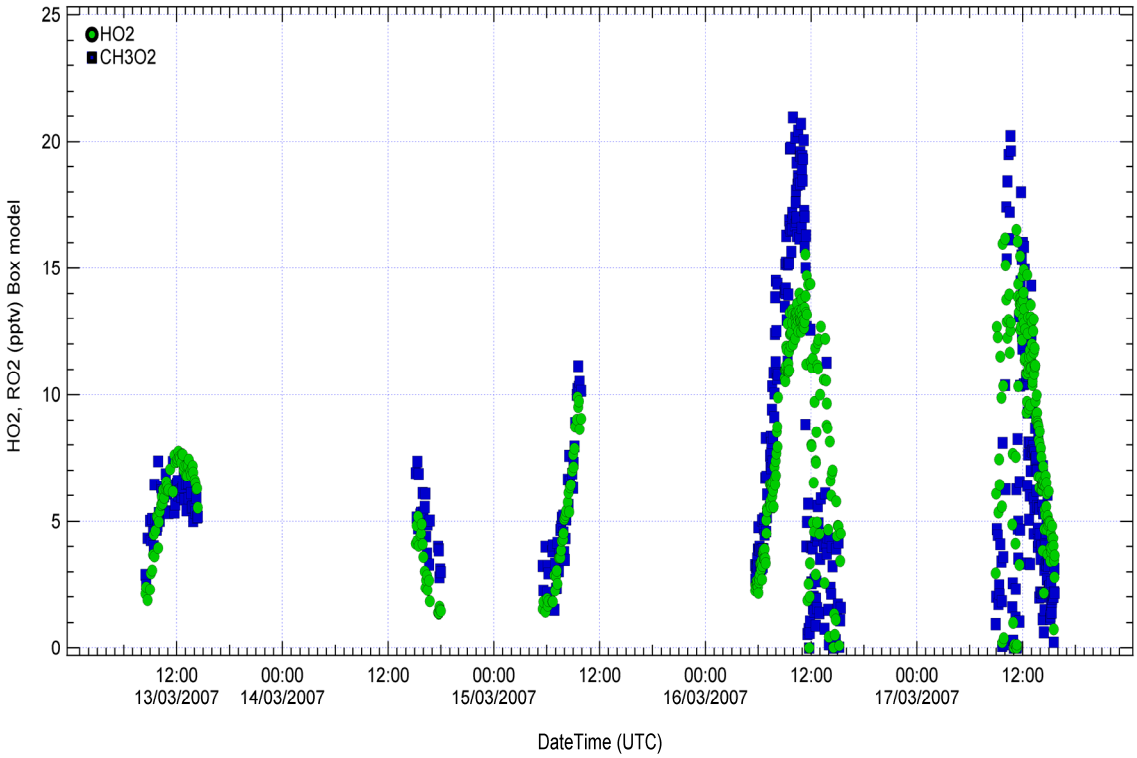

Figure 4.25 Day time results from the steady state box model simulations for HO_2 (green circles) and CH_3O_2 (blue squares).

4.2.6.6 Discussion on peroxy radical concentrations

It is well known that methods for estimating peroxy radical concentration from other measured parameters do not agree with observations (e.g. (Cantrell et al., 1997)). The calculated values are systematically higher than the measurements. This could be due to systematic errors in the measured data used to calculate RO_2. A second possibility is that there is an unknown oxidant of NO which converts NO to NO_2 in excess of the reaction of NO with ROx. Results presented in sections 4.2.4.1 to 4.2.4.5 indicate that

CH_3O_2 values in the remote MBL are expected to be more or less the same concentrations as HO_2. This is contradicted by the extremely high observed PERCA signals. At the same time, the high PERCA signals seem to be in good agreement and a possible explanation for the high NO_2 to NO concentrations measured by the CLD instrument. In fact, with the inclusion of the PERCA signal in the PSS ratio the deviations from PSS are decreased substantially to a minimum (see figure 4.19). However, it is deemed unlikely that CH_3O_2 (or RO_2 in general) concentrations are a factor of ten higher than HO_2 in the remote MBL.

Therefore, in light of the evidence presented in sections 4.2.4.1 to 4.2.4.5, the most likely explanation for the gross overestimation of the PERCA signal would be that the response of the instrument is not entirely due to the measurement of peroxy radicals. It is assumed to be a possibility that the additional signal in the PERCA instrument is created by an oxidant other than peroxy radicals. In the next section, we assess a potential candidate which is known to cause a signal in the chemical amplification method.

4.2.6.7 PERCA method and potential interferences

Chemical amplification is a method commonly used for the detection of peroxy radicals. The measurement principle of the PERCA method is based on the OH/HO_2 radical catalysed simultaneous chain oxidation of CO to CO_2 and NO to NO_2:

$$HO_2 + NO \rightarrow NO_2 + OH \quad \text{(R4.5)}$$

$$OH + CO \rightarrow CO_2 + H \quad \text{(R4.6)}$$

$$H + O_2 + M \rightarrow HO_2 + M \quad \text{(R4.7)}$$

RO_2 measurement first requires the conversion of RO_2 to HO_2 via the following reactions:

$$RO_2 + NO \rightarrow NO_2 + RO \quad \text{(R4.8)}$$

$$RO + O_2 \rightarrow RCHO + HO_2 \quad \text{(R4.9)}$$

$$\rightarrow R\text{-}CO\text{-}R + HO_2 \quad \text{(R4.10)}$$

Subsequently, HO_2 is detected through the same cycle as the first three reactions mentioned above. Therefore, any oxidant that can convert NO to NO_2 and has a sufficiently long chain length (i.e. the number of conversion cycles that occur before termination) can be detected via the chemical amplification method. In a study carried out by Perner et al., it was concluded that the chemical amplification method is sensitive to oxidants other than ROx and HOx (Perner et al., 1998). They observed that the method was sensitive towards ClOx ($Cl+ClO+ClO_2$). It was found that ClOx is reduced by NO to Cl atoms which react with CO in the presence of O_2:

$ClO + NO \rightarrow Cl + NO_2$ (R4.11)

$Cl + CO + M \rightarrow ClCO + M$ (R4.12)

The reaction sequence which is initiated oxidizes CO to CO_2 and NO to NO_2:

$ClCO + O_2 + M \rightarrow ClCO_3 + M$ (R4.13)

$ClCO_3 + NO \rightarrow Cl + CO_2 + NO_2$ (R4.14)

The chain length for ClOx species in the study by Perner et al. was reported to be 300±60. In parallel, peroxy radicals are indicated with a chain length of 160 ± 15. Therefore, the chain length for ClOx is approximately a factor of two higher than that of the peroxy radicals. It is believed that the ClOx chain length could be up to a factor of 10 higher compared to the peroxy radical chain length (Dr. J. Crowley, personal communication, 2009). This would of course result in a significant impact on the total observed ROx signal. The conclusion of Perner et al. was that the chemical amplification method is not specific and does not indicate which radical chain it is seeing. Therefore the PERCA signal can be defined as below:

PERCA signal= $RO_2 + RO + HO_2 + OH + X$ (Equation 4.14)

X in the above equation is the additional unknown oxidant that can oxidize NO to NO_2 in the atmosphere and therefore lead to the high NO_2 levels measured during the campaign.

4.2.7 Halogen monoxides and the PSS equation

As described in detail in the first chapter of this thesis, halogen monoxides have been proposed as potential candidates for the 'unknown oxidant' (Mannschreck et al., 2004, Matsumoto et al., 2006). Even though very small concentrations of XO are thought to exist in the remote MBL, the cycle does seem to affect the O_3 cycle and contributes to O_3 destruction. Since, as described above, it is believed that not all the PERCA signal is due to ROx concentrations. Calculations were done to test the affect of XO on the Leighton ratio. The RO_2 values used in the calculation were based on the assumption that RO_2 concentrations were equal to HO_2 concentrations. Subsequently, the concentrations of XO (X = Br, Cl or I) needed to minimize the deviation from unity were calculated using the following equation:

$$\Phi = \frac{JNO_2[NO_2]}{(k_3[O_3]+k_4[HO_2]+k_5[RO_2]+k_7[XO])[NO]}$$ (Equation 4.15)

where k_3, k_4, k_5 and k_7 are the rate coefficients for reactions 1.3, 1.4, 1.5 and 1.7, respectively, in Chapter one. Note that the rate constants for the reactions of XO with NO (for BrO, ClO and IO) are very close to each other (Atkinson et al., 2007).

In order to explain the deviations in the Leighton ratio in this study, ClO mixing ratios of more than 15 ppt_v would be required. This is difficult to imagine, as O_3 concentrations are on average between 18 to 24 ppb_v during the period of this study. If indeed such high XO levels existed in the atmosphere outside the Polar Regions, O_3 levels would be approximately zero. These high XO mixing ratios do not match observations and model predictions which have been reported previously for this area of the world (see figure 1.5). It is worth mentioning that Prof. J.M.C. Plane and Dr. R. Sander have each made an educated guess of 1-2 ppt_v of halogen monoxide (ClO or BrO) for the remote South Atlantic where the data used in this study were obtained (personal communication, 2008). This is in no way comparable to the high values derived from the Leighton ratio.

4.2.8 Uncertainty related to rate coefficients

The uncertainty related to the rate coefficients of relevant reactions, k_i, is of course included in the overall uncertainty of the PSS calculations. It is believed that whilst k_i does in fact contribute to the overall uncertainty of the results, there is little dispute over the actual k_i values themselves. This was noticed in the sensitivity tests carried out on the PSS calculations using two sources for rate coefficients, i.e. Sanders and Atkinson (Atkinson et al., 2004, Sander et al., 2006).

The two coefficients rates agreed well within the range of uncertainty. Therefore, it is concluded that the large deviations seen in the Leighton ratios can not be due to the relatively small uncertainty in the k_i values.

In a later stage, another sensitivity test was carried out in relation to rate coefficient values, in this case specifically for ROx calculated from the PSS expression ($[ROx]_{PSS)}$. It has been suggested in previous studies that reaction rate coefficients could be critical for PSS calculations of ROx (Matsumoto et al., 2006). It was found that the reaction rates of NO with HO_2 and RO_2 are critical for PSS estimation and that $[ROx]_{PSS}$ can be influenced by uncertainties in the rate coefficients. It was found that deviations could be caused by the assumption that, for all radicals, reaction rate coefficients of RO_2 with NO are similar to that of HO_2. This assumption has been made frequently in previous studies.

4.3 Summary and Conclusions

To our knowledge, this is the first study in the remote MBL were the PSS of NOx and O_3 has been studied in a region where NOx values are in the order of 5 to 20 ppt_v. Most previous studies of this kind have only looked at PSS down to a NOx mixing ratio of 100 ppt_v, which is already relatively high compared to the pristine conditions measured on this campaign. Therefore, there is a need for more measurements to be carried out in order to better understand the unique processes which are unknown but are of significant importance in the remote regions of the globe.

The most important finding is that at very low NOx concentrations the Leighton ratio can be valid in the remote MBL. Significant deviation from unity is only seen with an increase in JNO_2 values ($\Phi>1$). Therefore, the deviation from unity is not at minimum NOx concentrations and JNO_2 values as suggested in previous studies. This may indicate some additional unknown photochemistry taking place at higher JNO_2 values in a low NOx regime.

Measurements of pollution from a ship on collision course with our ship in the remote southern Atlantic leads to the conclusion that PSS is established in a matter of minutes once large concentrations of NOx are released into the remote southern Atlantic. It was found that during high NOx regimes (1.5 ppb_v), PSS is established without taking into account the effect of RO_2 and HO_2. It is believed that high NOx levels suppress peroxy radicals' concentrations; therefore these radicals can not cause deviations in the Leighton ratio.

In the mid NOx values (150 ppt_v) and below, the addition of HO_2 and RO_2 is important. With the decrease in NOx concentrations, RO_2 and HO_2 chemistry gains more importance.

The comparison between measured and model calculated ROx concentrations (low NOx regime) shows that the theory failed to reproduce the observations. This indicates that species convert NO to NO_2 in excess of the reaction between NO with O_3 and the peroxy radicals. It could also indicate additional sources of NO_2.

In previous studies, the Leighton ratio has been used to estimate levels of NO, NO_2, O_3, HO_2 and RO_2. It is concluded from this study that in non-urban regions the ratio is affected by unknown chemistry, which invalidates its common use as a way of deriving atmospheric trace gas concentrations. The PSS method therefore must be used with the utmost caution, since it is only valid when PSS is reached and when the steady state NOx portioning is entirely dependent on O_3 and the peroxy radicals.

Chapter 5: O_3 destruction in the remote MBL

Introduction

The role of insitu photochemistry in the tropospheric ozone budget is an important topic of interest in atmospheric chemistry. The remote marine boundary layer which may consist of up to 25 % of the total atmosphere is an ideal place to study the basic processes that drive photochemistry due to its stable and relatively simple nature. The net effect of photochemistry in the remote MBL is to destroy O_3. It is believed that O_3 destruction is balanced by entrainment into the MBL from the lower free troposphere and that it is relatively constant during the day and night in the remote MBL.

The ability of the atmosphere to produce or destroy ozone is a non-linear function dependant on the availability of nitrogen oxides (NOx = NO + NO_2) and volatile organic compounds precursors. In the low NOx conditions of the remote southern Atlantic boundary layer, O_3 is predominantly lost through photolysis and an electronically excited oxygen atom is produced:

$$O_3 + h\nu \rightarrow O_2 + O(^1D) \qquad (\lambda<320 \text{ nm}) \qquad \text{(R5.1)}$$

The $O(^1D)$ atom can either be quenched to the ground state by collision with nitrogen (N_2) and oxygen (O_2) molecules or can react with water vapour to produce hydroxyl radicals (OH):

$$O(^1D) + H_2O \rightarrow 2OH \qquad \text{(R5.2)}$$

Therefore, only a fraction (α) of $O(^1D)$ atoms react with H_2O to produce OH rather than being collisionally deactivated (Fischer et al., 2003). This fraction is estimated to be around 10 % in the lower atmosphere and is strongly dependant on the availability of water vapour. In this study calculations reveal that α can on average vary from 5 % to 13 % over a period of a few days. However, α is more or less constant during a single day in the background conditions of the remote MBL.

Additional losses of O_3 are due to the following reactions:

$$HO_2 + O_3 \rightarrow OH + 2O_2 \qquad \text{(R5.3)}$$

$$OH + O_3 \rightarrow HO_2 + O_2 \qquad \text{(R5.4)}$$

Reactions R5.3 and R5.4 coupled to O_3 photolysis (R5.1) leads to net O_3 destruction in low NOx regimes. However, even at low NOx concentrations there is a small positive contribution to the overall photochemical O_3 budget from the photolysis of NO_2.

5.1 Results and discussions

The specific objective of this study is to (1) take a closer look at the relationship between O_3, the peroxy radicals and $JO(^1D)$; (2) investigate the O_3 budget based on theoretically assumed and measured peroxy radical concentrations in the remote MBL; (3) assess O_3 production based on the PSS expression; (4) investigate the O_3 compensation point in the remote MBL of the southern Atlantic ocean using clean background data obtained on the MD 160 cruise in March 2007.

5.1.1 Peroxy radicals, Ozone and $JO(^1D)$

The background profiles for O_3, hydroperoxy radicals (HO_2) and organic peroxy radicals (ROx) are presented in figures 5.1.a and 5.2.b for March 15th and 16th respectively. The tendency of the species is consistent and representative of clean background air in a low NOx environment in the MBL. The negative correlation exhibited in figures 5.1.a and 5.2.b, between peroxides and O_3, indicates net photochemical destruction of O_3 and the subsequent production of OH and HO_2 in the remote MBL. This behaviour is in good agreement to those observed in previous studies e.g. (Monks et al., 1998).

Ozone photolysis via reactions R5.1 and R5.2 is believed to be the primary source of OH in the low NOx conditions of the remote MBL. In turn OH oxidation of CO and CH4 is the major driving force of peroxy radical (HO_2 and CH_3O_2) production (see R5.8, R5.9, R5.19 and R5.20 of Chapter one). The peroxy radicals that are generated are mainly lost due to self-reactions of peroxy radicals with themselves:

$$HO_2 + HO_2 \rightarrow H_2O_2 + O_2 \qquad \text{(R5.5)}$$

$$HO_2 + RO_2 \rightarrow ROOH + O_2 \qquad \text{(R5.6)}$$

In a study by Penkett et al. (Penkett et al., 1997) it has been demonstrated that the sum of peroxy radicals can be expressed as:

$$[HO_2] + [RO_2] = \left(\frac{JO(^1D)[O_3]\alpha}{k'} \right)^{\frac{1}{2}} \qquad \text{(Equation 5.1)}$$

Where α is the fraction of $O(^1D)$ atoms that react with H_2O to produce OH rather than being collisionally deactivated. The composite rate coefficient, k', of reactions R5.7 and R5.8 is given by:

$$k' = a^2 k_7 + a(1-a)k_8 \qquad \text{(Equation 5.2)}$$

$$HO_2 + NO \rightarrow NO_2 + OH \qquad \text{(R5.7)}$$

$$RO_2 + NO \rightarrow NO_2 + RO \qquad \text{(R5.8)}$$

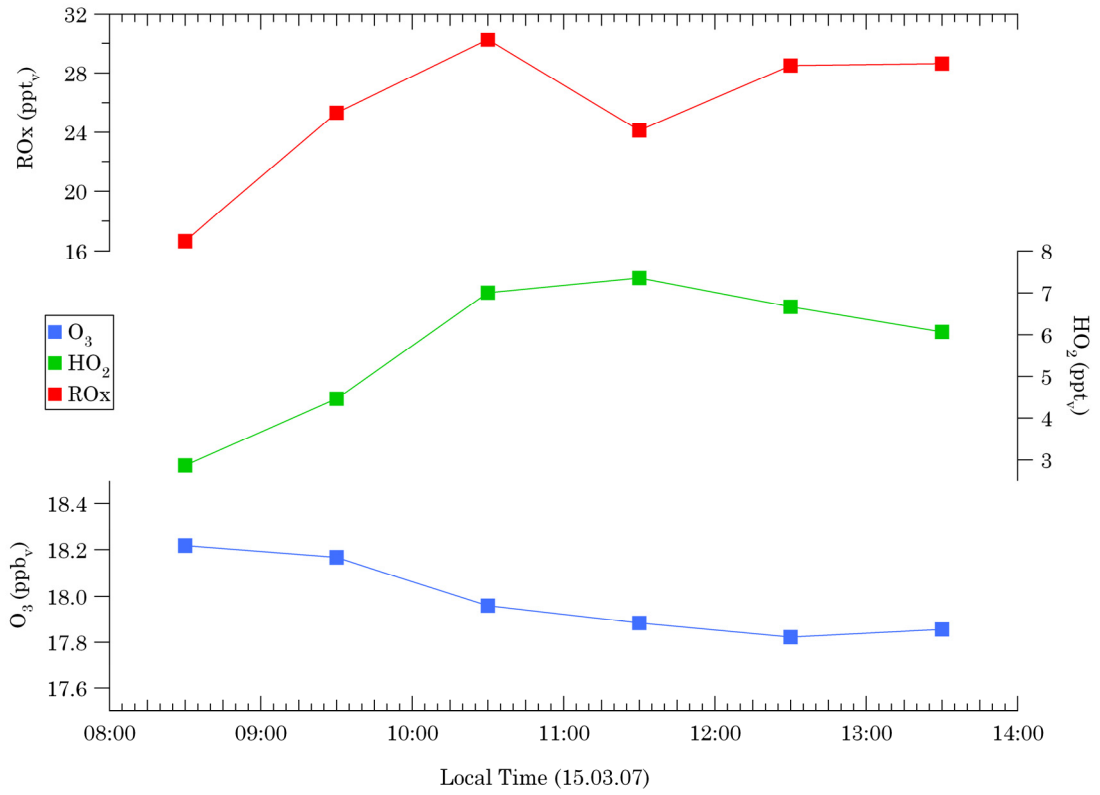

Figure 5.1.a Presented are the hourly averages of ROx, HO_2 and O_3 for background daytime period on March 15th. Blue, green and red squares represent O_3, HO_2 and ROx respectively.

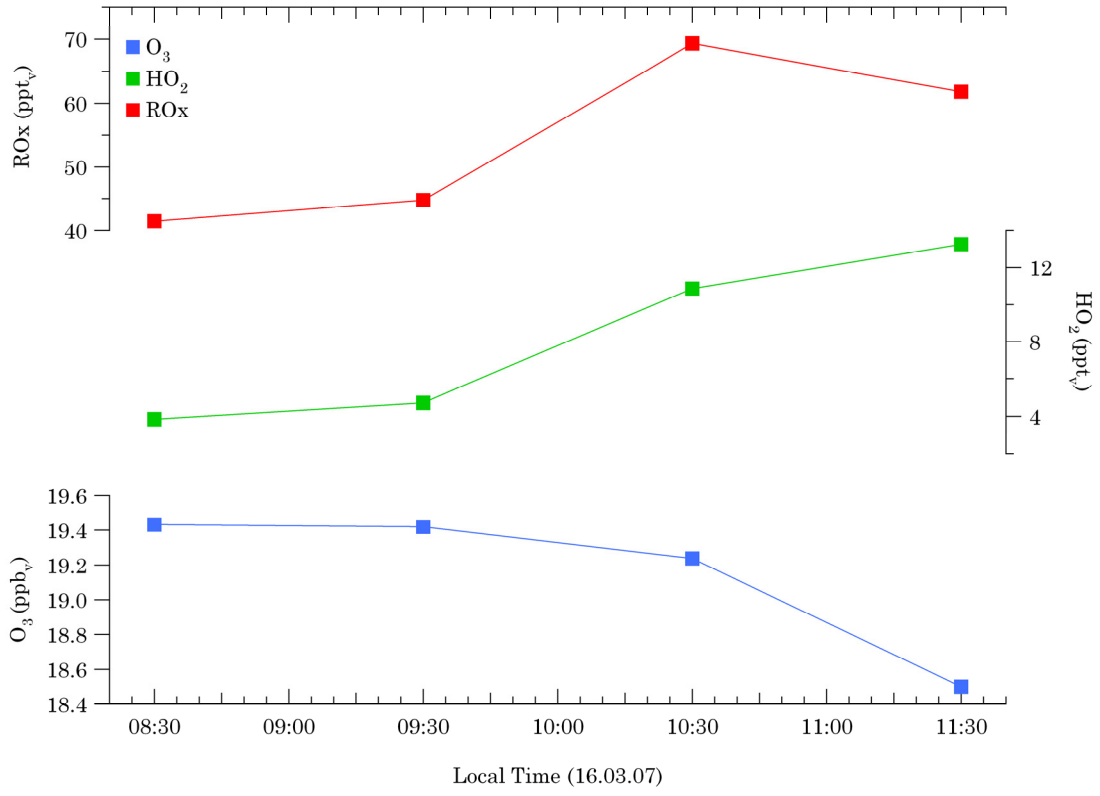

Figure 5.1.b Presented are the hourly averages of ROx, HO_2 and O_3 for background daytime period on March 16th. Blue, green and red squares represent O_3, HO_2 and ROx respectively.

Where 'a' is the ratio $[HO_2]/([HO_2]+[RO_2])$. Therefore, it can be concluded from equation 5.1 that peroxy radical concentrations are proportional to the square root of $JO(^1D)$ in clean background conditions.

It is well known that atmospheric chemistry is largely driven by the photo-dissociation of trace gases. This makes accurate determination of the photolysis rates as important as that of the trace gas concentrations when atmospheric chemistry is investigated insitu.

Figures 5.2.a, 5.2.b, 5.2.c, 5.2.d illustrate the diurnal cycle for ROx and HO_2 versus the square root of $JO(^1D)$ ($\sqrt{JO(^1D)}$) for March 13th, 14th, 15th and 16th respectively. What can generally be seen in all figures is that the concentrations of peroxy radicals increases with the increase in $JO(^1D)$ after sunrise and throughout the day and follows changes in the $JO(^1D)$ values. The ten-minute averaged radical concentrations tracked $\sqrt{JO(^1D)}$ closely during the clean background periods, where O_3 photolysis is believed to be the main driving force for radical production. As observed in the figures below the HO_2 mixing ratios track $JO(^1D)$ more closely in comparison to the ROx values.

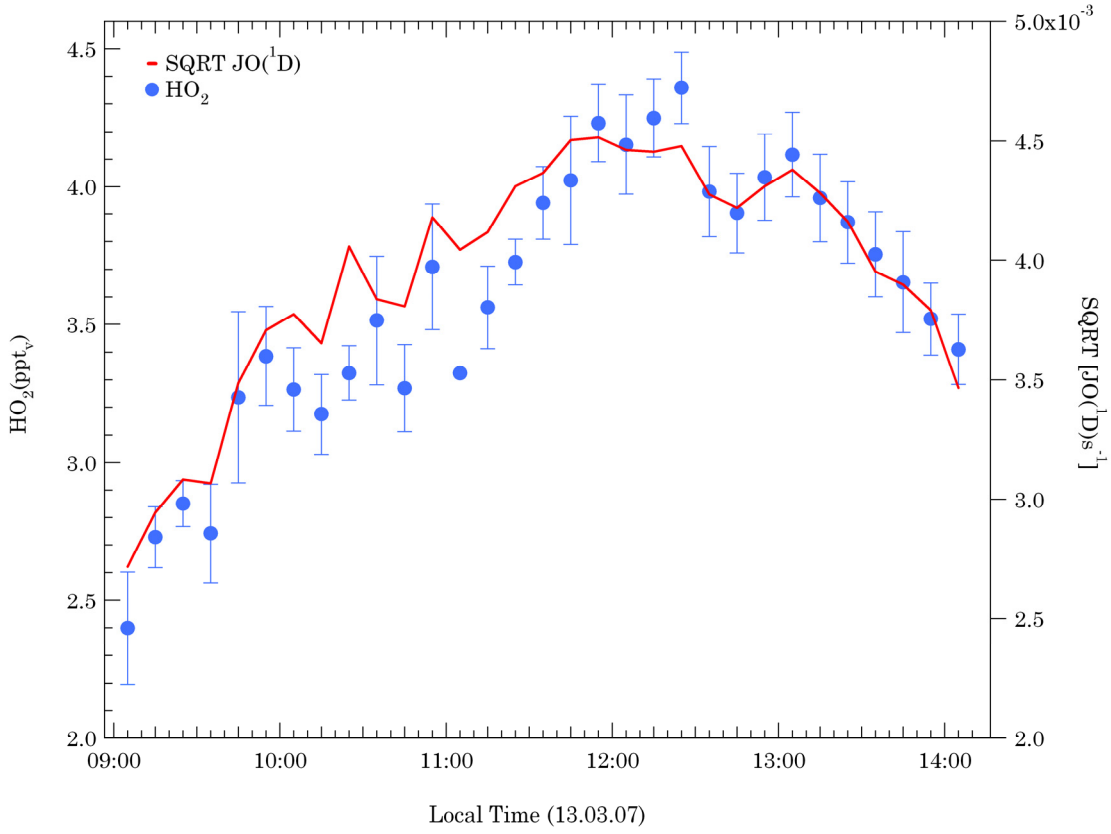

Figure 5.2.a Time series of ten-minute averaged HO_2, ROx and $JO(^1D)$ during background conditions on March 13th. Blue circles represent HO_2 mixing ratios and $JO(^1D)$ is represented as red crosses and line.

Carpenter et al. found that net O_3 destruction was observed when peroxy radical concentrations were proportional to $\sqrt{JO(^1D)}$ and net O_3 production occurred when peroxy radicals concentrations were proportional to the first power of $JO(^1D)$ (Carpenter et al., 1997).

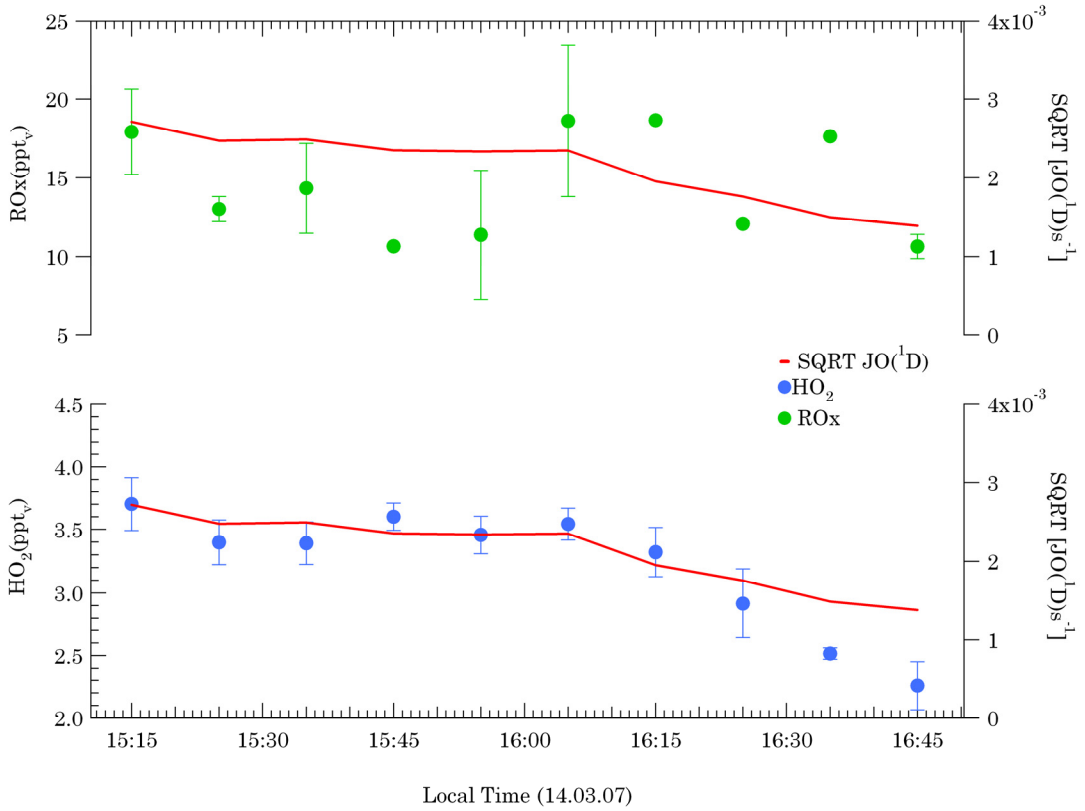

Figure 5.2.b Time series of ten-minute averaged HO_2, ROx and JO(^{1}D) during background conditions on March 14th.

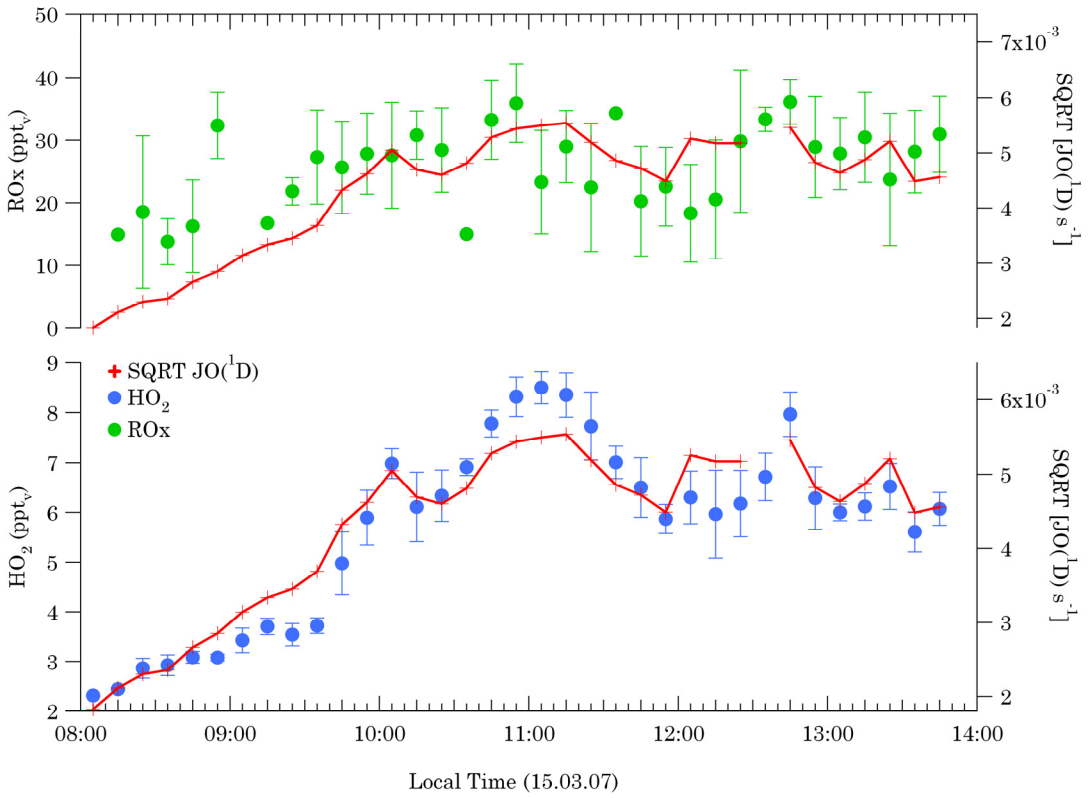

Figure 5.2.c Time series of ten-minute averaged HO_2, ROx and JO(^{1}D) during background conditions on March 15th.

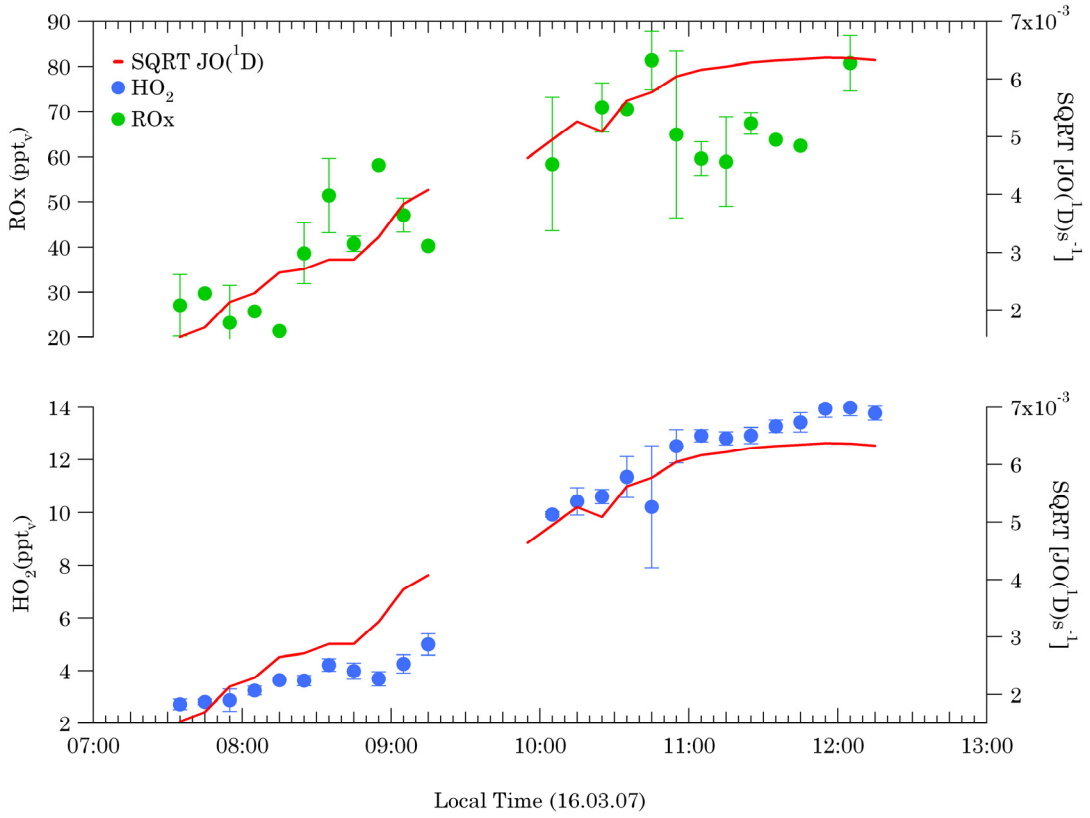

Figure 5.2.d Time series of ten-minute averaged HO_2, ROx and $JO(^1D)$ during background conditions on March 16th.

5.1.2 Ozone Tendency based on measured peroxy radicals

As explained previously in Chapter one, the rate of O_3 production ($P(O_3)$), O_3 loss ($L(O_3)$) and the net O_3 tendency ($T(O_3)$) can be expressed as:

$$P(O_3)=\{k_7[HO_2] + k_8[RO_2]\}[NO] \qquad \text{(Equation 5.3)}$$

$$L(O_3) = k_3[HO_2][O_3] + JO(^1D)[O_3]\alpha + k_4[OH][O_3] \qquad \text{(Equation 5.4)}$$

$$T(O_3) = \{k_7[HO_2]+k_8[RO_2]\}[NO] - \{k_3[HO_2][O_3] + JO(^1D)[O_3]\alpha + k_4[OH][O_3]\} \qquad \text{(Equation 5.5)}$$

where k_3, k_4, k_7 and k_8 are the rate coefficients of reactions 3, 4, 7 and 8 respectively. When calculating $L(O_3)$ it is assumed that loss due to dry deposition, heterogeneous reactions, uptake in cloud droplets and reactions with alkenes is negligible (Fischer et al., 2003). Also losses due to reactions with halogen monoxides are considered negligible. In this study the α term was calculated using the following equation:

$$\alpha = \frac{k_2[H_2O]}{k_9[N_2]+k_{10}[O_2]} \qquad \text{(Equation 5.6)}$$

where k_2 is the rate coefficient of the reaction between H_2O and $O(^1D)$ in R5.2. The rate coefficients k_9 and k_{10} correspond to reactions 5.9 and 5.10 respectively:

$$O(^1D) + N_2 \rightarrow O(^3P) + N_2 \qquad \text{(R5.9)}$$

$$O(^1D) + O_2 \rightarrow O(^3P) + O_2 \qquad \text{(R5.10)}$$

Table 5.1 Mixing ratio averages of trace gases, $JO(^1D)$, temperature and the α factor used in O_3 tendency calculations for March 13th to 16th.

Day	NO (ppt_v)	H_2O,10^{17} ($mol.cm^{-3}$)	O_3 (ppb_v)	HO_2 (ppt_v)	ROx (ppt_v)	$JO(^1D)$ (s^{-1})	T, K	α factor
March 13	3.10	1.72	20.38	3.67	-	$1.63*10^{-5}$	276	0.05
March 14	2.14	2.41	21.26	3.39	14.31	$5.44*10^{-6}$	281	0.07
March 15	2.75	3.16	17.96	5.91	25.91	$2.10*10^{-5}$	284	0.09
March 16	2.76	4.16	18.96	9.80	55.35	$2.73*10^{-5}$	289	0.12

The O_3 loss, production and overall tendency were calculated for clean background conditions using the equations above. The results are presented in figures 5.3 to 5.9 for March 13th to 16th. Each figure is divided into three sections. The lower, middle and top sections contain plots of $L(O_3)$, $P(O_3)$ and $T(O_3)$ respectively.

The lower section in figure 5.3 presents O_3 loss (coloured circles) calculated from equation 5.4 in ppt_v/hr for March 13th. The colour bar represents $JO(^1D)$ intensity. A direct correlation is seen between the $JO(^1D)$ intensity and the O_3 loss levels i.e. the higher the intensity the higher the loss rates. Average $L(O_3)$ on March 13th was 76.0 ppt_v/hr. Maximum loss took place around noon and was 98.3 ppt_v/hr at its peak value.

The $L(O_3)$ equation consists of three different components; the loss of O_3 due to the reactions of (a) HO_2 with O_3, (b) OH with O_3 and (c) O_3 photolysis. Calculations carried out for this experiment showed that the O_3 photolysis component was the major driving force in terms of O_3 destruction and the reaction of O_3 with HO_2 and OH had a less significant role in the overall O_3 destruction taking place. The low O_3 loss rates were expected due to the relatively constant O_3 concentrations during the period of a day (see figures in section 4.2.1, Chapter four).

Since it is not absolutely clear whether the entire PERCA signal is solely due to ROx (section 4.2.5, Chapter four), the $P(O_3)$ in this study was calculated twice. The first set of calculations were done through the use of PERCA derived RO_2 data. The calculations were carried out a second time with the assumption that HO_2 concentrations are equal to those of RO_2 (see section 4.2.5, Chapter four). That is with the exception of March 13th were the calculations for $P(O_3)$ were done only once using the assumed RO_2 concentrations due to the lack of PERCA data for this day. The $P(O_3)$ values on March 13th are presented in the middle section of figure 5.3 as green diamonds. The average $P(O_3)$ on this day was approximately 20 ppt_v. The net ozone tendency can be seen in the top section of figure 5.3 (red triangles). The $T(O_3)$

is on average -56.7 ppt_v/hr, with -83.3 ppt_v/hr and -23.2 ppt_v/hr being the highest and lowest $T(O_3)$ respectively. Since the $T(O_3)$ is clearly negative therefore, it is concluded that the trend in the remote MBL on this day is O_3 destruction.

Figure 5.4 exhibits low O_3 loss rates for March 14th with average $L(O_3)$ at 47.38 ppt_v/hr. This is probably mainly due to the relatively low $JO(^1D)$ intensity measured on this day compared to other days. Maximum O_3 loss was at a rate of 67.94 ppt_v/hr.

The $P(O_3)$ on this day was calculated twice using both PERCA derived RO_2 data ($P(O_3)_{Meas.}$) and also using the assumed RO_2 concentrations ($P(O_3)_{Theor.}$). These results are presented in figure 5.5. The ratio between $P(O_3)_{Meas.}$ and $P(O_3)_{Theor.}$ is represented as black triangles. As can be observed the measured $P(O_3)$ is on average twice as large as the theoretically calculated $P(O_3)$ value.

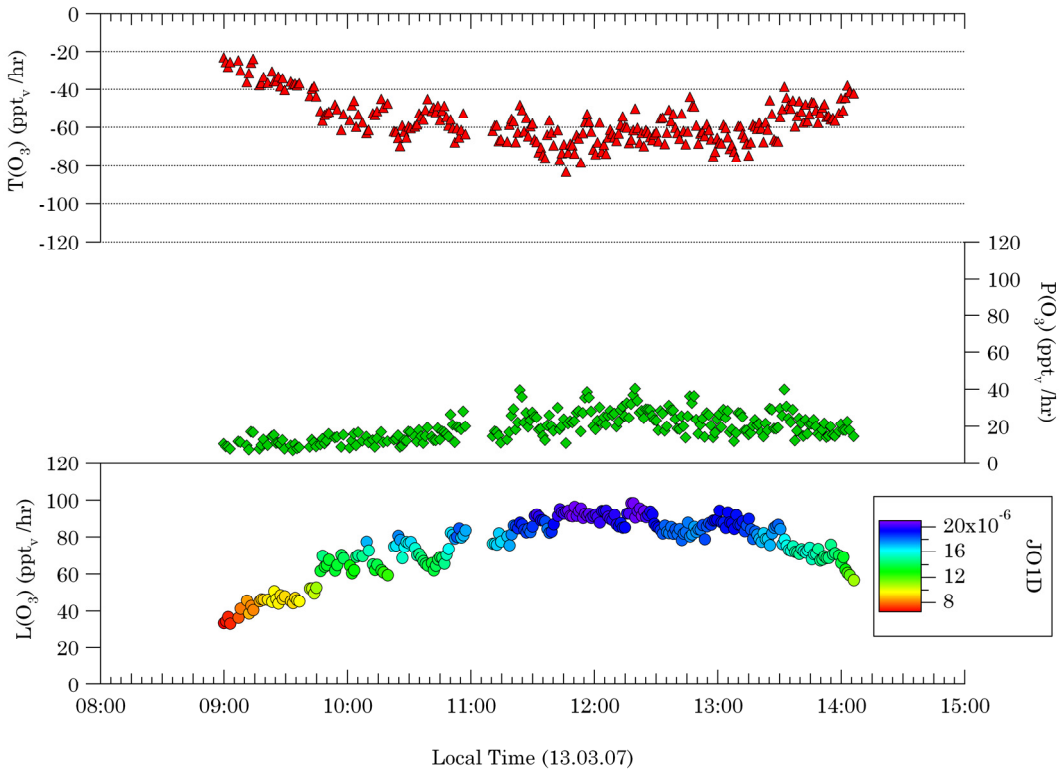

Figure 5.3 One-minute averages of the calculated $L(O_3)$, $P(O_3)$ and $T(O_3)$ in the clean background air masses on March 13th (ppt_v/hr). The colour bar in the $L(O_3)$ section of the graph represents the $JO(^1D)$ intensity (unit is s^{-1}). The $P(O_3)$ in this plot was calculated using the assumption $[HO_2] = [RO_2]$.

The $T(O_3)$ calculated using $P(O_3)_{Meas.}$ in figure 5.4 (top section) is negative and it is concluded that the trend in the remote MBL on March 14th is O_3 destruction, with the average $T(O_3)$ at -21.8 ppt_v/hr. This value is relatively low compared to other days but this is again probably due to the low $JO(^1D)$ intensity on this day compared to other days which results in a smaller loss of O_3. The $T(O_3)$ calculated using the $P(O_3)_{Theor.}$ is on average -35.6 ppt_v/hr and is somewhat higher than the $T(O_3)$ calculated using the measured RO_2 to calculate $P(O_3)$ (not shown here).

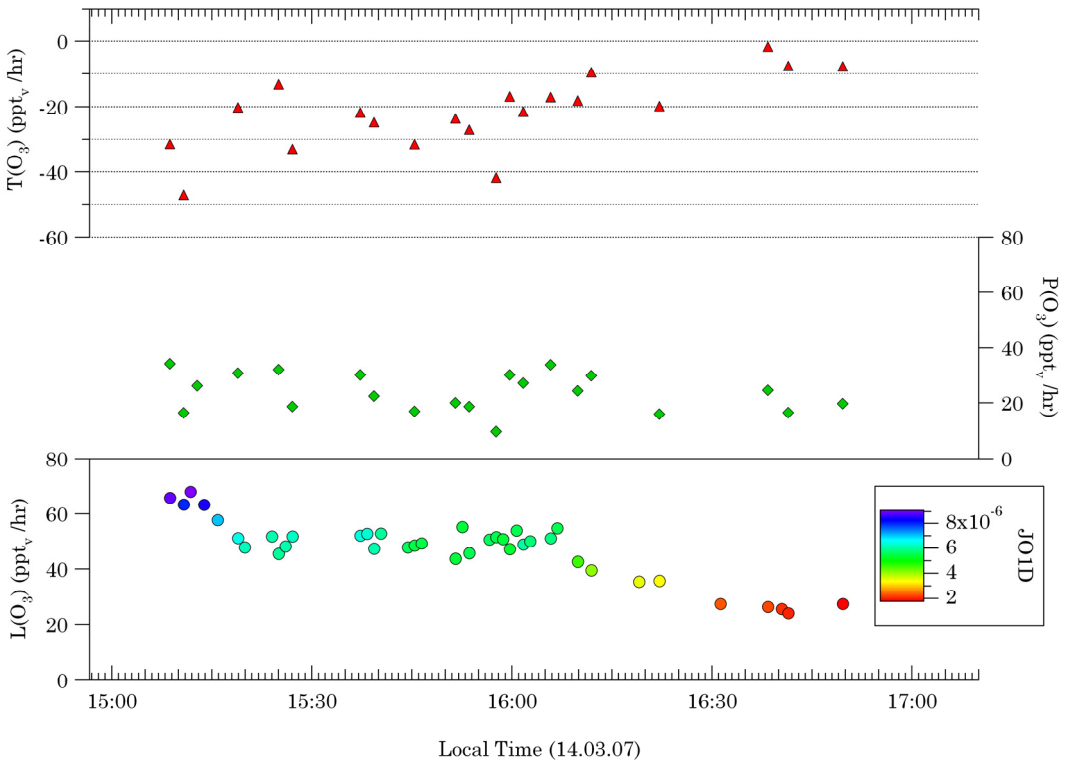

Figure 5.4 One-minute averages of the calculated $L(O_3)$, $P(O_3)$ and $T(O_3)$ in the clean background air masses on March 14th (ppt_v/hr). The colour bar represents the $JO(^1D)$ intensity (unit is s^{-1}). The $P(O_3)$ and $T(O_3)$ values in this plot were calculated using PERCA data.

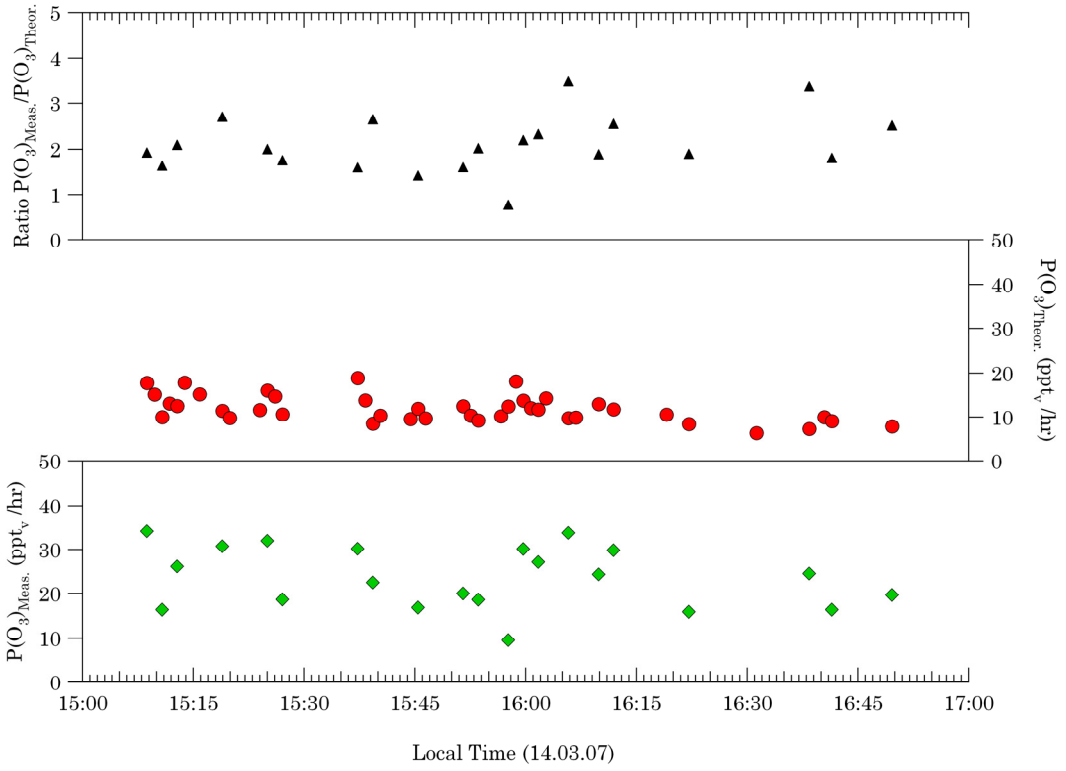

Figure 5.5 Comparison between $P(O_3)$ calculated from the measured data (green diamonds) and the $P(O_3)$ derived from the assumed RO_2 concentrations (red circles), the ratio is represented as black triangles for March 14th.

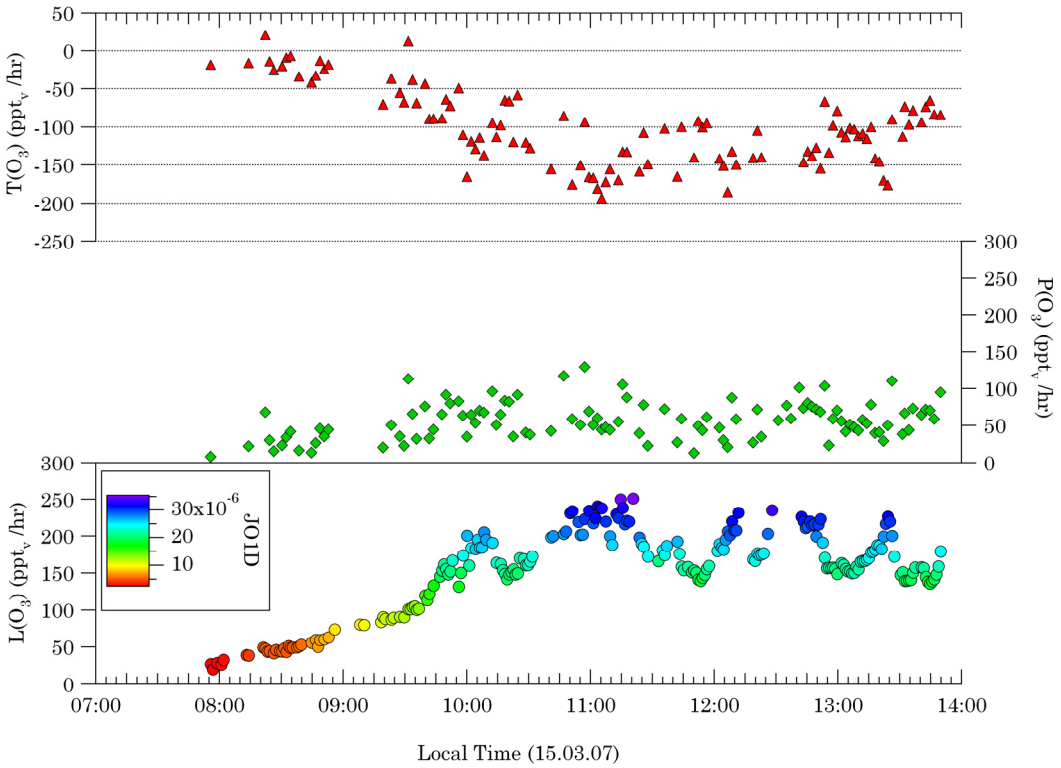

Figure 5.6 One-minute averages of the calculated $L(O_3)$, $P(O_3)$ and $T(O_3)$ in the clean background air masses on March 15th 2007 (ppt_v/hr). The colour bar represents the $JO(^1D)$ intensity (unit is s^{-1}). The $P(O_3)$ and $T(O_3)$ in this plot were calculated using PERCA data.

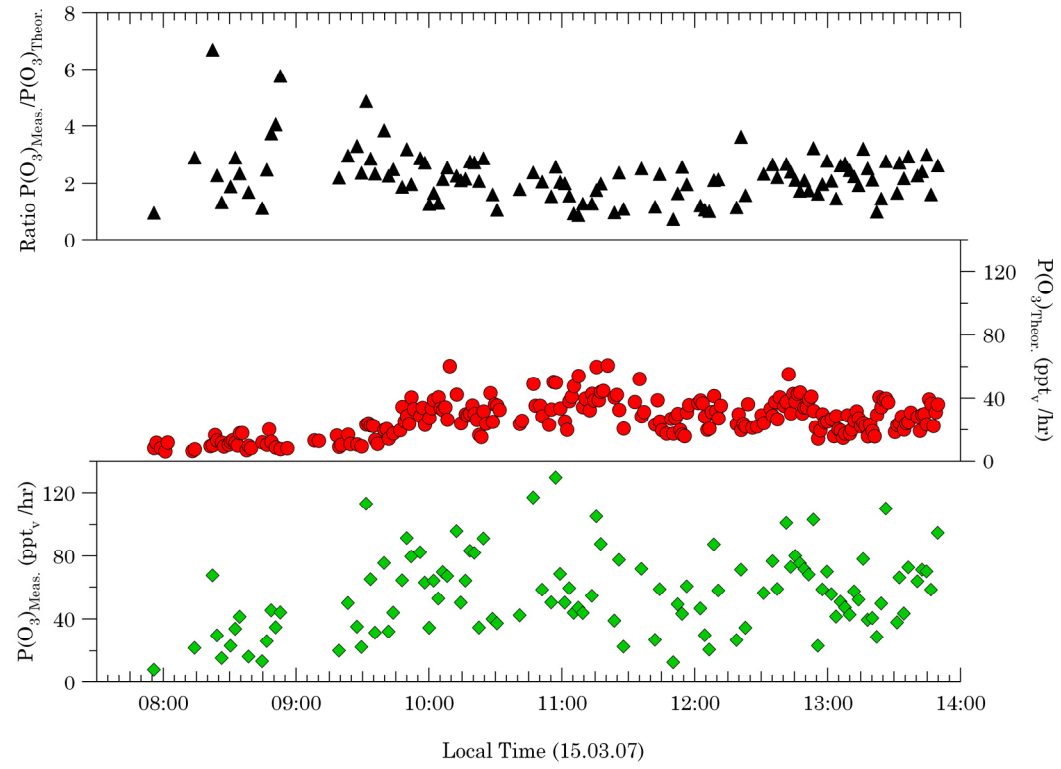

Figure 5.7 Comparison between $P(O_3)$ calculated from the measured data (green diamonds) and the $P(O_3)$ derived from the theoretical RO_2 (red circles), the ratio is presented as black triangles for March 15th.

A higher potential is seen in terms of ozone loss on March 15th in figure 5.6 in comparison to previous days. This is most likely due to higher $JO(^1D)$ intensity, increase in temperature and higher water vapour concentrations, as the ship heads northwards and further away from the colder regions of the southern Atlantic Ocean. The average $L(O_3)$ was 154.0 ppt_v/hr and maximum loss took place around noon at a rate of 251.0 ppt_v/hr.

The $P(O_3)$ calculated from both PERCA derived RO_2 data and also from assumed RO_2 concentrations are plotted in figure 5.7. The ratio is on average 2.23 with a maximum value of 6.68.

The $T(O_3)$ calculated using the $P(O_3)_{Meas.}$ is negative and it is concluded that the trend in the remote MBL on March 15th is O_3 destruction, with the average tendency at -100.5 ppt_v/hr (see figure 5.6). The $T(O_3)$ calculated using the $P(O_3)_{Theor.}$ is on average -127.4 ppt_v/hr and is slightly higher than the $T(O_3)$ calculated using the measured RO_2 to calculate $P(O_3)$ (not shown here).

March 16th exhibits the highest O_3 loss rates compared to previous days (figure 5.8), with average values at 282.3 ppt_v/hr. Maximum $L(O_3)$ was at a rate of 425.9 ppt_v/hr.

Again the $P(O_3)$ in this study was calculated twice using both PERCA derived RO_2 data and also using the assumed RO_2 concentrations. The results are presented in figure 5.9. The ratio is on average 3.52 with a maximum value of 7.49.

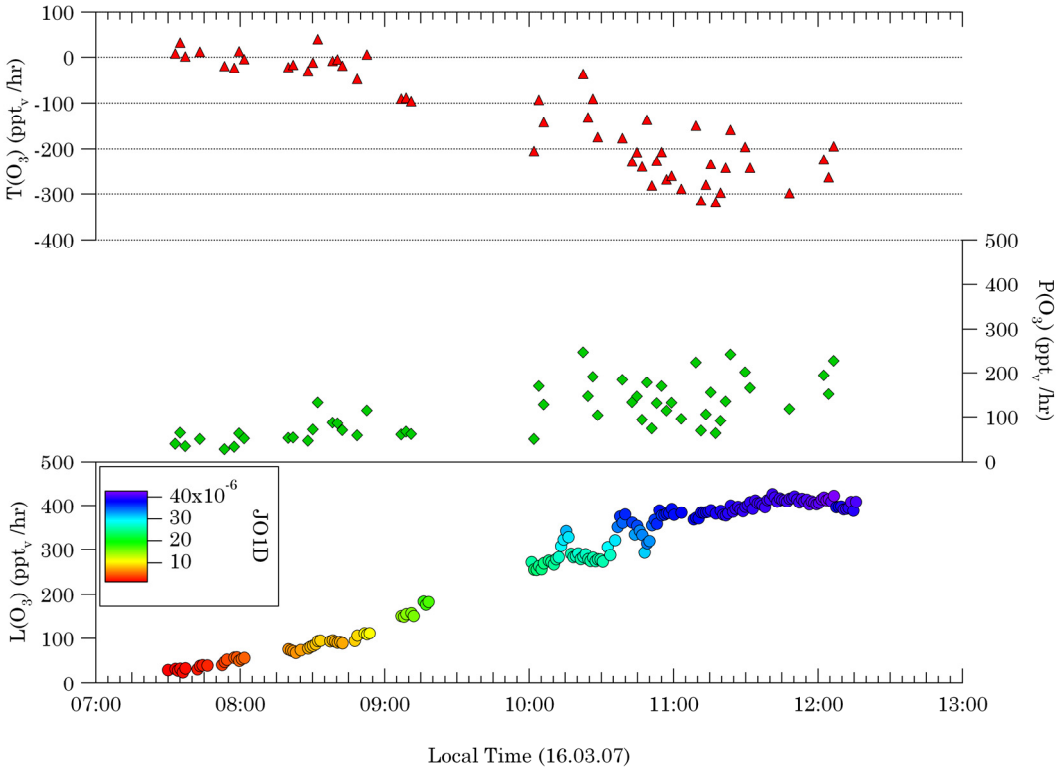

Figure 5.8 One-minute averages of the calculated $L(O_3)$, $P(O_3)$ and $T(O_3)$ in the clean background air masses on March 16th (ppt_v/hr). The colour bar in the $L(O_3)$ section of the graph represents the $JO(^1D)$ intensity (unit is s^{-1}). The $P(O_3)$ and $T(O_3)$ values in this plot were calculated using PERCA data.

From the $T(O_3)$ calculated using the $P(O_3)_{Meas.}$ it is concluded that the trend in the remote MBL on March 16th is O_3 destruction, with the average $T(O_3)$ at -135.8

ppt_v/hr (see figure 5.8). The $T(O_3)$ calculated using the $P(O_3)_{Theor.}$ is on average -237.6 ppt_v/hr and is significantly higher than the $T(O_3)$ calculated using the measured RO_2 to calculate $P(O_3)$.

The comparison of calculated $L(O_3)$, $P(O_3)$ and $T(O_3)$ for March 13th to 16th leads to the conclusion that whilst all days exhibited tendencies towards net ozone destruction, with the change in the longitude and latitude from (4.2°W, 51°S) on March 13th to (16.5°E, 39.8°S) on March 16th a significant increase in both $L(O_3)$ and $P(O_3)$ and the overall ozone destruction tendency can be observed.

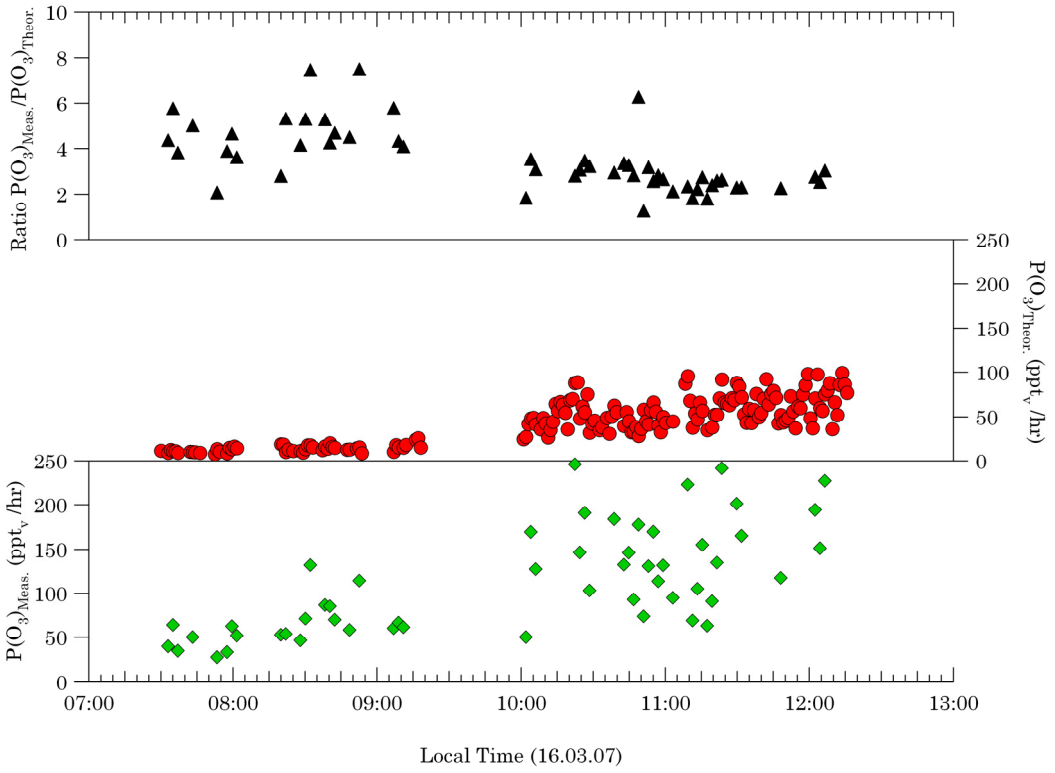

Figure 5.9 Comparison between $P(O_3)$ calculated from the measured data (green diamonds) and the $P(O_3)$ derived from the theoretical RO_2 (red circles), the ratio is presented as black triangles for March 16th.

5.1.3 Ozone Production based on the PSS expression

Another method which can be used to estimate ozone production in addition to the measured peroxy radical method presented in the last section is via the photostationary state expression (PSS explained in Chapter one in detail) (Volz-Thomas et al., 1996). Based on the following reactions:

$$NO_2 + h\nu \rightarrow NO + O(^3P) \qquad (\lambda<424\ nm) \qquad (R5.11)$$

$$O(^3P) + O_2 + M \rightarrow O_3 + M \qquad (R5.12)$$

$$O_3 + NO \rightarrow NO_2 + O_2 \qquad (R5.13)$$

and based on the assumption that only O_3 and peroxy radicals oxidize NO to NO_2 then:

$$JNO_2[NO_2] = \{k_{13}[O_3] + k_7[HO_2] + k_8[RO_2]\}[NO] \quad \text{(Equation 5.7)}$$

where k_7, k_8 and k_{13} are the reaction rate of reactions 5.7, 5.8 and 5.13. Equation 5.7 can be rearranged to give:

$$JNO_2[NO_2] - k_{13}[NO][O_3] = \{k_7[HO_2] + k_8[RO_2]\}[NO] \quad \text{(Equation 5.8)}$$

The right hand side of equation 5.8 is equal to $P(O_3)$, therefore it can be concluded that:

$$P(O_3) = JNO_2[NO_2] - k_{13}[NO][O_3] \quad \text{(Equation 5.9)}$$

Therefore, the formation rate of O_3, $P(O_3)$, can either be determined through the measurement of peroxy radical and NO concentrations (equation 5.3) or from the difference between the photolysis rate of NO_2 and the rate of the reaction between NO and O_3. Through the second method the measurement of the photolysis rate of NO_2 (JNO_2) can be utilized to determine the rate of O_3 production $P(O_3)$ from the PSS of NOx. Figure 5.10 shows the O_3 production time series calculated by the two distinct methods, Equation 5.3 and 5.9, for this experiment.

Values for each day are averages over daylight hours in the clean background conditions of the MBL. $P(O_3)$ calculated using the measured peroxy radicals is represented as blue circles and $P(O_3)$ calculated using the PSS expression is represented as red diamonds. Due to the lack of ROx data for March 13th, equation 5.3 has been calculated based on the $[HO_2] = [RO_2]$ assumption.

As can be observed in figure 5.11 the level of correlation between the two calculations is very good (R^2=0.92). However, the $P(O_3)$ values derived from the PSS method are between 2 to 3 times larger on average than those calculated from peroxy data. This is not unexpected considering the interesting results obtained from the PSS calculations in Chapter four.

These results are also in agreement with those in a study by Salisbury et al. where it was found that the average O_3 tendency calculated from the PSS method was on average three times larger than those calculated from peroxy radical (Salisbury et al., 2002). A similar result was also obtained by Carpenter et al. where PSS calculations were used to predict peroxy radical mixing ratios and compared with results from a box model (Carpenter et al., 1998). The peroxy radical levels predicted from PSS expression were found to be two orders of magnitude higher than the modeled mixing ratios. Cantrell et al. also found that peroxy radical mixing ratios estimated from the PSS expression exceeded measured levels by a factor of two (Cantrell et al., 1997).Whilst the above figures present a qualitative agreement, the fact that PSS derived estimates are on average about two to three times higher than those derived from peroxy radicals is evident in figure 5.12. The one minute $P(O_3)$ data derived from both methods shows clearly the difference in $P(O_3)$ calculated from the measured data (blue circles) and the $P(O_3)$ derived from the PSS expression (red diamonds) for March 14th, 15th and 16th.

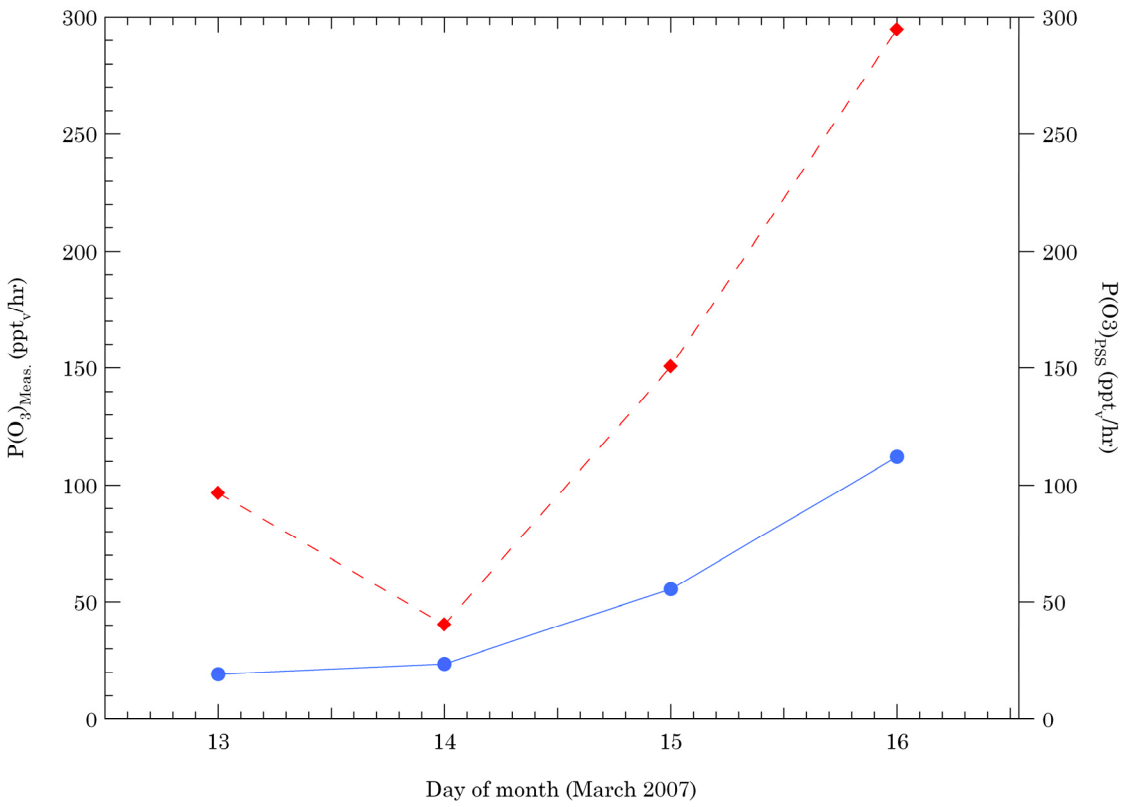

Figure 5.10 Time series of daytime average $P(O_3)$. Blue circle and red diamonds represent the values obtained from measured data and the PSS expression respectively. Units are ppt_v/hr.

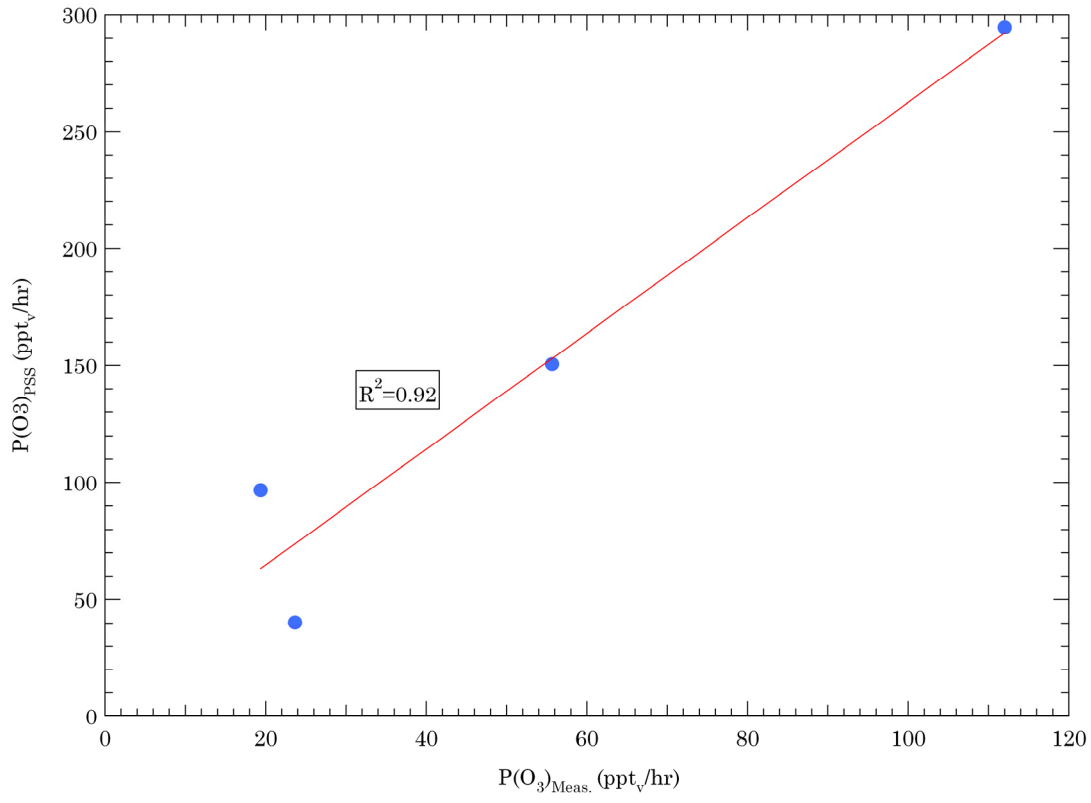

Figure 5.11 Plot of the average daytime mean ozone production values.

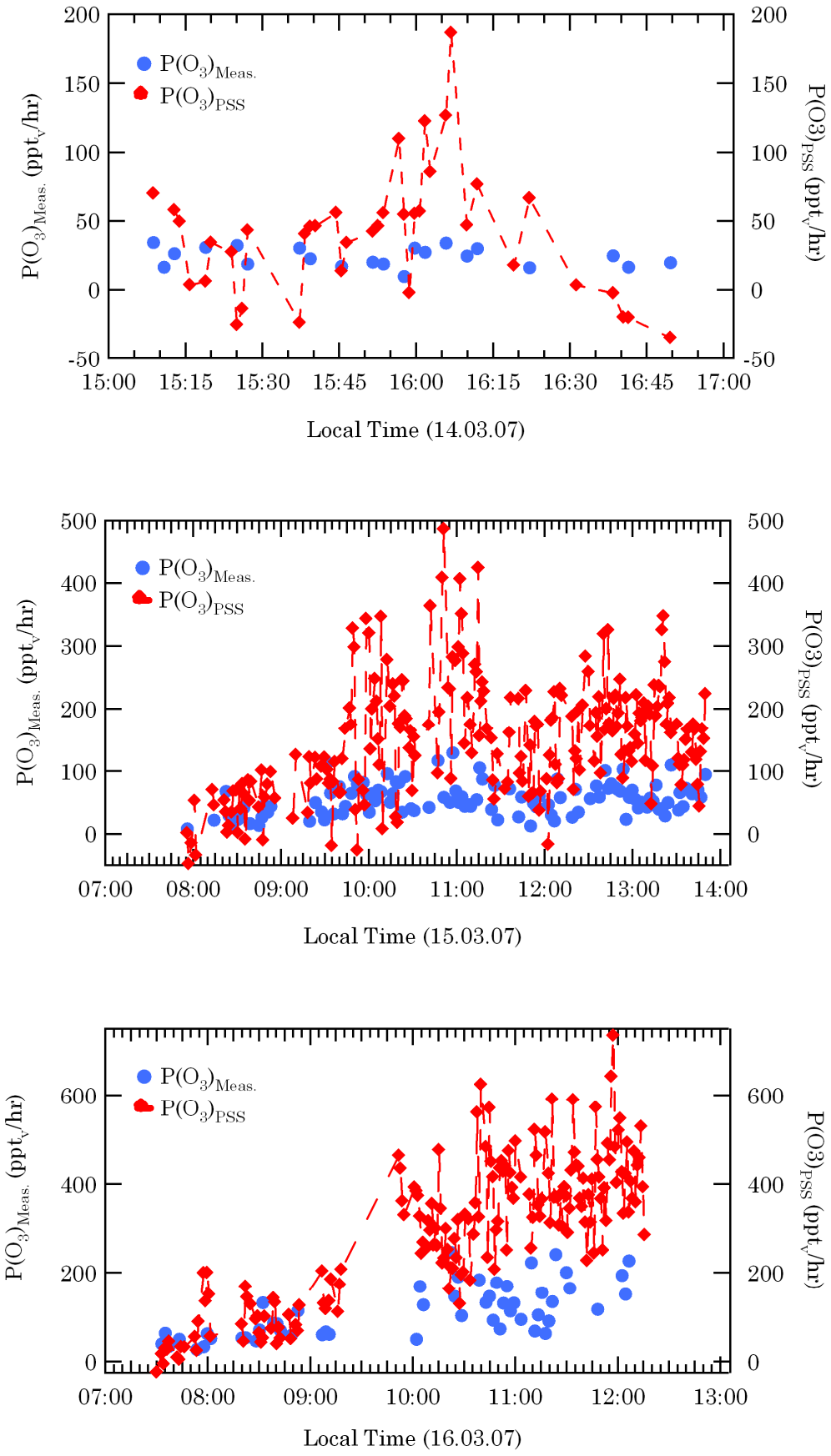

Figure 5.12 Time series of 1-minute averaged $P(O_3)$. Blue circle and red diamonds represent the values obtained from measured data and the PSS expression respectively. Units are ppt_v/hr.

5.1.4 Ozone Compensation Point

The ozone compensation point (OCP) is a topic of major importance to the tropospheric O_3 budget and is strongly dependant on NO concentrations. It is also defined as the critical NO level which is the point where photochemical O_3 destruction and production processes are exactly in balance. In a low NOx regime OCP is controlled by the rate of O_3 destruction (R5.1 and R5.2) and also by the self reaction of peroxy radicals with themselves (R5.5 and R5.6). Since O_3 destruction and production processes are in balance therefore:

$$P(O_3) = L(O_3)$$

When equations 5.3 and 5.4 are placed on either side of the equal sign, and re-arranged, the critical NO concentration ($[NO]_{crit.}$) can be obtained through:

$$[NO]_{crit.} = \frac{k_3[HO_2][O_3]+JO(^1D)[O_3]\alpha + k_4[OH][O_3]}{k_7[HO_2]+k_8[RO_2]} \qquad \text{(Equation 5.10)}$$

Presented in figures 5.13 to 5.16 are the time series of 1-minute averaged critical NO mixing ratios derived from both theoretical and measured peroxy radicals. The colour bars indicate the $JO(^1D)$ intensity on each day. The average $NO_{crit.}$ mixing ratios, standard deviation (STDEV), minimum and maximum mixing ratios for March 14th to 16th are presented in table 5.2.

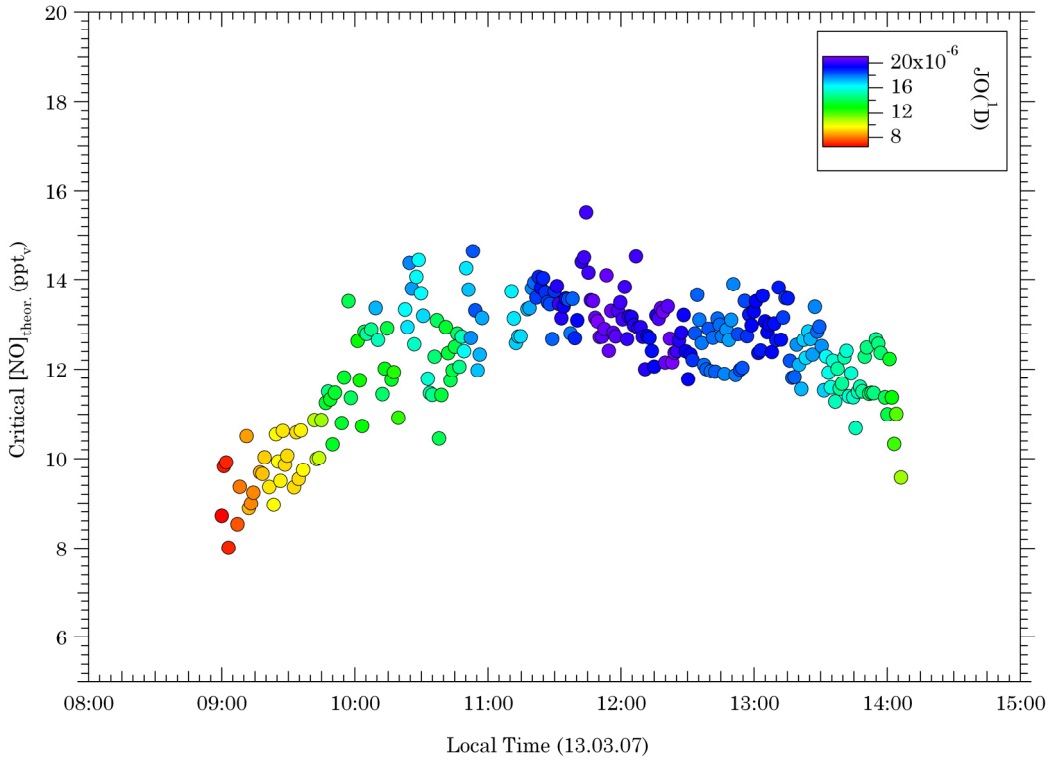

Figure 5.13 Time series of 1-min averaged $NO_{crit.}$ mixing ratios derived from assumed $[RO_2]$ on March 13th. The colour bar indicates the $JO(^1D)$ intensity.

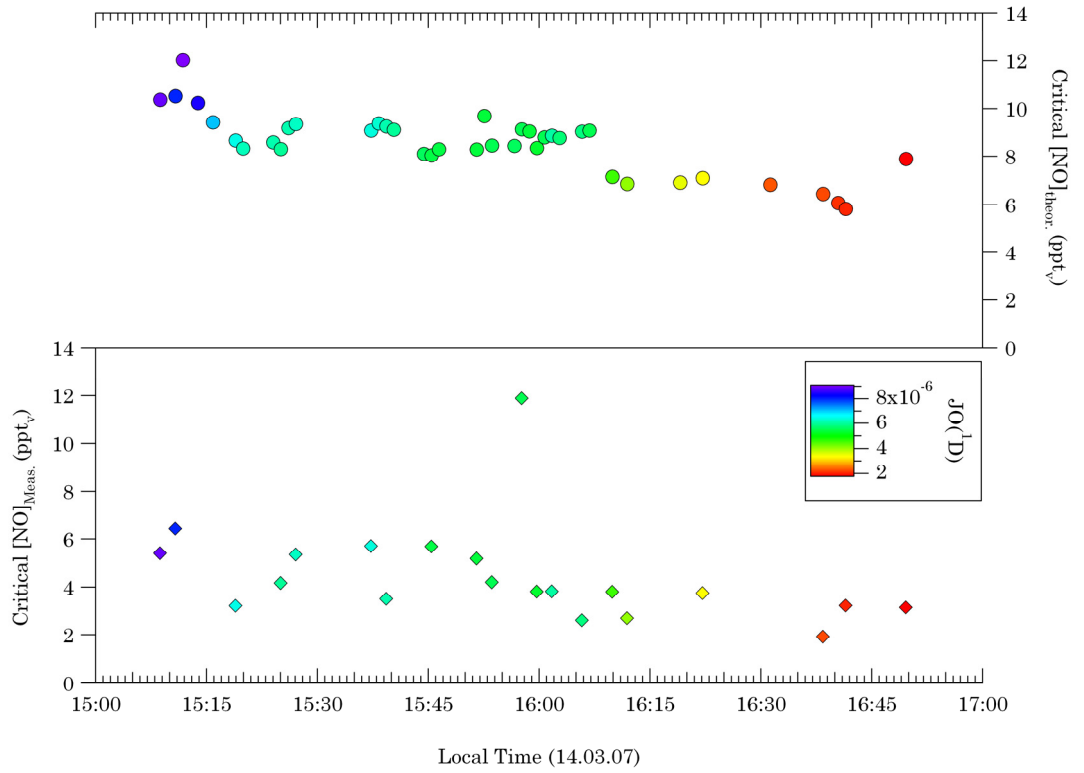

Figure 5.14 Time series of 1-min averaged $NO_{crit.}$ mixing ratios on March 14th. Circles and diamonds represent $NO_{crit.}$ derived from assumed $[RO_2]$ and measured PERCA data respectively.

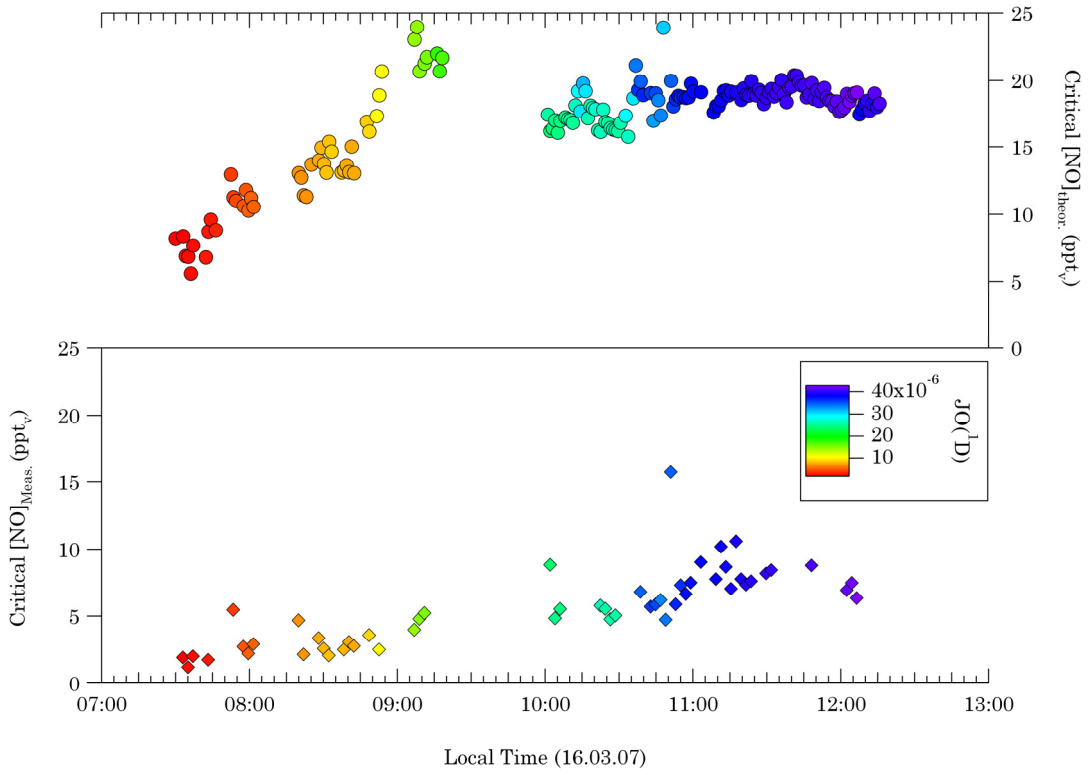

Figure 5.15 Time series of 1-min averaged $NO_{crit.}$ mixing ratios on March 15th. Circles and diamonds represent $NO_{crit.}$ derived from assumed $[RO_2]$ and measured PERCA data respectively.

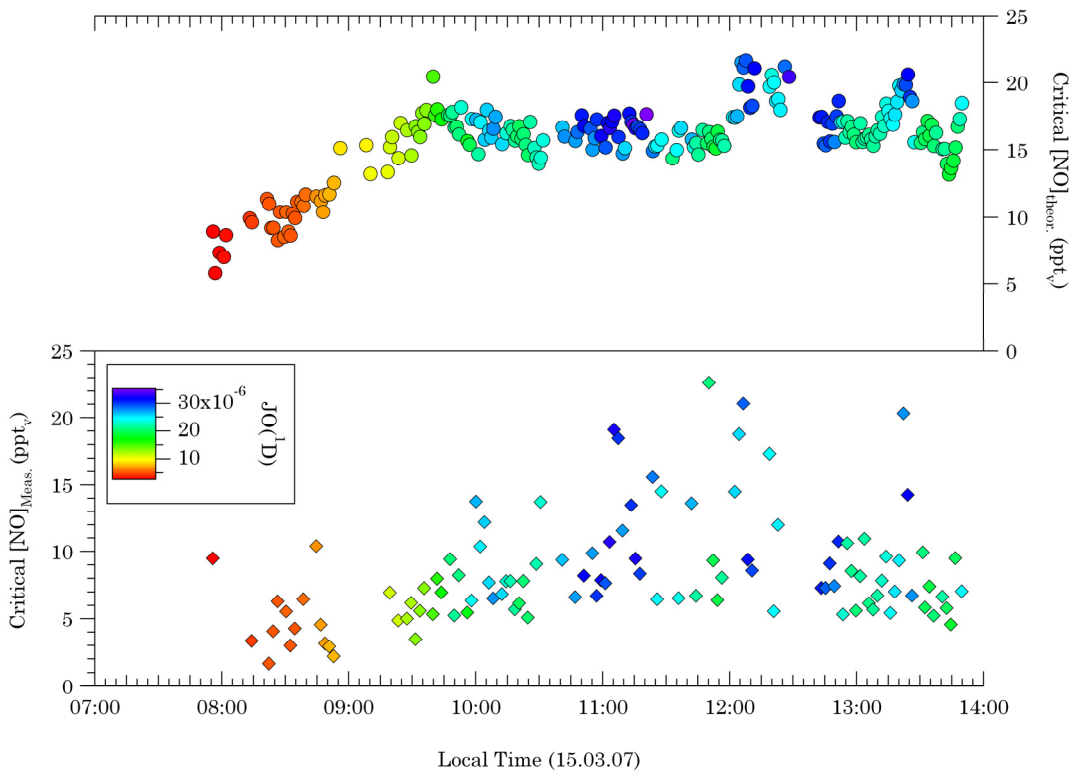

Figure 5.16 Time series of 1-min averaged $NO_{crit.}$ mixing ratios on March 16th. Circles and diamonds represent $NO_{crit.}$ derived from assumed $[RO_2]$ and measured PERCA data respectively. The colour bar indicates the $JO(^1D)$ intensity.

Table 5.2 Average $NO_{crit.}$ values calculated from PERCA data

Day	NO (ppt_v)	O_3 (ppb_v)	AVG. Measured $NO_{crit.}$ (ppt_v)	STDEV (ppt_v)	Min. Measured $NO_{crit.}$ (ppt_v)	Max. Measured $NO_{crit.}$ (ppt_v)
March 14	2.14	21.26	4.47	2.11	1.91	11.87
March 15	2.75	17.96	8.46	4.11	1.65	22.6
March 16	2.76	18.96	5.61	2.8	1.18	15.71

Table 5.3 presents $NO_{crit.}$ mixing ratios which are calculated using the theoretically derived $[RO_2]$ based on the assumption that $[RO_2]=[HO_2]$. The $NO_{crit.}$ calculated from assumed RO_2 values are higher by a factor of approximately 2 on March 14th and 15th and by a factor of 3 on March 16th compared to those calculated using the actual measured ROx data in table 5.2. Again this reflects our difficulty in understanding the peroxy radical budget in the remote MBL.

The OCP values obtained here are lower than the values obtained in previous studies. Minimum values are at approximately 2 ppt_v of NO and are on average between ca. 5 ppt_v to 9 ppt_v based on the measured parameters. Carpenter et al. calculated an OCP value of 23 ± 20 ppt_v of NO for Cape Grim which is basically the same as the maximum value of 22.6 ppt_v of NO calculated in our study (see table 5.2) (Carpenter et al., 1997).

Table 5.3 Average $NO_{crit.}$ values calculated from theoretically assumed RO_2 values

Day	NO (ppt_v)	O_3 (ppb_v)	AVG. Assumed $NO_{crit.}$ (ppt_v)	STDEV (ppt_v)	Min. Assumed $NO_{crit.}$ (ppt_v)	Max. Assumed $NO_{crit.}$ (ppt_v)
March 13	3.1	20.38	12.30	1.29	8.01	15.51
March 14	2.14	21.26	8.55	1.26	5.82	12.02
March 15	2.75	17.96	15.77	2.84	5.80	21.65
March 16	2.76	18.96	17.23	3.69	5.58	29.65

In a separate study by Salisbury et al. the OCP was calculated at a lower value of 14ppt_v NO (Salisbury et al., 2002). However, it must be taken into account that the OCP is highly specific to a given set of conditions, particularly $J(O^1D)$, $[O_3]$ and $[H_2O]$ which are the key players in terms of influence on photochemical O_3 loss. The level of NO required to reach and exceed the balance point between net loss and production is strongly influenced by these variables.

5.3 Summary and Conclusions

The measured data obtained during MD160 clearly demonstrate that under remote marine boundary layer conditions, net photochemical destruction of O_3 occurs during the austral summer. This is demonstrated in the anti-correlation of O_3 and the peroxy radicals during the daytime hours. It is also confirmed separately through the observed linear correlation between peroxy radicals and $\sqrt{JO(^1D)}$. Also as the research vessel crossed from the colder remote south-western regions to the warmer north-eastern regions of the southern Atlantic an increase in the net ozone destruction was clearly seen.

Calculation of O_3 production using both in-situ peroxy radical measurements and the deviation from photochemical stationary state PSS gave qualitative agreement. However, the PSS derived $P(O_3)$ were about three times higher on average than those derived from measurements. This result is in agreement with a series of previous investigations e.g. (Salisbury et al., 2002).

The critical NO level or OCP in the remote MBL was estimated to be on average between 5 to 9 ppt_v of NO based on the measured parameters. These values are considerably lower than the values suggested by previous studies carried out in a variety of locations. The lower OCP may lead to the conclusion that the ozone production/destruction potential of the remote southern Atlantic Ocean is more responsive to the availability of NO in comparison to other environments.

Even though the above results provide confidence that the level of understanding of the photochemistry of O_3 in the remote MBL has made advancements to some extent, from a mechanistic aspect, there remains the important question concerning gas phase chemical processes that is namely halogen chemistry as well as physical removal processes and heterogeneous chemical reactions. Due to the mentioned deficiencies and also due to the absence of comprehensive O_3 precursor databases our assessment of tropospheric O_3 in terms of photochemical processes and the general O_3 budget is still in need of intensive future investigation.

Chapter 6: Comparison of observed data with EMAC model output

6.1 Introduction

The accurate measurement of trace gases over the ocean provides a particularly useful approach to assess the accuracy of atmospheric chemical models, because the simple dynamics and the lack of anthropogenic emissions reduce the number of physicochemical processes required to describe and interpret the results. Therefore, in order to achieve a direct comparison of measurement data with model output an atmospheric chemistry general circulation model was used in this study to simulate concentrations of trace gases along the exact MD 160 cruise track.

The ECHAM/MESSy Atmospheric Chemistry (EMAC) model is a numerical chemistry and climate simulation system that includes sub-models describing tropospheric and middle atmosphere processes and their interaction with oceans, land and human influences (Joeckel et al., 2006). It uses Modular Earth Sub-model System (MESSy) to link multi-institutional computer codes. The core atmospheric model is the 5th generation European Centre Hamburg general circulation model (ECHAM5) (Roeckner et al., 2006). For the present study EMAC was applied in the T42L90MA-resolution, i.e. with a spherical truncation of T42 (corresponding to a quadratic Gaussian grid of approx. 2.8° by 2.8° in latitude and longitude) with 90 vertical hybrid pressure levels up to 0.01 hPa. The model time step in this resolution is 12 minutes. Data was archived every 5 hours simulation time; along the MD160 transects, data from the model were directly sampled at model time step resolution.

6.2 Results and discussion

Figure 6.1 to 6.4 illustrate the time series of clean background measurements (March 13th to 16th 2007) versus data from the EMAC model. All black data points are EMAC model data and measured data is represented in a variety of colours. NO, NO_2, O_3, HO_2 and RO_2 are represented by circles, diamonds, triangles, squares and bows respectively. The measured data is presented as 1 minute averaged mixing ratios whilst EMAC data is presented as 12 minute averages originally derived from the model.

It can be observed in figure 6.1 that both NO and NO_2 data from the EMAC model are approximately equal to the lowest mixing ratios measured by the instrument on March 13th. The HO_2 mixing ratio comparison reveals the best correlation for both data sets with average HO_2 mixing ratios at approximately 4 ppt_v (see table 6.1). Also the diurnal cycle for HO_2 is very well represented by EMAC and follows the measured data closely.

However, what is evident is that the EMAC model does not produce O_3 mixing ratios similar to those measured during the campaign. With the difference in the two data sets being on average 2.5 ppb_v, which indicates a 12 % difference. Noteworthy is the fact that the O_3 concentrations during the campaign where measured using two different techniques. Data presented in this work is measured using the chemiluminescence technique which has already been discussed in Chapter two.

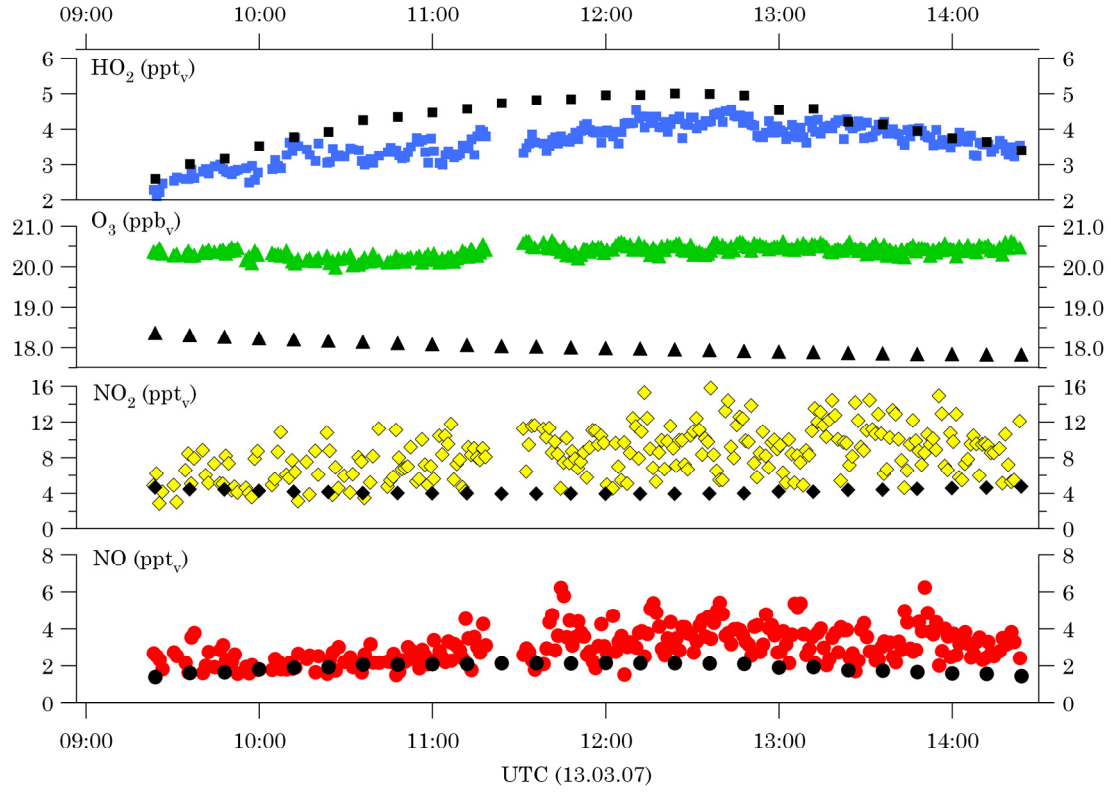

Figure 6.1 Time series of observed data versus EMAC data for March 13th.

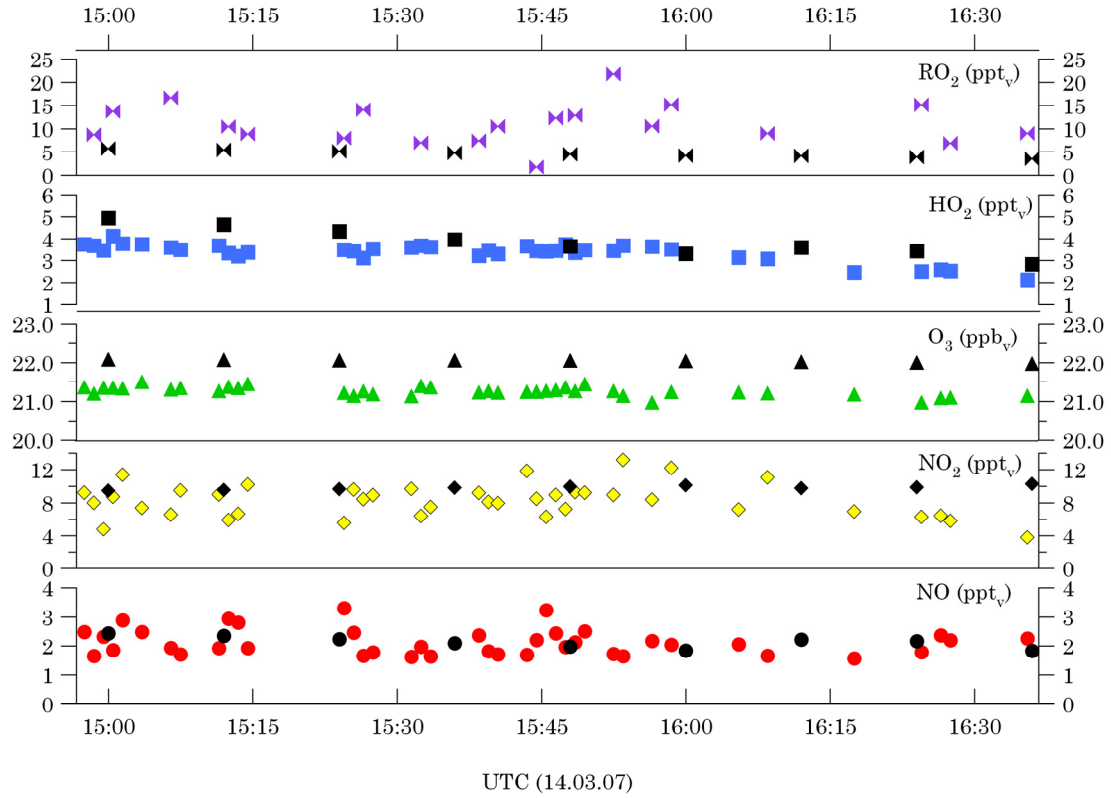

Figure 6.2 Time series of observed data versus EMAC data for March 14th.

Ozone was also measured during the campaign by a UV-absorption instrument (section 2.8, Chapter two). A comparison between the O_3 data measured via the two different methods revealed very good agreement. A comparison between modeled and observed data could not be made for RO_2 data as measured data was not available for this day. However, the average mixing ratio for the EMAC model is presented in table 6.1. STDEV stands for standard deviation in the tables below.

Table 6.1 Average mixing ratios of trace gases for measured and modeled data on March 13th

	March 13th	Average	STDEV
NO	Measured	3.1	(±0.94)
	Modeled	1.9	(±0.24)
NO_2	Measured	8.42	(±2.69)
	Modeled	4.18	(±0.26)
O_3	Measured	20.38	(±0.14)
	Modeled	18.02	(±0.16)
HO_2	Measured	3.67	(±0.50)
	Modeled	4.2	(±0.68)
RO_2	Measured	-	-
	Modeled	4.84	(±0.71)

Figure 6.2 presents the times series of observed and EMAC data for March 14th. As can be observed from averaged values NO and NO_2 data from modeled and measured datasets are excellent (see table 6.2). On this day modeled O_3 is also in fairly good agreement with measured values. However, this is the only period where an agreement is observed which may be due to the low JO(^{1}D) observed on this day. It could be speculated that the JO(^{1}D) and therefore the ozone destruction term in the model have not been correctly accounted for and this leads to the much higher O_3 mixing ratios especially with the change in longitude and latitude from (4.2°W, 51°S) on March 13th to (16.5°E, 39.8°S) on March 16th, where an increase in temperature, JO(^{1}D) and Ozone destruction was observed as discussed in Chapter five.

Table 6.2 Average mixing ratios of trace gases for measured and modeled data on March 14th

	March 14th	Average	STDEV
NO	Measured	2.14	(±0.46)
	Modeled	2.18	(±0.25)
NO_2	Measured	8.36	(±2.12)
	Modeled	9.77	(±0.30)
O_3	Measured	21.26	(±0.12)
	Modeled	22.05	(±0.04)
HO_2	Measured	3.39	(±0.42)
	Modeled	4.00	(±0.80)
RO_2	Measured	10.99	(±4.26)
	Modeled	4.74	(±0.82)

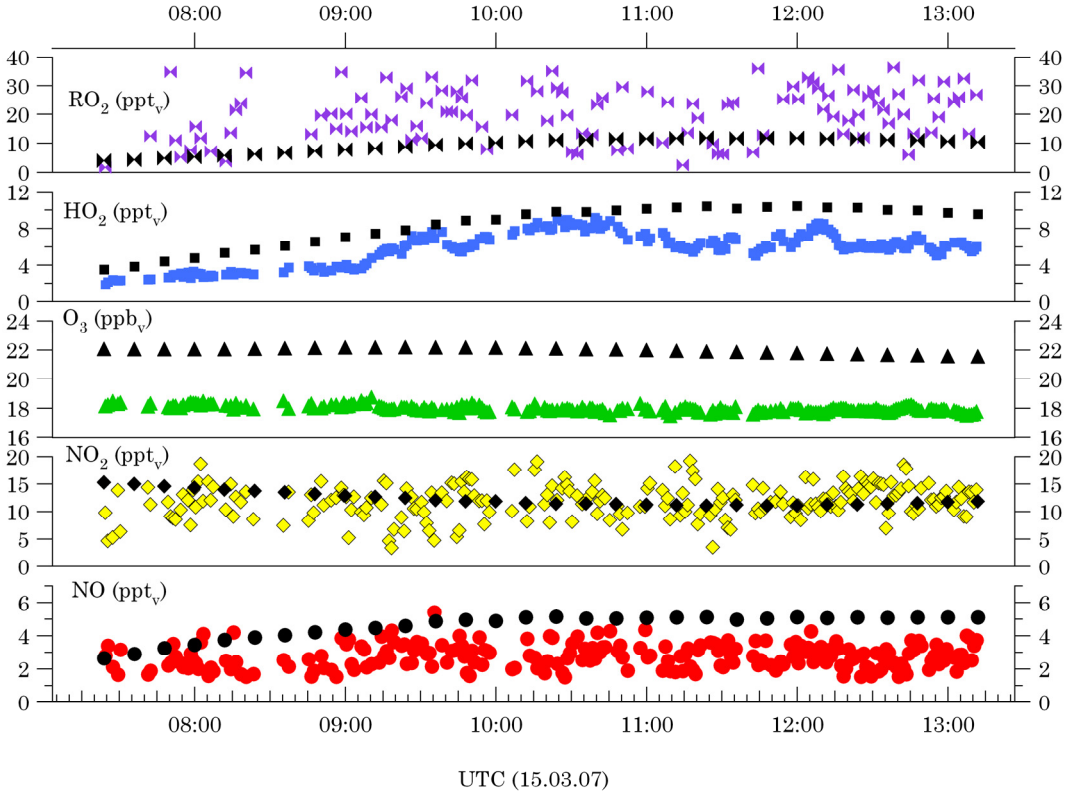

Figure 6.3 Time series of observed data versus EMAC data for March 15th.

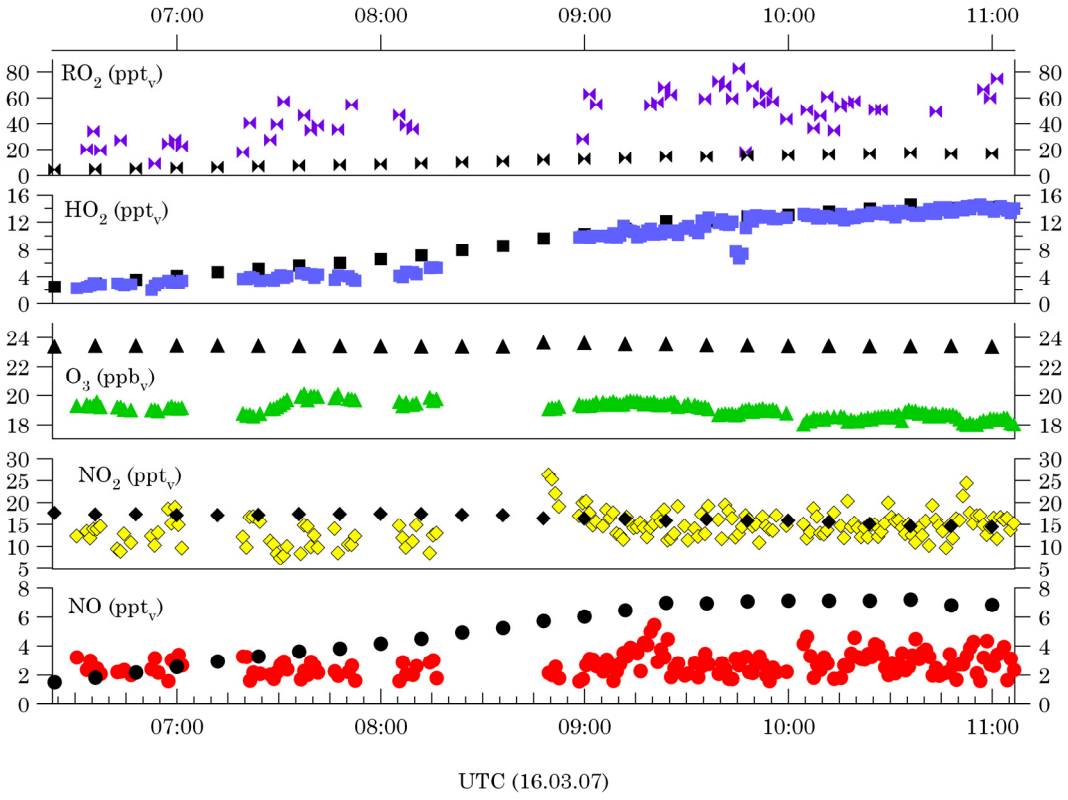

Figure 6.4 Time series of observed data versus EMAC data for March 16th.

Comparison of HO_2 data also shows very good agreement. However, the comparison of RO_2 data reveals that measured values (11 ppt_v) are on average more than double the modeled mixing ratios (4.74 ppt_v). At this point in the investigation this result is not completely unexpected as the PSS calculations in Chapter four revealed that there were major differences between measured and PSS derived peroxy radical concentrations.

Figure 6.3 reveals excellent agreement between the measured and model NO_2 data sets on March 15th. A difference is seen in the NO data with modeled data being almost double the measured values especially as the day progresses. This is opposite to the trend seen on March 13th, where the measured data was slightly higher than the modeled mixing ratios. A look at the O_3 data reveals that the model predicts higher mixing ratios, on average 4ppb_v in comparison to the actual measured O_3 values. The HO_2 calculated by the model is on average 25 % higher than measured mixing ratios.

A significant difference is seen between modeled and PERCA derived RO2 values, with average EMAC values being more than 50 % higher than measured mixing ratios. Again this is similar to results of a comparison made between measured RO_2 data and PSS derived data calculated in Chapter four.

Table 6.3 Average mixing ratios of trace gases for measured and modeled data on March 15th

	March 14th	Average	STDEV
NO	Measured	2.76	(±0.73)
	Modeled	4.58	(±0.73)
NO_2	Measured	11.83	(±3.01)
	Modeled	12.27	(±1.30)
O_3	Measured	17.96	(±0.22)
	Modeled	21.96	(±0.20)
HO_2	Measured	5.91	(±1.73)
	Modeled	8.31	(±2.25)
RO_2	Measured	20.25	(±8.90)
	Modeled	9.28	(±2.59)

The results for March 16th show that there is very good agreement between measured and modeled NO_2 data. Again the NO mixing ratios derived from the model are higher than measured values and this difference get larger towards noon. The difference between measured and modeled O_3 mixing ratios is highest on this day compared to previous days. Modeled O_3 data are on average approximately 20 % higher than measured mixing ratios. Comparison of HO_2 data however shows excellent agreement between the two data sets with the modeled values following the measured HO_2 data very closely (see figure 6.4). Comparison of RO_2 data shows that measured data is again significantly higher than modeled data, with measured mixing ratios being on average four times greater than EMAC data. This is not unexpected considering the results obtained from the PSS calculations in Chapter four.

Table 6.4 Average mixing ratios of trace gases for measured and modeled data on March 16th

	March 14th	Average	STDEV
NO	Measured	2.76	(±0.79)
	Modeled	5.14	(±1.94)
NO_2	Measured	14.41	(±3.24)
	Modeled	16.31	(±1.05)
O_3	Measured	18.96	(±0.53)
	Modeled	23.43	(±0.08)
HO_2	Measured	9.8	(±4.16)
	Modeled	9.19	(±4.11)
RO_2	Measured	46.65	(±17.01)
	Modeled	11.25	(±4.49)

6.3 Summary and Conclusions

The comparison between the observed and EMAC model data demonstrates very good agreement with regard to short lived species such as NO and HO_2. However, a difference is seen between the two data sets for longer lived species, in this case O_3 specifically.

It is also worth mentioning that the model runs were carried out with the halogen chemistry turned off. However, this seems to have little impact on the outcome of the data in general, as the model and measured values are in relatively good agreement especially in regard to short lived species. It can be speculated that the discrepancy seen in O_3 data may be a result of missing halogen chemistry. Halogen chemistry would result in lower O_3 concentrations in the model thus improving the comparison with observations.

HO_2 concentrations predicted by the model were in very good agreement with measured HO_2 concentrations. However, RO_2 concentrations from the two data sets demonstrated significant differences. This was not an unanticipated result as the PERCA signal was a great deal higher than expected as discussed in detail in previous chapters (section 4.2.5 of chapter four). The EMAC data is in fact in agreement with data derived from steady state box model results, the CO/CH_4 ratio and also results of previous studies. This again may indicate that the additional signal measured by the PERCA instrument is created by an oxidant other than peroxy radicals.

Chapter 7: Summary, Conclusions and Outlook

The role of in-situ photochemistry in the Tropospheric ozone budget has become an important research topic in atmospheric chemistry in recent years. Atmospheric photochemistry produces a variety of radicals which exert a substantial influence on the composition of the atmosphere. In order to be able to estimate feedbacks on future climate scenarios it is crucial to determine current global budgets as precisely as possible.

The trace gas composition of the marine boundary layer of the remote southern Ocean can be considered as one of the most atmospherically pristine areas on Earth. In order to investigate the photostationary state of nitrogen oxides and ozone, comprehensive ship-born measurements of trace gases, aerosols and meteorological parameters were made while crossing the South Atlantic Ocean from Chile (70.85°W, 53.12°S) to La Reunion island (55.36°E, 21.06°S) in the late Austral summer of 2007. Excellent data have been obtained for all relevant compounds in the remote South Atlantic Ocean.

In this study all parameters which are believed to be required in order to comprehensively investigate the PSS of NOx and O_3 in the remote MBL have been measured. This makes this study unique in the sense that a complete set of measurements have been obtained in the pristine MBL, without the effect of anthropogenic pollution whatsoever. The use of high resolution, state of the art instruments with very low detection limits has allowed us to obtain a data set which is apt for studying the PSS in the remote MBL. The data were of sufficient quantity to be able to verify aspects of the basic theory of photochemistry occurring in the troposphere.

It is important to note that the main difference between this study and previous studies is that this study was done in the remote open ocean, where there is almost no influence from local pollution which is seen in continental and coastal regions of the globe. In order to avoid the possibility that results might be skewed by either local sources of pollution or other regional effects, ship born studies on the open ocean are essential. Noteworthy are the extremely low mixing ratios observed for both NOx and the volatile organic species such as acetone (727 ppt_v) and carbon monoxide (41 ppb_v). In particular, NOx was measured on average at approximately 10 ppt_v in the remote marine air. Such values are considerably lower than those measured at terrestrial surface sites, even at remote locations such as Antarctica (Grannas et al., 2007).

In Chapter four the PSS parameter (Leighton ratio) was calculated using observed data of NO, NO_2, O_3, HO_2, ROx and JNO_2. The PSS calculations were carried out using all data available for three specific regimes; Pristine background conditions (NOx <30 ppt_v), South African air masses (100 ppt_v < NOx < 500 ppt_v) and a period in the remote MBL during the isolated incident of a passing ship which was on collision course with the Marion Dufresne (1 ppb_v < NOx < 2 ppb_v). The latter two periods were studied with the sole purpose of comparison with the pristine background conditions.

The most important finding of this investigation was that the Leighton ratio can be valid at very low NOx concentrations in the remote MBL. Significant deviations from unity are seen once there is a significant increase in JNO_2 intensities (Φ>1). Therefore, the deviation from unity is not at minimum NOx concentrations and JNO_2 values as suggested in previous theoretical studies. This result may be an indication of

additional unknown photochemistry taking place at higher JNO_2 values in the low NOx regime of the remote MBL. That is an additional unknown photochemically driven reaction which may not be significant once NOx concentrations are relatively high but can exert influence on the PSS of O_3 in the remote pristine conditions of the MBL which compromise up to 25% of the total atmosphere. This affect would be similar to the affect of peroxy radicals on the PSS of O_3 and NOx. In the mid-range NOx regime (150 ppt_v) and below the addition of HO_2 and RO_2 is important. With the decrease in NOx concentrations RO_2 and HO_2 chemistry gains more importance. However, once NOx ratios reach a certain concentration the affect of peroxy radicals is deemed insignificant. It is believed that high NOx levels suppress peroxy radical concentrations; therefore, these radicals can not cause deviations in the Leighton ratio. Clearly the trend seen in the pristine background section of figure 4.18 is interesting in the sense that at low NOx levels there is possibly an unknown photochemically driven process which is of insignificance at NOx mixing ratios above 100 ppt_v.

Measurements of pollution from a ship on collision course with our ship in the remote South Atlantic leads to the conclusion that PSS can be established in a matter of minutes once large concentrations of NOx are released into the remote southern Atlantic. It was found that during high NOx periods (1.5 ppb_v) PSS is established without taking into account the effect of peroxy radicals. This is a strong confirmation of the insignificance of ROx reactions in high NOx regimes.

In order to better understand the significance of the Leighton ratio deviations, theoretically calculated NO_2, which can be derived from the PSS expression, were compared to observed NO_2 concentrations for the pristine background conditions of the MBL. The comparison was made in the form of a ratio between the two values. The ratio between the measured and theoretically calculated NO_2 would be expected to equal unity if indeed these two values were similar. In fact at the deviation point maxima, NO_2 observations are on average a factor of 7 higher than the theoretically calculated NO_2 values. This clearly indicates the role of a chemical process which converts additional NO to NO_2. The maximum deviations were correlated to periods with the highest JNO_2 intensity. The periods with relatively low JNO_2 intensities were the periods were the ratio approached unity. It was observed that the uncertainty limits are insufficient to explain the discrepancy seen between observed and theoretically calculated NO_2 concentrations.

In the past combined field and modeling investigations of the peroxy radical budget and of ozone formation have been undertaken to test the current understanding of photochemistry. Generally, it was found that RO_2 concentrations calculated from assuming PSS were significantly higher than observed values.

It was observed from measurements that the HO_2 and OH mixing ratios were very low, as would be expected in the remote MBL of the southern Atlantic. However, it was also observed that the ROx data obtained from the PERCA instrument was unexpectedly high. In order to further investigate the extremely large difference between the observed peroxy radical concentrations the issue was examined from several different aspects using a variety of observations, models and calculations. The comparison between measured and model calculated ROx concentrations in this study (low NOx regime) shows that the theory failed to reproduce the observation. This indicates that species convert NO to NO_2 in excess of the reaction between NO with O_3 and the peroxy radicals.

It is well known from previous studies that methods for estimating peroxy radical concentrations from other measured parameters do not agree with observations. This

could be due to systematic errors in the measured data used to calculate RO_2. A second possibility is that there is an unknown oxidant of NO which converts NO to NO_2 in excess of the reaction of NO with ROx. Results presented in sections 4.2.4.1 to 4.2.4.5 indicate that CH_3O_2 values in the remote MBL are expected to be more or less the same concentrations as HO_2. This is contradicted by the extremely high observed PERCA signals. However, at the same time the high PERCA signals seem to be in good agreement and a possible explanation for the high NO_2 to NO concentrations measured by the CLD instrument. In fact with the inclusion of the PERCA signal in the PSS ratio the deviations from PSS are decreased substantially to a minimum. However, it is deemed unlikely that CH_3O_2 (or RO_2 in general) concentrations are a factor of ten higher than HO_2 in the remote MBL. Therefore, in light of the evidence, presented in sections 4.2.4 the most likely explanation for the gross overestimation of the PERCA signal would be that the response of the instrument is not entirely due to the measurement of peroxy radicals. It is assumed a possibility that the additional signal in the PERCA instrument is created by an oxidant other than peroxy radicals.

In the past halogen monoxides, XO, have been proposed as potential candidates for the 'unknown oxidant' which can convert additional NO to NO_2. In order to explain the deviations in the Leighton ratio in this study XO mixing ratios of more than $15ppt_v$ would be required. This is difficult to imagine as O_3 concentrations are on average between 18 to 24 ppb_v during the period of this study. If indeed such high XO levels existed in the atmosphere outside the Polar Regions, O_3 levels would be approximately zero ppb_v. These high theoretically calculated XO mixing ratios do not match observations and model predictions which have been reported previously for the remote South Atlantic.

In previous studies the Leighton ratio has been used to estimate levels of NO, NO_2, O_3, HO_2 and RO_2. It is concluded from this study that in non-urban regions the ratio is affected by unknown chemistry which invalidates its common use as a way of deriving atmospheric trace gas concentrations. The PSS method therefore, must be used with the utmost caution, since it is only valid when PSS is reached and when the steady state NOx portioning is entirely dependant on O_3 and the peroxy radicals.

The measured data and results presented in Chapter five clearly demonstrate that under remote marine boundary layer conditions, net photochemical destruction of ozone occurs and that photolysis was found to be the primary cause of ozone destruction in daylight hours. This is demonstrated in the anti-correlation of O_3 and the peroxy radicals during the daytime hours. It is also confirmed separately through the observed linear correlation between peroxy radicals and $\sqrt{JO(^1D)}$. Also as the research vessel crossed from the colder remote south-western regions to the warmer north-eastern regions of the southern Atlantic an increase in the net ozone destruction was evidently seen. Therefore, the pristine background atmosphere can generally be considered a "buffer" against the anthropogenic production and enhancement of O_3 occurring in polluted regions of the globe. However, the capacity to buffer O_3 is destroyed once long range transport and release of NOx from reservoir species kick in e.g. as a result of direct anthropogenic emissions from ships.

Calculation of O_3 production using both in-situ peroxy radical measurements and the deviation from photochemical stationary state PSS gave qualitative agreement. However, the PSS derived $P(O_3)$ were about three times higher on average than those derived from measurements. This result is in agreement with a series of previous work by separate groups.

The critical NO level or OCP in the remote MBL was estimated to be on average between 5 to 9 ppt_v of NO based on the measured parameters. These values are considerably lower than the values suggested by previous studies carried out in a variety of locations. The lower OCP may lead to the conclusion that the ozone production/destruction potential of the remote southern Atlantic Ocean is more responsive to the availability of NO in comparison to other environments.

The comparison between the observed data and EMAC model data demonstrates very good agreement in regard to short lived species such as NO and HO_2. However, a significant difference is seen between the two data sets in regard to O_3 which is a compound with a relatively longer lifetime. This may be a result of transport parameterization within the model and not necessarily due to chemistry. This speculation is based on the fact that as a result of entrainment from the free troposphere into the MBL the concentration of O_3 increases and the concentration of CO decreases simultaneously. In this case the higher O_3 concentrations may be due to entrainment from above, but a look at the CO concentrations contradicts this. The CO concentrations predicted by the model are on average significantly higher, not lower than measured values. This may indicate the need for improvement in regard to transport parameterization within the EMAC model.

It is also worth mentioning that the model runs were carried out with the halogen chemistry turned off. However, this seems to have little impact on the outcome of the data in general, as the model and measured values are in relatively good agreement especially in regard to short lived species. It can be speculated that the discrepancy seen in O_3 data may be a result of missing halogen chemistry. However, this is most probably not the case as the effect of halogen chemistry on O_3 would result in lower O_3 concentrations from the model whereas as in this case the model produces higher O_3 concentrations compared to measurements.

HO_2 concentrations predicted by the model were in very good agreement with measured HO_2 concentrations. However, RO_2 concentrations from the two data sets demonstrated significant differences. This was not an unanticipated result as the PERCA signal was a great deal higher than expected. The EMAC data is in fact in agreement with data derived from steady state box model results, the CO/CH_4 ratio and also results of previous studies. This again may indicate that the additional signal measured by the PERCA instrument is created by an oxidant other than peroxy radicals.

To our knowledge this is the first study in the remote MBL were the PSS of NOx and O_3 has been studied in a region were NOx values are in the order of 5 to 20 ppt_v. Most previous studies of this kind have only looked at PSS down to a NOx mixing ratio of 100 ppt_v, which is already relatively high compared to the pristine conditions measured on this campaign. Therefore, there is need for more measurements to be carried out in order to better understand the unique processes which are unknown but are of significant importance in the remote regions of the globe.

Currently the size of database needed to define non urban NOx is limited. This is because only during recent years have techniques been available with sufficient sensitivity and range detectability to measure NOx in non urban areas (ppt_v range). In order to further investigate and explain this trend, measurements need to be made in conditions where NOx mixing ratios are below 100 ppt_v. Hopefully this study will stimulate further efforts in the field of developing and measuring NOx concentrations in the remote background regions of the world.

One of the future objectives will also be to measure NOx concentrations in the remote MBL using both a BLC-CLD and a LIF instrument for inter-comparison, as was done during a recent campaign, DOMINO 2008, on the Northern Atlantic coast in Spain. Inter-comparison of data from the two different methods showed excellent agreement. However, due to measurements being on land and not in the remote MBL during the recent campaign, observed NOx data was not in the exceptionally low ppt_v range measured during MD 160, therefore a comparison was only feasible for relatively higher NOx concentrations.

Even though the above results provide confidence that the level of understanding of the photochemistry of O_3 in the remote MBL has made advancements to some extent, from a mechanistic aspect, there remains the important question concerning gas phase chemical processes that is namely halogen chemistry as well as physical removal processes and heterogeneous chemical reactions of ozone. Due to the mentioned deficiencies and also due to the absence of comprehensive O_3 precursor databases our assessment of Tropospheric O_3 in terms of photochemical processes and the general O_3 budget is still in need of intensive future investigation.

In conclusion, it can be said that the results of this doctoral thesis contribute to the advancement of our knowledge on O_3 photochemistry in the non-continental southern hemisphere and lead to a better understanding of the $NO\text{-}NO_2\text{-}O_3$ system in remote MBL.

List of tables

List of figures

3.7 Air temperature measured during MD160, unit is in degrees Celsius.

3.8 The Marion Dufresne. Indicated on this plot is the exhaust stack relative to the atmospheric mast and the instrument container. Wind coming from behind the ship towards the atmospheric mast resulted in data contamination (plot adapted from Zorn et al., 2008).

3.9 The wind filter automatically eliminates data when the wind direction was unsuitable that is when the wind came from the back of the ship (between 55° and 275°). The blue box represents the atmospheric mast on top of which the sampling line was placed.

3.10 Wind speed and wind direction data during the MD160 cruise. Data shown here is from March 5th to 20th.

3.11 The affect of wind direction on measurement contamination on March 17th. Mixing ratios of the measured O_3 (red lines), NO (green dots), NOc (blue dots) and the wind speed (pink line) and wind direction (black dots) are plotted.

4.1 Mixing ratios of the measured O_3 (red circles), NO_2 (blue circles), NO (green circles), JNO_2 (yellow circles) and HO_2 (purple circles) in clean background MBL are plotted for the study period on March 13th 2007.

4.2 Calculated back trajectories for March 13th for the period of study. Plots a, b and c correspond to 9:00, 12:00 and 15:00 GMT respectively. The colour bar below each plot is an indication of the pressure level (300 to 1025 hPa).

4.3 Mixing ratios of the measured O_3 (red circles), NO_2 (blue circles), NO (green circles), JNO_2 (yellow circles), HO_2 (purple circles) and ROx (black circles) in clean background MBL are plotted for the study period on March 14th 2007.

4.4 Calculated back trajectories for March 14th for the period of study. Plots a, b and c correspond to 12:00, 15:00 and 18:00 GMT respectively. The colour bar below each plot is an indication of the pressure level (300 to 1025hPa).

4.5 Mixing ratios of the measured O_3 (red circles), NO_2 (blue circles), NO (green circles), JNO_2 (yellow circles), HO_2 (purple circles) and ROx (black circles) in clean background MBL are plotted for the study period on March 15th 2007.

4.6 Calculated back trajectories for March 15th for the period of study. Plots a, b and c correspond to 9:00, 12:00 and 15:00 GMT respectively. The colour bar below each plot is an indication of the pressure level (300 to 1025 hPa).

4.7 Mixing ratios of the measured O_3 (red circles), NO_2 (blue circles), NO (green circles), JNO_2 (yellow circles), HO_2 (purple circles) and ROx (black circles) in clean background MBL are plotted for the study period on March 16th 2007.

4.8 Calculated back trajectories for March 16th for the period of study. Plots a, b and c correspond to 6:00, 9:00 and 12:00 GMT respectively. The colour bar below each plot is an indication of the pressure level (300 to 1025 hPa).

4.9 Mixing ratios of the measured O_3 (red circles), NO_2 (blue circles), NO (green circles), JNO_2 (yellow circles), HO_2 (purple circles) and ROx (black circles) in clean background MBL are plotted for the study period on March 17th 2007.

4.10 Calculated back trajectories for March 17th for the period of study. Plots a, b and c correspond to 6:00, 9:00 and 12:00 GMT respectively. The colour bar below each plot is an indication of the pressure level (300 to 1025 hPa).

4.11 Mixing ratios of the measured O_3 (red circles), NO_2 (blue circles), NO (green circles), JNO_2 (yellow circles) and ROx (black circles) are plotted for the high NOx episode due to the passing of a second on March 15th 2007.

4.12 Mixing ratios of the measured O_3 (red circles), NO_2 (blue circles), NO (green circles), JNO_2 (yellow circles) and HO_2 (purple circles) are plotted for the African continental air masses measured off the coast of Durban on March 19th 2007.

4.13 Calculated back trajectories for March 19th for the period of study. Plots a, b and c correspond to 6:00, 9:00 and 12:00 GMT respectively. The colour bar below each plot is an indication of the pressure level (300 to 1025 hPa).

4.14 Observed NO/NO_2 ratios (solid circles with bars) compared with calculated values derived from equation 4.4 (open purple circles), equation 4.5 (open blue squares) and equation 4.6 (dashed green line) for March 13th, 2007.

4.15 Observed NO/NO_2 ratios (solid red circles with bars) compared with calculated values derived from equation 4.4 (open purple circles), equation 4.5 (open blue squares), equation 4.6 (dashed green line) and equation 4.6' (yellow line) for March 15th, 2007.

4.16 The observed NO/NO_2 ratios (solid red circles) and calculated equation 4.4 (open purple circles) for March 15th 2007 for the high NOx episode resulting from the passing of a second ship.

4.17 The classic Leighton ratio (equation 4.1) for clean background conditions is plotted as a function of NOx mixing ratios. The colour coding corresponds to the JNO_2 intensity. Plots are for March 13th, 14th, 15th and 16th.

4.18 Leighton ratio values for all days are plotted against NOx mixing ratios (logarithmic scale). The colour bar indicates the JNO_2 intensity.

4.19 Leighton ratio plotted as a function of NOx mixing ratios (logarithmic scale) using equation 4.2. The colour bar indicates the JNO_2 intensity.

4.20 Leighton ratio values for all days are plotted against NOx mixing ratios (logarithmic scale) for both the filtered and unfiltered data sets. Green and red circles represent the filtered and unfiltered data respectively. The axis here is limited to Φ=16.

4.21 Leighton ratio values for all days are plotted against NOx mixing ratios (logarithmic scale) for both the filtered and unfiltered data sets. Green and red circles represent the filtered and unfiltered data respectively.

4.22 The observed NO_2 to calculated NO_2 ratio is plotted as a function of NOx mixing ratios for the pristine background air masses of the MD 160 cruise. The colour bar represents the JNO_2 intensity. The error bar on the single point is for an estimate of the uncertainty factor in this study.

4.23 Diurnal profiles of OH, HO_2 and ROx from March 13th to 19th.

4.24 Results from the EMAC model simulations for HO_2 (green circles) and CH_3O_2 (blue squares).

4.25 Day time results from the steady state box model simulations for HO_2 (green circles) and CH_3O_2 (blue squares).

5.1.a Presented are the hourly averages of ROx, HO_2 and O_3 for background daytime period on March 15th. Blue, green and red squares represent O_3, HO_2 and ROx respectively.

5.1.b Presented are the hourly averages of ROx, HO_2 and O_3 for background daytime period on March 16th. Blue, green and red squares represent O_3, HO_2 and ROx respectively.

5.2.a Time series of ten-minute averaged HO_2, ROx and $JO(^1D)$ during background conditions on March 13th. Blue circles represent HO_2 mixing ratios and $JO(^1D)$ is represented as red crosses and line.

5.2.b Time series of ten-minute averaged HO_2, ROx and $JO(^1D)$ during background conditions on March 14th.

5.2.c Time series of ten-minute averaged HO_2, ROx and $JO(^1D)$ during background conditions on March 15th.

5.2.d Time series of ten-minute averaged HO_2, ROx and $JO(^1D)$ during background conditions on March 16th.

5.3 One-minute averages of the calculated $L(O_3)$, $P(O_3)$ and $T(O_3)$ in the clean background air masses on March 13th (ppt_v/hr). The colour bar in the $L(O_3)$ section of the graph represents the $JO(^1D)$ intensity (unit is s^{-1}). The $P(O_3)$ in this plot was calculated using the assumption $[HO_2] = [RO_2]$.

5.4 One-minute averages of the calculated $L(O_3)$, $P(O_3)$ and $T(O_3)$ in the clean background air masses on March 14th (ppt_v/hr). The colour bar in the $L(O_3)$ section of the graph represents the $JO(^1D)$ intensity (unit is s^{-1}). The $P(O_3)$ and $T(O_3)$ values in this plot were calculated using PERCA data.

5.5 Comparison between $P(O_3)$ calculated from the measured data (green diamonds) and the $P(O_3)$ derived from the assumed RO_2 concentrations (red circles), the ratio is represented as black triangles for March 14th.

5.6 One-minute averages of the calculated $L(O_3)$, $P(O_3)$ and $T(O_3)$ in the clean background air masses on March 15th 2007 (ppt_v/hr). The colour bar in the $L(O_3)$ section of the graph represents the $JO(^1D)$ intensity (unit is s^{-1}). The $P(O_3)$ and $T(O_3)$ in this plot were calculated using PERCA data.

5.7 Comparison between $P(O_3)$ calculated from the measured data (green diamonds) and the $P(O_3)$ derived from the theoretical RO_2 (red circles), the ratio is presented as black triangles for March 15th.

5.8 One-minute averages of the calculated $L(O_3)$, $P(O_3)$ and $T(O_3)$ in the clean background air masses on March 16th (ppt_v/hr). The colour bar in the $L(O_3)$ section of the graph represents the $JO(^1D)$ intensity (unit is s^{-1}). The $P(O_3)$ and $T(O_3)$ values in this plot were calculated using PERCA data.

5.9 Comparison between $P(O_3)$ calculated from the measured data (green diamonds) and the $P(O_3)$ derived from the theoretical RO_2 (red circles), the ratio is presented as black triangles for March 16th.

5.10 Time series of daytime average $P(O_3)$. Blue circle and red diamonds represent the values obtained from measured data and the PSS expression respectively. Units are ppt_v/hr.

5.11 Plot of the average daytime mean ozone production values.

5.12 Time series of 1-minute averaged $P(O_3)$. Blue circle and red diamonds represent the values obtained from measured data and the PSS expression respectively. Units are ppt_v/hr.

5.13 Time series of 1-min averaged $NO_{crit.}$ mixing ratios derived from assumed $[RO_2]$ on March 13th. The colour bar indicates the $JO(^1D)$ intensity.

5.14 Time series of 1-min averaged $NO_{crit.}$ mixing ratios on March 14th. Circles and diamonds represent $NO_{crit.}$ derived from assumed $[RO_2]$ and measured PERCA data respectively. The colour bar indicates the $JO(^1D)$ intensity.

5.15 Time series of 1-min averaged $NO_{crit.}$ mixing ratios on March 15th. Circles and diamonds represent $NO_{crit.}$ derived from assumed $[RO_2]$ and measured PERCA data respectively. The colour bar indicates the $JO(^1D)$ intensity.

5.16 Time series of 1-min averaged $NO_{crit.}$ mixing ratios on March 16th. Circles and diamonds represent $NO_{crit.}$ derived from assumed $[RO_2]$ and measured PERCA data respectively. The colour bar indicates the $JO(^1D)$ intensity.

6.1 Time series of observed data versus EMAC data for March 13th.

6.2 Time series of observed data versus EMAC data for March 14th.

6.3 Time series of observed data versus EMAC data for March 15th.

6.4 Time series of observed data versus EMAC data for March 16th.

List of Abbreviations

(aq)	aqueous
avg.	Average
BLC	Blue light converter
CE	Conversion efficiency
CH_3O_2	Methyl peroxy radical
CL	Chemiluminescence
CLD	Chemiluminescence Detector
DL	Detection Limit
DMS	dimethyl sulfide
ECHAM	European Centre Hamburg general circulation model
EMAC	ECHAM/MESSy Atmospheric chemistry model
(g)	gas
GHG	Green house gas
GMT	Greenwich Mean Time
GPT	Gas phase titration
HO_2	Hydroperoxy radical
HONO	Nitrous acid
IPCC	Intergovernmental Panel of Climate Change
JNO_2	Photolysis rate of NO_2
$JO(^1D)$	Photolysis rate $O(^1D)$
(l)	liquid
LED	Light emitting diodes
LIDAR	Laser Detection And Ranging
LIF	Laser induced fluorescence
LOD	Limit of detection
LT	Local Time
MBL	Marine boundary layer
MD	Marion Dufresne
MESSy	Modular Earth Sub-model System
MPI	Max Planck Institute
CH_3O_2	Methyl peroxy radical
NO	Nitrogen Oxide
NO_2	Nitrogen dioxide
NO2*	Excited nitrogen dioxide
NOx	Total sum of active nitrogen oxides ($NO+NO_2$)
OCP	Ozone compensation point
OH	Hydroxyl radical
OOMPH	Organic over Ocean Modifying Particles in both Hemispheres

PAN	Peroxy Acetyl Nitrate
PERCA	Peroxy radical chemical amplifier
Pmol	Pico-mole (10^{-12})
PMT	Photomultiplier tube
ppb_v	parts per billion
ppm_v	parts per million
ppt_v	parts per trillion
PSS	Photostationary State
RO_2	Organic peroxy radical
ROx	Total sum of organic peroxy radicals
SA	Synthetic air
Sccm	Standard cubic centimeters per minute
SLM	Standard liter per minute
STDEV	Standard deviation
TgN yr^{-1}	Tera (10^{12}) grams of Nitrogen per year
UT	Universal Time
UV	Ultra violet
VOCs	Volatile Organic Compounds

Bibliography

Allan, B.J., McFiggans, G., Plane, J.M.C. and Coe, H.: Observations of iodine monoxide in the remote marine boundary layer, Journal of Geophysical Research-Atmospheres, 105, 14363-14369, 2000.

Atkinson, R., Baulch, D.L., Cox, R.A., Crowley, J.N., Hampson, R.F., Hynes, R.G., Jenkin, M.E., Rossi, M.J. and Troe, J.: Evaluated kinetic and photochemical data for atmospheric chemistry: Volume I - gas phase reactions of Ox, HOx, NOx and SOx species, Atmospheric Chemistry and Physics, 4, 1461-1738, 2004.

Atkinson, R., Baulch, D.L., Cox, R.A., Crowley, J.N., Hampson, R.F., Hynes, R.G., Jenkin, M.E., Rossi, M.J. and Troe, J.: Evaluated kinetic and photochemical data for atmospheric chemistry: Volume III - gas phase reactions of inorganic halogens, Atmospheric Chemistry and Physics, 7, 981-1191, 2007.

Bollinger, M.J., Hahn, C.J., Parrish, D.D., Murphy, P.C., Albritton, D.L. and Fehsenfeld, F.C.: NOx measurements in clean continental air and analysis of the contributing meteorology, Journal of Geophysical Research-Atmospheres, 89, 9623-9631, 1984.

Bradshaw, J., Davis, D., Crawford, J., Chen, G., Shetter, R., Muller, M., Gregory, G., Sachse, G., Blake, D., Heikes, B., Singh, H., Mastromarino, J. and Sandholm, S.: Photofragmentation two-photon laser-induced fluorescence detection of NO_2 and NO: Comparison of measurements with model results based on airborne observations during PEM-Tropics A, Geophysical Research Letters, 26, 471-474, 1999.

Calvert, J.G.: Test of theory of ozone generation in Los-Angeles atmosphere, Environmental Science & Technology, 10, 248-256, 1976.

Cantrell, C.A., Shetter, R.E., Calvert, J.G., Eisele, F.L., Williams, E., Baumann, K., Brune, W.H., Stevens, P.S. and Mather, J.H.: Peroxy radicals from photostationary state deviations and steady state calculations during the tropospheric OH photochemistry experiment at Idaho Hill, Colorado, 1993, Journal of Geophysical Research-Atmospheres, 102, 6369-6378, 1997.

Cantrell, C.A., Edwards, G.D., Stephens, S., Mauldin, R.L., Zondlo, M.A., Kosciuch, E., Eisele, F.L., Shetter, R.E., Lefer, B.L., Hall, S., Flocke, F., Weinheimer, A., Fried, A., Apel, E., Kondo, Y., Blake, D.R., Blake, N.J., Simpson, I.J., Bandy, A.R., Thornton, D.C., Heikes, B.G., Singh, H.B., Brune, W.H., Harder, H., Martinez, M., Jacob, D.J., Avery, M.A., Barrick, J.D., Sachse, G.W., Olson, J.R., Crawford, J.H. and Clarke, A.D.: Peroxy radical behavior during the Transport and Chemical Evolution over the Pacific (TRACE-P) campaign as measured aboard the NASA P-3B aircraft, Journal of Geophysical Research-Atmospheres, 108, 21, 2003.

Carpenter, L.J., Monks, P.S., Bandy, B.J., Penkett, S.A., Galbally, I.E. and Meyer, C.P.: A study of peroxy radicals and ozone photochemistry at coastal sites in the northern and southern hemispheres, Journal of Geophysical Research-Atmospheres, 102, 25417-25427, 1997.

Carpenter, L.J., Clemitshaw, K.C., Burgess, R.A., Penkett, S.A., Cape, J.N. and McFadyen, G.C.: Investigation and evaluation of the NOx/O_3 photochemical steady state, Atmospheric Environment, 32, 3353-3365, 1998.

Chameides, W.L. and Walker, J.C.G.: Photochemical Theory of Tropospheric Ozone, Journal of Geophysical Research, 78, 8751-8760, 1973.

Chameides, W.L., Davis, D.D., Bradshaw, J., Sandholm, S., Rodgers, M., Baum, B., Ridley, B., Madronich, S., Carroll, M.A., Gregory, G., Schiff, H.I., Hastie, D.R., Torres, A. and Condon, E.: Observed and model-calculated NO_2/NO ratios in tropospheric air sampled during the Nasa Gte/Cite-2 field-study, Journal of Geophysical Research-Atmospheres, 95, 10235-10247, 1990.

Chatfield, R.B. and Crutzen, P.J.: Are there interactions of Iodine and Sulfur species in marine air photochemistry?, Journal of Geophysical Research-Atmospheres, 95, 22319-22341, 1990.

Clough, P.N. and Thrush, B.A.: Mechanism of chemiluminescent reaction between Nitric Oxide and Ozone, Transactions of the Faraday Society, 63, 915-927, 1967.

Crawford, J.H., Davis, D.D., Chen, G., Bradshaw, J., Sandholm, S., Kondo, Y., Merrill, J., Liu, S., Browell, E., Gregory, G., Anderson, B., Sachse, G., Barrick, J., Blake, D., Talbot, R. and Pueschel, R.: Implications of large scale shifts in tropospheric NOx levels in the remote tropical Pacific, Journal of Geophysical Research-Atmospheres, 102, 28447-28468, 1997.

Crutzen, P.J.: Discussion of chemistry of some minor constituents in stratosphere and troposphere, Pure and Applied Geophysics, 106, 1385-1399, 1973.

Crutzen, P.J.: Photochemical reactions initiated by and influencing Ozone in unpolluted tropospheric air, Tellus, 26, 47-57, 1974.

Crutzen, P.J.: The role of NO and NO_2 in the chemistry of the troposphere and stratosphere, Annual Review of Earth and Planetary Sciences, Vol. 7, 443-472 1979.

Crutzen, P.J.: Tropospheric Ozone: an Overview, NATO ASI Series, Series C Mathematical and Physical Sciences, D. Reidel Publishing Company, 3-32, 1988.

Danielsen, E.F.: Stratospheric-tropospheric exchange based on radioactivity Ozone and potential vorticity, Journal of the Atmospheric Sciences, 25, 502-518, 1968.

Danielsen, E.F. and Mohnen, V.A.: Project dustorm report - Ozone transport, insitu measurements, and meteorological analyses of tropopause folding, Journal of Geophysical Research-Oceans and Atmospheres, 82, 5867-5877, 1977.

Davis, D.D., Crawford, J., Chen, G., Chameides, W., Liu, S., Bradshaw, J., Sandholm, S., Sachse, G., Gregory, G., Anderson, B., Barrick, J., Bachmeier, A., Collins, J., Browell, E., Blake, D., Rowland, S., Kondo, Y., Singh, H., Talbot, R., Heikes, B., Merrill, J., Rodriguez, J. and Newell, R.E.: Assessment of ozone photochemistry in the western North Pacific as inferred from PEM-West A observations during the fall 1991, Journal of Geophysical Research-Atmospheres, 101, 2111-2134, 1996.

Del Negro, L.A., Fahey, D.W., Gao, R.S., Donnelly, S.G., Keim, E.R., Neuman, J.A., Cohen, R.C., Perkins, K.K., Koch, L.C., Salawitch, R.J., Lloyd, S.A., Proffitt, M.H., Margitan, J.J., Stimpfle, R.M., Bonne, G.P., Voss, P.B., Wennberg, P.O., McElroy, C.T., Swartz, W.H., Kusterer, T.L., Anderson, D.E., Lait, L.R. and Bui, T.P.: Comparison of modeled and observed values of NO_2 and JNO_2 during the Photochemistry of Ozone Loss in the Arctic Region in Summer (POLARIS) mission, Journal of Geophysical Research-Atmospheres, 104, 26687-26703, 1999.

Demerjian, K.L., Kerr, J.A. and Calvert, J.G.: The Mechanism of Photochemical Smog Formation, Pitts, James N. Jr. and Robert L. Metcalf, 1-262, 1974.

DeMore, W.B., Howard, C.J., Golden, D.M., Kolb, C.E., Hampson, R.F. and Molina, M.J.: Chemical kinetics and photochemical data for use in stratospheric modeling, JPL Publication, NASA Jet Propulsion Laboratory, 97-4, 1997.

Dickerson, R.R., Rhoads, K.P., Carsey, T.P., Oltmans, S.J., Burrows, J.P. and Crutzen, P.J.: Ozone in the remote marine boundary layer: A possible role for halogens, Journal of Geophysical Research-Atmospheres, 104, 21385-21395, 1999.

Duce, R.A., Winchest.Jw and Vannahl, T.W.: Iodine Bromine and Chlorine in Hawaiian marine atmosphere, Journal of Geophysical Research, 70, 1775-&, 1965.

Fabian, P.: Comments on 'Photochemical theory of tropospheric Ozone' by W. Chameides and J.C.G. Walker Journal of Geophysical Research, 79, 4124-4125, 1974.

Fabian, P. and Pruchniewicz, P.G.: Meridional Distribution of Ozone in Troposphere and Its Seasonal-Variations, Journal of Geophysical Research-Oceans and Atmospheres, 82, 2063-2073, 1977.

Fehsenfeld, F.C., Drummond, J.W., Roychowdhury, U.K., Galvin, P.J., Williams, E.J., Buhr, M.P., Parrish, D.D., Hubler, G., Langford, A.O., Calvert, J.G., Ridley, B.A., Grahek, F., Heikes, B.G., Kok, G.L., Shetter, J.D., Walega, J.G., Elsworth, C.M., Norton, R.B., Fahey, D.W., Murphy, P.C., Hovermale, C., Mohnen, V.A., Demerjian, K.L., Mackay, G.I. and Schiff, H.I.: Intercomparison of NO_2 measurement techniques, Journal of Geophysical Research-Atmospheres, 95, 3579-3597, 1990.

Fickert, S., Adams, J.W. and Crowley, J.N.: Activation of Br_2 and BrCl via uptake of HOBr onto aqueous salt solutions, Journal of Geophysical Research-Atmospheres, 104, 23719-23727, 1999.

Finalyson-Pitts, B.J. and Pitts, J.N.: Chemistry of the upper and lower atmosphere: Theory, experiments, and applications, Academic Press, San Diego, 1999.

Fischer, H., Kormann, R., Klupfel, T., Gurk, C., Konigstedt, R.K., Parchatka, U., Muhle, J., Rhee, T.S., Brenninkmeijer, C.A.M., Bonasoni, P. and Stohl, A.: Ozone production and trace gas correlations during the June 2000 MINATROC intensive measurement campaign at Mt. Cimone, Atmospheric Chemistry and Physics, 3, 725-738, 2003.

Fishman, J., Solomon, S. and Crutzen, P.J.: Observational and theoretical evidence in support of a significant insitu photochemical source of tropospheric Ozone, Tellus, 31, 432-446, 1979.

Fontijn, A., Sabadell, A.J. and Ronco, R.J.: Homogeneous chemiluminescent measurement of Nitric Oxide with Ozone: Implications for continuous selective monitoring of gaseous air pollutants, Analytical Chemistry, 42, 575-&, 1970.

Friess, U., Hollwedel, J., Konig-Langlo, G., Wagner, T. and Platt, U.: Dynamics and chemistry of tropospheric bromine explosion events in the Antarctic coastal region, Journal of Geophysical Research-Atmospheres, 109, 15, 2004.

Galbally, I.E., Bentley, S.T. and Meyer, C.P.: Mid-latitude marine boundary-layer ozone destruction at visible sunrise observed at Cape Grim, Tasmania, 41 degrees South, Geophysical Research Letters, 27, 3841-3844, 2000.

Gao, R.S., Keim, E.R., Woodbridge, E.L., Ciciora, S.J., Proffitt, M.H., Thompson, T.L., McLaughlin, R.J. and Fahey, D.W.: New photolysis system for NO_2 measurements in the lower Stratosphere, Journal of Geophysical Research-Atmospheres, 99, 20673-20681, 1994.

Grannas, A.M., Jones, A.E., Dibb, J., Ammann, M., Anastasio, C., Beine, H.J., Bergin, M., Bottenheim, J., Boxe, C.S., Carver, G., Chen, G., Crawford, J.H., Domine, F., Frey, M.M., Guzman, M.I., Heard, D.E., Helmig, D., Hoffmann, M.R., Honrath, R.E., Huey, L.G., Hutterli, M., Jacobi, H.W., Klan, P., Lefer, B., McConnell, J., Plane, J., Sander, R., Savarino, J., Shepson, P.B., Simpson, W.R., Sodeau, J.R., von Glasow, R., Weller, R., Wolff, E.W. and Zhu, T.: An overview of snow photochemistry: evidence, mechanisms and impacts, Atmospheric Chemistry and Physics, 7, 4329-4373, 2007.

Gros, V., Poisson, N., Martin, D., Kanakidou, M. and Bonsang, B.: Observations and modeling of the seasonal variation of surface ozone at Amsterdam Island: 1994-1996, Journal of Geophysical Research-Atmospheres, 103, 28103-28109, 1998.

Haagensmit, A.J.: Chemistry and physiology of Los-Angeles smog, Industrial and Engineering Chemistry, 44, 1342-1346, 1952.

Haagensmit, A.J. and Fox, M.M.: Ozone formation in photochemical oxidation of organic substances, Industrial and Engineering Chemistry, 48, 1484-1487, 1956.

Hauglustaine, D.A., Madronich, S., Ridley, B.A., Walega, J.G., Cantrell, C.A., Shetter, R.E. and Hubler, G.: Observed and model-calculated photostationary state at Mauna Loa observatory during MLOPEX 2, Journal of Geophysical Research-Atmospheres, 101, 14681-14696, 1996.

Hauglustaine, D.A., Madronich, S., Ridley, B.A., Flocke, S.J., Cantrell, C.A., Eisele, F.L., Shetter, R.E., Tanner, D.J., Ginoux, P. and Atlas, E.L.: Photochemistry and budget of ozone during the Mauna Loa Observatory Photochemistry Experiment (MLOPEX 2), Journal of Geophysical Research-Atmospheres, 104, 30275-30307, 1999.

Hegglin, M.I.: Airborne NOy-, NO- and O_3- measurements during SPURT: Implications for atmospheric transport, PhD thesis, ETH Zurich, Switzerland, 2004.

Hönninger, G.: Halogen Oxide Studies in the Boundary Layer by Multi Axis Differential Optical Absorption Spectroscopy and Active Longpath-DOAS, PhD Thesis, University Heidelberg, Heidelberg, Germany, 2002.

Huebert, B.J. and Lazrus, A.L.: Global tropospheric measurements of Nitric-Acid vapor and particulate Nitrate, Geophysical Research Letters, 5, 577-580, 1978.

IPCC: Climate Change 2007: The physical science basis. Contribution of working group I to the fourth assessment report of the Intergovernmental Panel on climate Change, Baede, A. P. M., Cambridge University Press, 2007.

Janach, W.E.: Surface Ozone - trend details, Seasonal-variations, and interpretation, Journal of Geophysical Research-Atmospheres, 94, 18289-18295, 1989.

Joeckel, P., Tost, H., Pozzer, A., Bruehl, C., Buchholz, J., Ganzeveld, L., Hoor, P., Kerkweg, A., Lawrence, M., Sander, R., Steil, B., Stiller, G., Tanarhte, M., Taraborrelli, D., van Aardenne, J. and Lelieveld, J.: The atmospheric chemistry general circulation model ECHAM5/MESSy1, Atmospheric Chemistry and Physics, 6, 5067-5104, 2006.

Junkermann, W., Platt, U. and Volzthomas, A.: A photoelectric detector for the measurement of photolysis frequencies of Ozone and other atmospheric molecules, Journal of Atmospheric Chemistry, 8, 203-227, 1989.

Kanaya, Y., Yokouchi, Y., Matsumoto, J., Nakamura, K., Kato, S. , Tanimoto, H. , Furutani, H. , Toyota K., and Akimoto H.: Implications of iodine chemistry for daytime HO_2 levels at Rishiri Island, Geophysical Research Letters 29, 2002.

Keene, W.C., Pszenny, A.A.P., Maben, J.R. and Sander, R.: Variation of marine aerosol acidity with particle size, Geophysical Research Letters, 29, 5-1-5-5-4, 2002.

Kondo, Y., Ziereis, H., Koike, M., Kawakami, S., Gregory, G.L., Sachse, G.W., Singh, H.B., Davis, D.D. and Merrill, J.T.: Reactive nitrogen over the Pacific Ocean during PEM-West A, Journal of Geophysical Research-Atmospheres, 101, 1809-1828, 1996.

Leighton, P.A.: Photochemistry of air pollution, Physical Chemistry, 9, 300, 1961.

Lelieveld, J. and Dentener, F.J.: What controls tropospheric ozone?, Journal of Geophysical Research-Atmospheres, 105, 3531-3551, 2000.

Lelieveld, J., van Aardenne, J., Fischer, H., de Reus, M., Williams, J. and Winkler, P.: Increasing ozone over the Atlantic Ocean, Science, 304, 1483-1487, 2004.

Leser, H., Honninger, G. and Platt, U.: MAX-DOAS measurements of BrO and NO_2 in the marine boundary layer, Geophysical Research Letters, 30, 4, 2003.

Liu, S.C., Kley, D., McFarland, M., Mahlman, J.D. and Levy, H.: On the origin of tropospheric Ozone, Journal of Geophysical Research-Oceans and Atmospheres, 85, 7546-7552, 1980.

Liu, S.C., McFarland, M., Kley, D., Zafiriou, O. and Huebert, B.: Tropospheric NOx and O_3 budgets in the equatorial pacific, Journal of Geophysical Research-Oceans and Atmospheres, 88, 1360-1368, 1983.

Liu, S.C., Trainer, M., Fehsenfeld, F.C., Parrish, D.D., Williams, E.J., Fahey, D.W., Hubler, G. and Murphy, P.C.: Ozone production in the rural troposphere and the implications for regional and global Ozone distributions, Journal of Geophysical Research-Atmospheres, 92, 4191-4207, 1987.

Ljungstrom, E. and Hallquist, M.: Nitrate radical formation rates in Scandinavia, Atmospheric Environment, 30, 2925-2932, 1996.

Logan, J.A.: Tropospheric chemistry a global perspective, Abstracts of Papers American Chemical Society, 86, 7210-7254, 1981.

Logan, J.A.: Tropospheric Ozone - seasonal behavior, trends, and anthropogenic influence, Journal of Geophysical Research-Atmospheres, 90, 10463-10482, 1985.

Mannschreck, K., Gilge, S., Plass-Duelmer, C., Fricke, W. and Berresheim, H.: Assessment of the applicability of NO-NO_2-O_3 photostationary state to long-term measurements at the Hohenpeissenberg GAW Station, Germany, Atmospheric Chemistry and Physics, 4, 1265-1277, 2004.

Martinez, M., Harder, H., Kubistin, D., Rudolf, M., Bozem, H., Eerdekens, G., Fischer, H., Gurk, C., Kluepfel, T., Koenigstedt, R., Parchatka, U., Schiller, C.L., Stickler, A., Williams, J. and Lelieveld, J.: Hydroxyl radicals in the tropical troposphere over the Suriname rainforest: airborne measurements, Atmospheric Chemistry and Physics Discussion, 8, 15491-15536, 2008.

Matsumoto, J., Kosugi, N., Nishiyama, A., Isozaki, R., Sadanaga, Y., Kato, S., Bandow, H. and Kajii, Y.: Examination on photostationary state of NOx in the urban atmosphere in Japan, Atmospheric Environment, 40, 3230-3239, 2006.

McFarland, M., Kley, D., Drummond, J.W., Schmeltekopf, A.L. and Winkler, R.H.: Nitric-Oxide measurements in the equatorial Pacific region, Geophysical Research Letters, 6, 605-608, 1979.

Mihelcic, D., Holland, F., Hofzumahaus, A., Hoppe, L., Konrad, S., Musgen, P., Patz, H.W., Schafer, H.J., Schmitz, T., Volz-Thomas, A., Bachmann, K., Schlomski, S., Platt, U., Geyer, A., Alicke, B. and Moortgat, G.K.: Peroxy radicals during BERLIOZ at Pabstthum: Measurements, radical budgets and ozone production, Journal of Geophysical Research-Atmospheres, 108, 17, 2003.

Monks, P., Carpenter, L.J., Penkett, S.A., Ayers, G.P., Gillett, R.W., Galbally, I.E. and Meyer, C.P.: Fundamental ozone photochemistry in the remote marine boundary layer: the soapex experiment, measurement and theory

Atmospheric Environment, 32, 3647-3664, 1998.

Parker, A.E., Monks, P.S., Wyche, K.P., Balzani-Loov, J.M., Staehelin, J., Reimann, S., Legreid, G., Vollmer, M.K. and Steinbacher, M.: Peroxy radicals in the summer free troposphere: seasonality and potential for heterogeneous loss, Atmospheric Chemistry and Physics, 9, 1989-2006, 2009.

Parrish, D.D., Trainer, M., Williams, E.J., Fahey, D.W., Hubler, G., Eubank, C.S., Liu, S.C., Murphy, P.C., Albritton, D.L. and Fehsenfeld, F.C.: Measurements of the NOx-O_3 Photostationary State at Niwot Ridge, Colorado, Journal of Geophysical Research-Atmospheres, 91, 5361-5370, 1986.

Penkett, S.A., Monks, P.S., Carpenter, L.J., Clemitshaw, K.C., Ayers, G.P., Gillett, R.W., Galbally, I.E. and Meyer, C.P.: Relationships between ozone photolysis rates and peroxy radical concentrations in clean marine air over the Southern Ocean, Journal of Geophysical Research-Atmospheres, 102, 12805-12817, 1997.

Perner, D., Arnold, T., Crowley, J., Klupfel, T., Martinez, M. and Seuwen, R.: The measurement of active chlorine in the atmosphere by chemical amplification, XXIII

General Assembly of the European-Geophysical-Society, Kluwer Academic Publishing 9-20, 1998.

Platt, U., Perner, D. and Patz, H.W.: Simultaneous Measurement of Atmospheric CH_2O, O_3, and NO_2 by Differential Optical-Absorption, Journal of Geophysical Research-Oceans and Atmospheres, 84, 6329-6335, 1979.

Read, K.A., Mahajan, A.S., Carpenter, L.J., Evans, M.J., Faria, B.V.E., Heard, D.E., Hopkins, J.R., Lee, J.D., Moller, S.J., Lewis, A.C., Mendes, L., McQuaid, J.B., Oetjen, H., Saiz-Lopez, A., Pilling, M.J. and Plane, J.M.C.: Extensive halogen-mediated ozone destruction over the tropical Atlantic Ocean, Nature, 453, 1232-1235, 2008.

Richter, A.: Nitrogen oxides in the troposphere - What have we learned from satellite measurements?, European Physical J. Conferences, 1, 149-156, 2009.

Ridley, B.A. and Howlett, L.C.: Instrument for Nitric-Oxide measurements in stratosphere, Review of Scientific Instruments, 45, 742-746, 1974.

Ridley, B.A., Madronich, S., Chatfield, R.B., Walega, J.G., Shetter, R.E., Carroll, M.A. and Montzka, D.D.: Measurements and model simulations of the photostationary state during the Mauna-Loa-Observatory photochemistry experiment - Implications for radical concentrations and Ozone production and loss rates, Journal of Geophysical Research-Atmospheres, 97, 10375-10388, 1992.

Roeckner, E., Brokopf, R., Esch, M., Giorgetta, M., Hagemann, S., Kornblueh, L., Manzini, E., Schlese, U. and Schulzweida, U.: Sensitivity of simulated climate to horizontal and vertical resolution in the ECHAM5 atmosphere model, Journal of Climate, 19, 3771-3791, 2006.

Ryerson, T.B., Williams, E.J. and Fehsenfeld, F.C.: An efficient photolysis system for fast-response NO_2 measurements, Journal of Geophysical Research-Atmospheres, 105, 26447-26461, 2000.

Saiz-Lopez, A., Plane, J.M.C. and Shillito, J.A.: Bromine oxide in the mid-latitude marine boundary layer, Geophysical Research Letters, 31, 4, 2004.

Saiz-Lopez, A., Shillito, J.A., Coe, H. and Plane, J.M.C.: Measurements and modelling of I_2, IO, OIO, BrO and NO_3 in the mid-latitude marine boundary layer, Atmospheric Chemistry and Physics, 6, 1513-1528, 2006.

Salisbury, G., Monks, P.S., Bauguitte, S., Bandy, B.J. and Penkett, S.A.: A seasonal comparison of the ozone photochemistry in clean and polluted air masses at Mace Head, Ireland, Journal of Atmospheric Chemistry, 41, 163-187, 2002.

Sander, R. and Crutzen, P.J.: Model study indicating halogen activation and ozone destruction in polluted air masses transported to the sea, Journal of Geophysical Research-Atmospheres, 101, 9121-9138, 1996.

Sander, S.P., Golden, D.M., Kurylo, M.J., Moortgat, G.K., Wine, P.H., Ravishankara, A.R., Kolb, C.E., Molina, M.J., Finlayson-Pitts, B.J., Huie, R.E. and Orkin, V.L.: Chemical Kinetics and photochemical data for use in stratospheric modeling - evaluation number 15, Jet Propulsion Laboratory, California Institute of Technology, California, 2006

Schurath, U., Lippmann, H.H. and Jesser, B.: Temperature dependence of the chemiluminescent reaction ($NO+O_3 \rightarrow NO_2+O_3$) and quenching of the excited product, Berichte Der Bunsen-Gesellschaft-Physical Chemistry Chemical Physics, 85, 807-813, 1981.

Seinfeld, J.H. and Pandis, S.N.: Atmospheric Chemistry and Physics: from air pollution to climate change, 2006.

Singh, H.B., Ludwig, F.L. and Johnson, W.B.: Tropospheric Ozone - Concentrations and Variabilities in Clean Remote Atmospheres, Atmospheric Environment, 12, 2185-2196, 1978.

Stickler, A., Fischer, H., Bozem, H., Gurk, C., Schiller, C., Martinez-Harder, M., Kubistin, D., Harder, H., Williams, J., Eerdekens, G., Yassaa, N., Ganzeveld, L., Sander, R. and Lelieveld, J.: Chemistry, transport and dry deposition of trace gases in the boundary layer over the tropical Atlantic Ocean and the Guyanas during the GABRIEL field campaign, Atmospheric Chemistry and Physics, 7, 3933-3956, 2007.

Stutz, J., Ackermann, R., Fast, J.D. and Barrie, L.: Atmospheric reactive chlorine and bromine at the Great Salt Lake, Utah, Geophysical Research Letters, 29, 18-1-18-18-4, 2002.

Thompson, A.M.: The oxidizing capacity of the earths atmosphere - Probable past and future changes, Science, 256, 1157-1165, 1992.

Thornton, J.A., Wooldridge, P.J., Cohen, R.C., Martinez, M., Harder, H., Brune, W.H., Williams, E.J., Roberts, J.M., Fehsenfeld, F.C., Hall, S.R., Shetter, R.E., Wert, B.P. and Fried, A.: Ozone production rates as a function of NOx abundances and HOx production rates in the Nashville urban plume, Journal of Geophysical Research, 107, 2002.

Tiao, G.C., Reinsel, G.C., Pedrick, J.H., Allenby, G.M., Mateer, C.L., Miller, A.J. and Deluisi, J.J.: A statistical trend analysis of Ozonesonde data, Journal of Geophysical Research-Atmospheres, 91, 3121-3136, 1986.

Vogt, R., Crutzen, P.J. and Sander, R.: A mechanism for halogen release from sea-salt aerosol in the remote marine boundary layer, Nature, 383, 327-330, 1996.

Volz-Thomas, A., Lerner, A., Patz, H.W., Schultz, M., McKenna, D.S., Schmitt, R., Madronich, S. and Roth, E.P.: Airborne measurements of the photolysis frequency of NO_2, Journal of Geophysical Research-Atmospheres, 101, 18613-18627, 1996.

Volz-Thomas, A., Patz, H.W., Houben, N., Konrad, S., Mihelcic, D., Klupfel, T. and Perner, D.: Inorganic trace gases and peroxy radicals during BERLIOZ at Pabstthum: An investigation of the photostationary state of NOx and O_3, Journal of Geophysical Research-Atmospheres, 108, 2003.

Volz, A. and Drummond, J.W.: Measurements of Nitrogen-Oxides at ppt Levels by Chemiluminescence with O_3, Fresenius Zeitschrift Fur Analytische Chemie, 317, 355-358, 1984.

von Glasow, R., Sander, R., Bott, A. and Crutzen, P.J.: Modeling halogen chemistry in the marine boundary layer - 2. Interactions with sulfur and the cloud-covered MBL, Journal of Geophysical Research-Atmospheres, 107, 13, 2002.

von Glasow, R., von Kuhlmann, R., Lawrence, M.G., Platt, U. and Crutzen, P.J.: Impact of reactive bromine chemistry in the troposphere, Atmospheric Chemistry and Physics, 4, 2481-2497, 2004.

von Glasow, R. and Crutzen, P.J.: Tropospheric Halogen chemistry, Treatise on Geochemistry, 4.02, 1-67, 2007.

von Glasow, R.: Atmospheric chemistry - Sun, sea and ozone destruction, Nature, 453, 1195-1196, 2008.

Wagner, T., Leue, C., Wenig, M., Pfeilsticker, K. and Platt, U.: Spatial and temporal distribution of enhanced boundary layer BrO concentrations measured by the GOME instrument aboard ERS-2, Journal of Geophysical Research-Atmospheres, 106, 24225-24235, 2001.

Wang, Y.H. and Jacob, D.J.: Anthropogenic forcing on tropospheric ozone and OH since preindustrial times, Journal of Geophysical Research-Atmospheres, 103, 31123-31135, 1998.

Wendel, G.J., Stedman, D.H., Cantrell, C.A. and Damrauer, L.: Luminol-Based Nitrogen-Dioxide Detector, Analytical Chemistry, 55, 937-940, 1983.

Wernli, H. and Davies, H.C.: A Lagrangian-based analysis of extratropical cyclones. I: The method and some applications, Quarterly Journal of the Royal Meteorological Society, 123, 467-489, 1997.

WHO: Aspect of Air pollution with particulate matter, Ozone and Nitrogen Dioxide, World Health Organization, Bonn, 2003.

Yang, J., Honrath, R.E., Peterson, M.C., Parrish, D.D. and Warshawsky, M.: Photostationary state deviation-estimated peroxy radicals and their implications for HOx and ozone photochemistry at a remote northern Atlantic coastal site, Journal of Geophysical Research-Atmospheres, 109, 16, 2004.

Yang, X., Cox, R.A., Warwick, N.J., Pyle, J.A., Carver, G.D., O'Connor, F.M. and Savage, N.H.: Tropospheric bromine chemistry and its impacts on ozone: A model study, Journal of Geophysical Research-Atmospheres, 110, 18, 2005.

Zoellner, M.: Untersuchungen zur troposphärischen Photochemie am GAW-Observatorium Izana, PhD thesis, Fachbereich Chemie, Pharmazie und Geowissenschaften, Johannes Gutenberg-Universität in Mainz, 2008.

Zorn, S.R., Drewnick, F., Schott, M., Hoffmann, T. and Borrmann, S.: Characterization of the South Atlantic marine boundary layer aerosol using an aerodyne aerosol mass spectrometer, Atmospheric Chemistry and Physics, 8, 4711-4728, 2008.